UNIVERSIDADE DE SÃO PAULO
ESCOLA DE ENGENHARIA DE SÃO CARLOS

Vitor Akihiro Hisano Higuti

2D LiDAR-based Perception for Under Canopy Autonomous Scouting of Small Ground Robots within Narrow Lanes of Agricultural Fields

São Carlos

2021

Vitor Akihiro Hisano Higuti

2D LiDAR-based Perception for Under Canopy Autonomous Scouting of Small Ground Robots within Narrow Lanes of Agricultural Fields

Thesis presented to São Carlos School of Engineering, University of São Paulo, as part of the requirements for the degree of Doctor of Science - Post-graduate Program in Mechanical Engineering.

Concentration area: Machine and System Dynamics

Supervisor: Assoc. Prof. Marcelo Becker
Co-supervisor: Prof. Dr. Rafael Vidal Aroca

CORRECTED VERSION
ORIGINAL VERSION AVAILABLE ON MECHANICAL ENGINEERING DEPARTMENT AT EESC-USP

São Carlos
2021

Ficha catalográfica elaborada pela Biblioteca Prof. Dr. Sérgio Rodrigues Fontes da EESC/USP com os dados inseridos pelo(a) autor(a).

Higuti, Vitor Akihiro Hisano
H6342 2D LiDAR-based Perception for Under Canopy Autonomous Scouting of Small Ground Robot within Narrow Lanes of Agricultural Fields / Vitor Akihiro Hisano Higuti; orientador Marcelo Becker; coorientador Rafael Aroca. São Carlos, 2021.

Tese (Doutorado) - Programa de Pós-Graduação em Engenharia Mecânica e Área de Concentração em Dinâmica e Mecatrônica -- Escola de Engenharia de São Carlos da Universidade de São Paulo, 2021.

1. Mobile Robotics. 2. Agricultural Robots. 3. Perception. 4. LiDAR. I. Título.

Eduardo Graziosi Silva - CRB - 8/8907

FOLHA DE JULGAMENTO

Candidato: Engenheiro **VITOR AKIHIRO HISANO HIGUTI.**

Título da tese: "Percepção baseada em LiDAR 2D para movimentação autônoma embaixo da folhagem de pequenos robôs terrestres em faixas estreitas de plantações agrícolas".

Data da defesa: 29/03/2021.

Comissão Julgadora	**Resultado**
Prof. Associado **Marcelo Becker (Orientador)** (Escola de Engenharia de São Carlos – EESC/USP)	***APROVADO***
Prof. Associado **Daniel Varela Magalhães** (Escola de Engenharia de São Carlos – EESC/USP)	***APROVADO***
Prof. Dr. **Girish Chowdhary** (Universidade de Illinois - Urbana-Champaign/UIUC)	***APROVADO***
Prof. Associado **José Paulo Molin** (Escola Superior de Agricultura Luiz de Queiroz - ESALQ/USP)	***APROVADO***
Prof. Dr. **Paulo Lilles Jorge Drews Junior** (Universidade Federal do Rio Grande/FURG)	***APROVADO***

Coordenador do Programa de Pós-Graduação em Engenharia Mecânica:
Prof. Associado **Carlos de Marqui Junior**
Presidente da Comissão de Pós-Graduação:
Prof. Titular **Murilo Araujo Romero**

This work is dedicated to God, my mother Marina, my father Alberto, my sister Ayumi and my brother Yoshiriki. They provided me unconditional love and support in times of joy and darkness.

ACKNOWLEDGEMENTS

This work became possible due to precious contributions and support of many institutions and people.

First and foremost, I express my deepest gratitude towards my advisor, Prof. Marcelo Becker. His devotion to make the world a better place with exciting and ambitious projects motivates us all in the laboratory. His trust allowed me to move forward without fear because I could also count with his support and guidance, shown on many project changes, paper revisions and disheartening field experiments.

I would like to thank São Paulo Research Foundation (FAPESP) for providing financial resources to conduct the research through grants 2018/10894-2, 2017/00033-7, 2016/09970-0 and 2013/07276-1, and National Council for Scientific and Technological Development (CNPq) under grant 131474/2016-2.

I would like to thank the School of Engineering of São Carlos at University of São Paulo (EESC-USP) for providing the infrastructure to develop the work on both research and technical levels. In particular, I am grateful for the invaluable advices and technical support from LabRom, LabDin, Lamafe and LIEPO-CEPOF, whose members provided the means to take projects out of paper.

I would like to thank the fruitful joint research with University of Illinois at Urbana-Champaign since 2017. Special thanks to DASLab and EarthSense for conducting extensive field experiments and providing access to their databases, video footage and TerraSentia robots. I also want to thank their partners Jacob Washburn, Plant Genetics Researcher at University of Missouri, and Joseph Gage, NSF Postdoctoral Fellow at Buckler and Gore Labs, Cornell University. Other institutions and grants involved are USDA-ARS, Cornell University Startup Funds, and Advanced Research Projects Agency-Energy (ARPA-E), U.S. Department of Energy Award Number DE-AR0000598.

I would like to thank the fruitful joint research with Embrapa Instrumentation which led to the development and construction of the robotic platforms Mirã and Mirã II to demonstrate innovation in soil analysis. In particular, I would like to thank Debora Marcondes Bastos Pereira, current Deputy Head of Transfer Technology, for the trust since undergraduate time.

I would like to thank Prof. Girish Chowdhary and Chinmay Soman for the welcoming time while in Urbana-Champaign, for the trust and for the on-going joint research that took my initial research to a much higher level. Their inputs have not been limited to experience sharing and guidance, but also translated into two TerraSentia robots donated to our laboratory from EarthSense.

I would like to thank my co-advisor, Prof Rafael Aroca. His passion with robotics and his willingness to get hands-on inspired me to take projects out of paper and see them on real life.

I would like to thank José Rizardi for the priceless inputs on the design and for the manufacture of hElvis and Mirã II.

I would like to thank Ladislau Marcelino Rabello, Pedro Fernandes Bonfim and René de Oste for all logistics to enable field experiments in São Carlos and for making those field trips more enjoyable.

I would like to thank Nolan Repogle and Sri Theja Vuppala for their invaluable work to keep TerraSentia robots operational and handling the logistics for field experiments in Urbana-Champaign.

I am deeply thankful for having Andres Baquero and Mateus Valverde not only as work colleagues for years, but also for their friendship. Through all the work we have conducted so far, we shared many joys and sadness, but with certainty of a brighter future.

I would like to thank Amy Tanaami, Raphael Marcari, Henrique Toledo, Marco Arruda, Leonardo Bonacini, Ingrid Argote, Byron Portilla, Alexandre Padilla and Renan Moreira from whom I got precious advice on research and pleasant company on tough times. I extend my gratitude towards all my friends and acquaintances who made this journey enjoyable.

Finally, I am immensely pleased to have met and became friends with Myrella Vieira, a joyful and shiny person that not only supported and advised me on this work's tough times but also brought inestimable reflections about life.

ABSTRACT

HIGUTI, V. A. H. **2D LiDAR-based Perception for Under Canopy Autonomous Scouting of Small Ground Robots within Narrow Lanes of Agricultural Fields**. 2021. 118p. Ph.D. Thesis - Escola de Engenharia de São Carlos, Universidade de São Paulo, São Carlos, 2021.

Lightweight ground robots have been increasingly showing their potential to tackle agricultural tasks that require time-consuming human labor thus limited in detail or area coverage. A task that benefits several modern agricultural practices is scouting (*walking though the field*). However, a reliable autonomous navigation is still a challenge. A robot needs to deal with the agricultural field dynamism and unpredictable obstacles, e.g. humans and machines. In particular, corn and sorghum present an additional issue due to the standard way of cultivation: Narrow sub-meter lanes that become even less visible on later stages due to dense coverage and spreading of leaves. This condition heavily influences the sensors by provoking frequent occlusions, misreadings and other situations out of their working range. In such context, three questions arise: 1) *Can the unexplored potential of Light Detection and Ranging (LiDAR) sensor suffice to interpret a narrow lane crop environment without artificial landmarks?* 2) *Does the search of a best line representation for crop rows really represent the problem?* 3) *How can lateral distance estimation be improved through sensor fusion?* To answer these three questions, ***Perception LiDAR*** (***PL***) has been developed to estimate lateral distance to crop rows using a 2D LiDAR as the core sensor. An Extended Kalman Filter enables the use of embedded odometry and inertial measurements. Manual ground truth has shown that the task of finding best line representation from LiDAR data is challenging, and it could have as low as 54% of line estimates within 0.05 m error. Nonetheless, the proposed method has enabled 72 km of autonomous operation of multiple robots. Due to unreliable RTK-GNSS signal under canopy, ***PL*** outputs significantly outperform the GNSS-based positioning, which may not even be in the current lane. The extensive field testing happened in multiple corn and sorghum fields between 2017 and 2020. For continuous lane, i.e. at least one of the side rows exists, the success rate to finish the desired segment of autonomous navigation is 89.76%. The higher performance for LiDAR input with significant less presence of objects other than stalks, and also the failure concentration on sensor occlusion and gaps, both situations with low to none visible rows, strongly indicates that the problem is not best line fitting, but rather a classification one where the end goal is to find stalks. In summary, although ***PL*** does not provide a fully intervention-free for within crop rows navigation, its current capabilities relieve operators from the tedious task of manually driving the robot the whole time and pave the way towards a fully autonomous agricultural robot.

Keywords: Mobile Robotics. Agricultural Robots. Perception. LiDAR.

RESUMO

HIGUTI, V. A. H. **Percepção baseada em LiDAR 2D para movimentação autônoma embaixo da folhagem de pequenos robôs terrestres em faixas estreitas de plantações agrícolas**. 2021. 118p. Tese (Doutorado) - Escola de Engenharia de São Carlos, Universidade de São Paulo, São Carlos, 2021.

Robôs terrestres leves têm mostrado crescente potencial em tarefas agrícolas que requerem moroso trabalho humano, portanto, limitadas em detalhes ou abrangência de área. Uma atividade que beneficia várias práticas agrícolas modernas é o monitoramento (*caminhando pelo campo*). No entanto, uma navegação autônoma confiável continua um desafio. Um robô precisa enfrentar o dinamismo do campo agrícola e obstáculos imprevisíveis, e.g. humanos e máquinas. Em particular, o milho e o sorgo apresentam uma dificuldade adicional devido à forma padrão de cultivo: fileiras espaçadas por menos de um metro de largura que ficam ainda menos visíveis em estágios posteriores devido à densa cobertura e espalhamento das folhas. Tal condição influencia fortemente os sensores, provocando frequentes oclusões, erros de leitura e outras situações fora de sua faixa de trabalho. Nesse contexto, surgem três questões: 1) *O potencial inexplorado do sensor LiDAR é suficiente para interpretar um ambiente de cultura de ruas estreitas sem marcos artificiais?* 2) *A busca da melhor reta para representar fileiras de cultura retrata o problema?* 3) *Como a estimativa da distância lateral pode ser melhorada através da fusão de sensores?* Para responder às três perguntas, ***Perception LiDAR*** (***PL***) foi desenvolvido para estimar a distância lateral às fileiras com um LiDAR 2D como sensor principal. O filtro Kalman estendido permite o uso de odometria e medições inerciais. A aferição manual dos dados mostrou que a tarefa de encontrar a melhor reta a partir dos dados LiDAR é desafiadora e pode ter somente 54% das estimativas com erro inferior a 0,05 m. No entanto, o método proposto permitiu a operação autônoma de vários robôs por 72 km. Devido ao sinal RTK-GNSS ser pouco confiável sob cobertura, as estimativa por ***PL*** superam significativamente o posicionamento baseado em GNSS, que pode até indicar que a plataforma está em outra rua. O extenso teste de campo ocorreu em vários campos de milho e sorgo entre 2017 e 2020. Para ruas contínuas, ou seja, existe pelo menos uma das fileiras laterais, a taxa de sucesso para terminar o segmento desejado com navegação autônoma é de 89,76%. O desempenho superior ao remover grande parte de objetos diferentes de caule da leitura do sensor, e também a concentração de falhas nas lacunas e quando há oclusão do sensor, ambas situações com fileiras pouco a não visíveis, indicam que o problema não é o de melhor ajuste de reta, mas sim classificação em que o objetivo final é encontrar caules. Em resumo, embora ***PL*** não forneça uma navegação totalmente livre de intervenção entre as fileiras, suas capacidades atuais liberam os operadores da tediosa tarefa de dirigir manualmente o robô o tempo todo e pavimenta o caminho para um robô agrícola totalmente autônomo.

Palavras-chave: Robótica Móvel. Robôs Agrícolas. Percepção. LiDAR.

LIST OF FIGURES

LIST OF TABLES

LIST OF ABBREVIATIONS AND ACRONYMS

CTE	Cross Track Error
DASLab	Distributed Autonomous Systems Laboratory
DGNSS	Differential Global Navigation Satellite System (level of GNSS accuracy)
EKF	Extended Kalman Filter
GNSS	Global Navigation Satellite System
GT	Ground Truth
IMU	Inertial Measurement Unit
LabRoM	Mobile Robotics Laboratory
LiDAR	Light Detection and Ranging
LW	Lane Width
MLSS	Multi-Layer Sensing System
PL	Perception LiDAR
PVC	Polyvinyl Chloride
RS	Row Spacing
RTK	Real Time Kinematics
RW	Robot Width
SLAM	Simultaneous Localization and Mapping
SPS	Standard Positioning Service (level of GNSS accuracy)
TS	TerraSentia

LIST OF SYMBOLS

α	Angle between fitted line to adjacent row and robot's longitudinal axis
b	Intercept of fitted line
d	Lateral orthogonal distance between LiDAR and crop row
Δd	Difference between previous and current lateral distance estimates
l	Length of fitted line to crop row
λ	Associated reading angle for a LiDAR's distance measurement
L_{offset}	Longitudinal distance between robot's mass and sensor centers
m	Slope of fitted line
np	Number of points used to fit the line
ω_z	Angular speed around z-axis
Q_k	Process noise covariance matrix for instant k
R_k	Measurement noise covariance matrix for instant k
r	LiDAR's distance measurement
sd	Standard deviation of a fitted line with respect to original points
ϕ	Orientation difference between crop lane and robot longitudinal axes
v_x	Forward linear speed

CONTENTS

1 INTRODUCTION

According to United Nations projections, even if the decline of fertility accelerates, it is almost inevitable to have continued population growth until 2050. With 95% confidence, population will be between 9.2 and 10.1 billion people in 2050 from the 7.3 billion in mid-2015 (Department of Economic and Social Affairs of the United Nations, 2015). Such estimate continues valid after 2019 revision (United Nations DESA, 2019). Besides that, estimates of (FAO; IFAD; WFP, 2015) in the period 2014-2016 indicate around 795 millions of people - one every nine - are undernourished. Both facts support the projections made by Food and Agriculture Organization of the United Nations: Global production of food must increase by 70% until 2050, relative to 2009 levels (FAO, 1975). Hunter, Smith, Schipanski, Atwood and Mortensen (2017) provides a recalibrated target of approximately 25%-70% increase, relative to 2014 levels, to meet the demand for 2050. The authors state that although global agricultural output is in the right direction towards that goal, there is an even greater challenge to restore and maintain ecosystem functioning. Instead of the current increasing trend, dramatic drop must occur in both nutrient losses and greenhouse gas emissions from agriculture.

In this scenario, both precision agriculture and phenotyping have attracted great interest in the pursuit of greater sustainability (CHAWADE, 2019; FINGER, 2019; BONGIOVANNI; LOWENBERG-DEBOER, 2004). A key point for the first is mapping the soil variability, disease/growth monitoring across field. And for the second, a repetitive and frequent collection of phenotyping data under field conditions is fundamental. Additionally, weed control without chemicals has increasingly becoming a necessity due to rising number of superweeds world-wide (GILBERT, 2013). Although all three may have different procedures, the essential task for them is scouting (Fig. 1). Blackmore (2016) defines crop scouting as the *"the process where a person walks through the crop assessing health and looking for abnormalities"*. Currently, this highly time-consuming and labor-intensive task requires humans to go to field.

While on one side we see specialized workers spending time to collect data (phenotyping), on the other side there are a multitude of workers manually removing weeds, putting their health at risk. Aerial-based research platforms have been on the rise as they are easy to deploy and they can cover large distances in short times. But they still have several limitations as the payload, flight time, can not interact with crop e.g. for mechanical weed control and most importantly, they are mostly unable to enter the crop and therefore unfit to measure under canopy phenotypes (MUELLER-SIM, 2017).

Deployment of mechanical power, such as tractors, usually follows the sequence given by Tab. 1. The power intensive work benefits from mechanization as it greatly

Table 1 – Sequence of Mechanization

	Operation		
Sequence	First Stage	Second Stage	Third Stage
Type of Operation	High Power Low Skill	Medium Power Medium Skill	Low Power High Skill
Mobile	Land preparation, Transport	Seeding of grain, harvesting of grain	Transplanting, Harvesting of Cotton, Fruits & Vegetables, Sugarcane

Source: (RAI, 2009 apud KIENZLE, 2013, p. -105)

reduces drudgery while also being more time and normally cost efficient than hand work (KIENZLE, 2013). The second stage greatly benefits from standardized plantation as row planting which facilitates the use of self-propelled harvesters, for example. Finally, the last stage refers to tasks that require low power but high dexterity. Besides the mentioned activities in the table, scouting is an additional example due to its expected low interference with environment and possibly none to few material collection. In this sense, although tractors with automatic guidance may be available, they are not immediate candidates due to soil erosion, fuel costs and especially for the higher crops, a tractor may not even enter the crop without damaging it. This unveils a gap that can be filled with small ground mobile robots. Indeed, van Henten in King (2017) states that a single large machine to cover as much area as possible is needed while someone needs to drive it. Once a human driver is removed, size becomes irrelevant.

The world is facing a scenario where efficient usage of agricultural inputs is fundamental both for economical and environmental reasons and operation errors can be drastically reduced. In this context, the introduction of robotics as autonomous vehicles can be seen as a valuable technological tool for modern agriculture practices. Moreover, this has the advantage of being able to apply diverse robotic control theories, already well-founded in applications of other areas (GRIFT, 2008).

Figure 1 – An aerial footage of TerraSentia robots scouting corn field.

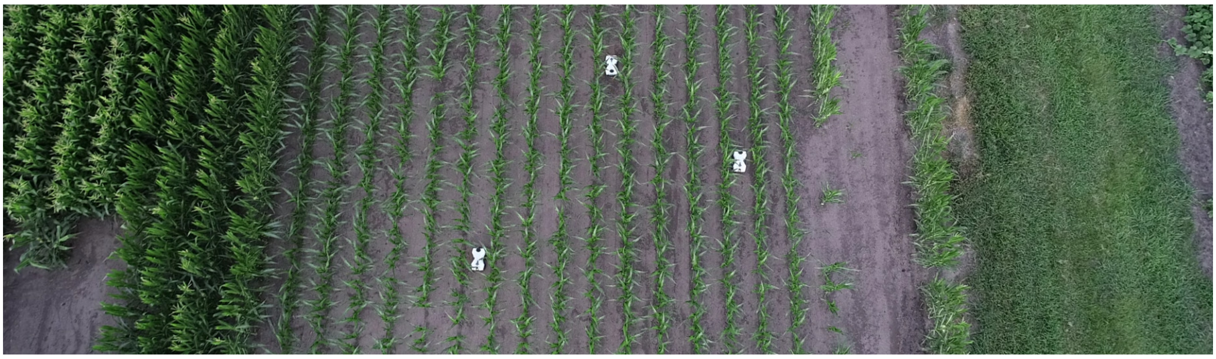

Source: DASLab archive. Credits to DASLab for video footage and EarthSense for the robots.

In this context, Mobile Robotics Laboratory (LabRoM) at School of Engineering of São Carlos - University of São Paulo (EESC-USP) has been researching mobile robots for agricultural purposes since 2010 in the pursuit of the question: *"How do we enable autonomous robots in agricultural fields?"*. For such endeavor, LabRoM has engaged joint researches with Instrumentation branch of Brazilian Agricultural Research Company (Embrapa) and Distributed Autonomous Systems Laboratory (DASLab) at University of Illinois at Urbana-Champaign (UIUC).

1.1 Motivation

While scouting is a general activity for agriculture, providing such task for corn has a great potential. Precision agriculture, phenotyping and weed control will greatly benefit both Brazil and United States. According to USDA most recent report (MCCONNELL, 2021), world production for 2020/2021 is projected to be 1,134.1 million tons, where the two countries are responsible for 41% of the total. Around 35% of crop production usually go to animal feed, but in Brazil, between 50% to 60% of corn production is destined to that. Indeed, both countries play a major role in global poultry exports, contributing with 52.4% of world total (U.S. Department of Agriculture, 2020). Therefore, improvements in corn production have also impact on another industries.

Figure 2 – Example of width measurement in sorghum field (a) manually done (b) TerraSentia robot collecting visual data (c) Width estimation from recorded data.

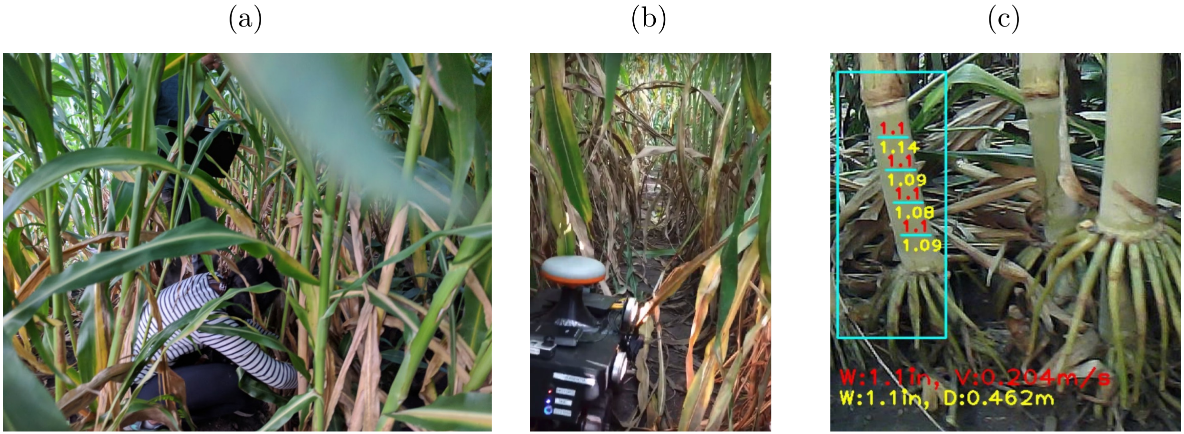
(a) (b) (c)

Source: extracted from Choudhuri and Chowdhary (2018).

The joint research with DASLab brought the need to autonomously navigate in energy sorghum, a key crop for the biofuels industry in the US Midwestern. This is a particular case where phenotyping was already being manually conducted by researchers and autonomous systems could showcase their potential (YOUNG, 2019; CHOUDHURI; CHOWDHARY, 2018). Figure 2a shows manual extraction of width measurement in sorghum plants. Then, TerraSentia robot records visual data from embedded side cameras (Fig. 2b). Such collected data is offline processed to estimate width (Fig. 2c). The study

Figure 3 – Modules present in a mobile robot system.

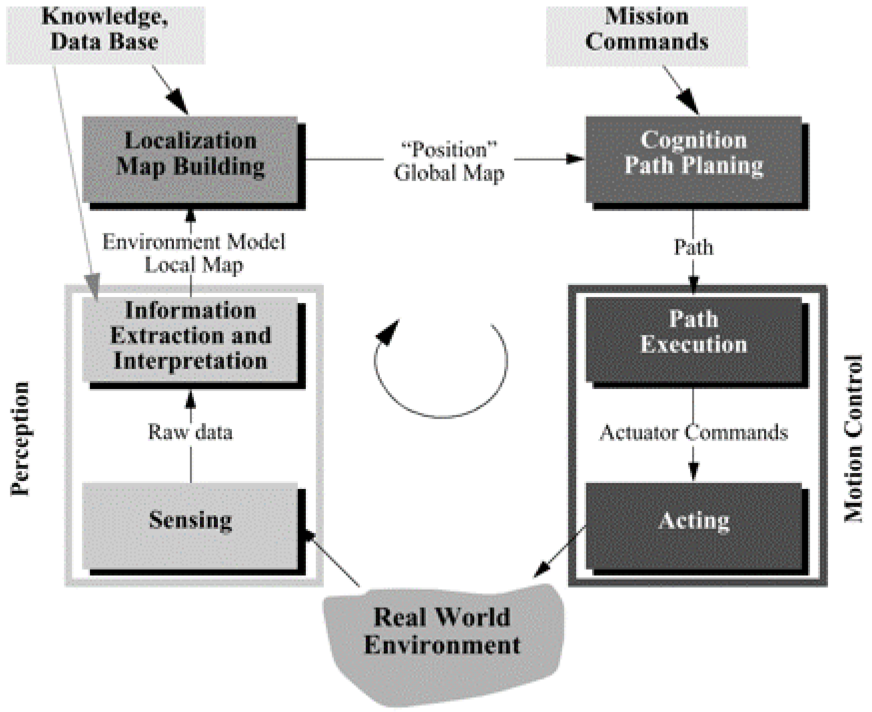

Source: retrieved from Siegwart, Nourbakhsh and Scaramuzza (2011).

reported 98.2% estimation agreement when compared against trained agronomists measurements. Such process can be further streamlined with autonomous robots. Fortunately, the sorghum research fields share similarities with corn fields, i.e. narrow sub-meter crop lanes, vertical growth that limits platforms that cannot fit within a single lane and expressive number of hanging leaves.

According to Siegwart, Nourbakhsh and Scaramuzza (2011), navigation is one of the most challenging competences required from a mobile robot. It can be further divided into high-level and low-level tasks as displayed by Fig. 3. Siegwart and colleagues also state that *"Robotics is peculiar in that solutions to high-level challenges are most meaningful only in the context of a solid understanding of the low-level details of the system"*. Within low-level tasks, while the motion control is tightly related to the available robotic platforms for this study, perception is not only sensing but it refers to extraction and interpretation of sensor readings to obtain knowledge about environment. Therefore, since robots are already under development by LabRoM and its partners, a perception subsystem is fundamental towards autonomous navigation.

Bechar and Vigneault (2016) provides a review on agricultural robots and special attention is given to devices used for sensing and self-localization, mainly those considered external sensors. They obtain current state of the environment relative to the position of the robot and its components. Examples of such type of sensor are: machine vision, Light

Detection And Ranging (LiDAR) and Global Navigation Satellite System (GNSS).

LabRoM's experience with LiDAR-based navigation in warehouse and urban environments coupled to advantages of LiDAR sensors in agricultural applications (MOUSAZADEH, 2013) and low attention given to this sensor (HIREMATH, 2014) motivates the development of a LiDAR-based perception subsystem for the narrow sub-meter lane crops such as corn and sorghum. Indeed, literature review shows an on-going gap in this area. Additionally, as field robotics greatly differs from the well-established indoor counter part, there is an expressive lack of field testing report and discussion of autonomous robots in agricultural fields, especially in the narrow lane crops.

1.2 Research Problem

The problem to be researched in this study is *How do we enable a ground mobile robot to understand its surroundings within narrow lanes of agricultural crops such as corn and sorghum?*

1.3 Objectives

Given the motivations and research problem, the ultimate objective of this study is a perception subsystem to enable autonomous scouting within narrow lanes of crop fields such as corn and sorghum. To achieve it, specific objectives are required:

- Lateral distance estimation within crop lanes;
- Implementation on lightweight ground mobile robots;
- Extensive field testing.

1.4 Research Questions

The main research questions that guided this study are:

Is it possible to develop a perception subsystem for narrow lanes, without artificial landmarks, using a LiDAR sensor?

How can the problem of navigating within narrow lanes be constrained to improve computational costs and allow field deployment?

Does the application of least squares linear regression on suitably chosen sensor data avoid the necessity to recur to computationally intensive methods to extract lines in LiDAR data?

1.5 Main Contributions of this Study

- Temporal, geometric and user-defined constraints on the lateral distance estimation problem to enable a low-computational cost and fast perception subsystem;
- Strong field experiments with over 72 km of autonomous navigation relying on the proposed perception subsystem.

1.5.1 Work Organization

Chapter 2 presents a literature review about the current status of autonomous agricultural robots. Then, Chapter 3 exposes the core sensor, robotic platforms, experimental sites, methods and performance indicators. Subsequently, Chapter 4 shows and discusses field experiments. Finally, Chapter 5 concludes this document.

2 LITERATURE REVIEW

In the context of increasing agricultural production with both environmental and labor health protection, autonomous robots in farms have been a rising research field and are becoming inseparable parts of the modern farms (SHAMSHIRI, 2018). Indeed, the importance of autonomous navigation in agriculture has been recognized since 1940s, when Frank A. Andrew patented a 'driverless' tractor controlled by cable as it winds around a stationary pole as shown by Fig. 4 (ANDREW, 1941). Even before, attempts to improve farm practices date back to the 1920s with the first patent of a steering attachment for tractors to guide the vehicle along/parallel to existing furrow (WILLRODT, 1924). Nonetheless, because agricultural machines frequently operate on uneven terrains, the creation of robots that have the ability to travel and realize a variety of tasks on unknown surfaces, either autonomously or remotely-operated, remains a challenge (TAROKH, 2013; VIDONI, 2015).

Figure 4 – Both top and side views of Frank Andrew's invention. There is a stationary pole in the center and the tractor is guided using a cable.

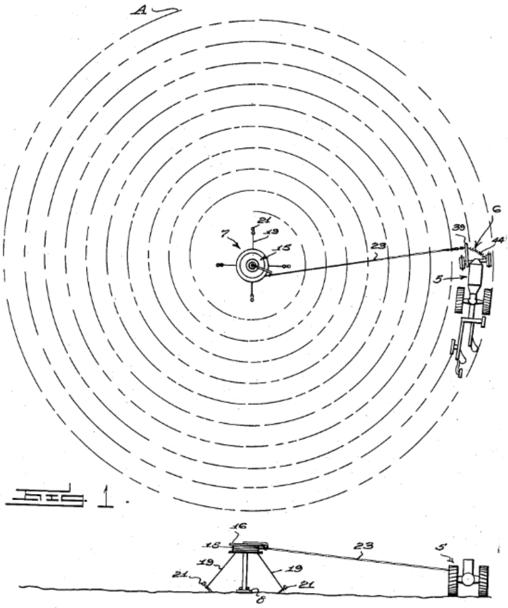

Source: retrieved from Andrew (1941).

Fountas, Mylonas, Malounas, Rodias, Santos and Pekkeriet (2020) provides a systematic review on research and commercial agricultural robotics used in crop field operations. It highlights that the most explored robotic systems were related to harvesting, weeding and crop scouting. The authors pointed out that the key factors for development of agricultural robots are: 1) Labour-intensive field operations either due to their complexity or because of they are related to sensitive plants; 2) Required repetitiveness throughout crop production cycle. For example, intra-row weed control is a hard-to-achieve task with traditional field machinery and that is currently achieved with human workers. Although a rising need, according to (MARINOUDI, 2019), the crop field operations with autonomous tractors and robotic platforms is still developed at research stage.

In their review of robotics in horticultural fields, Bechar (2010) discusses that robotic systems cost must be sufficiently low to match the relatively low value of horticulture produce, which can be extended to several other agricultural crops. The question of safety and reliability is also raised as a major concern to allow autonomous system operations in open fields. Another key point is about reduction of systems' dimensions in the pursuit of less environmental impact due to soil compaction, over-application of chemicals and coverage overlapping.

2.1 Global Navigation Satellite System (GNSS)

Relying on a constellation of satellites, GNSS provides information of positioning and timing on a continuous, worldwide basis with no direct charge (FARRELL, 2008). Different levels of accuracy can be achieved with GNSS receivers. Using Standard Positioning Service (SPS), a well-designed GNSS unit with a clear view of the sky and receiving at least four satellite signals can achieve 3 to 8 meters positioning accuracy (USA Department Of Defense, 2008). GNSS pseudorange measurements and mobile communication networks (4G or WiFi) enable real-time differential GNSS (DGNSS) to achieve 1 to 3 m accuracy (KAPLAN; HEGARTY, 2006). Finally, Real-Time Kinematic (RTK) is able to achieve centimeter accuracy using carrier phase measurements and resolving integer ambiguity. According to Zhao and Zhang (2016), Yan, Wang, Jin and Shi (2016), while integer ambiguity resolution is a well-researched topic for dual-frequency receivers, it is still very challenging for a single-frequency receiver.

For agricultural purposes, GNSS-based navigation systems have been widely used to allow automatic guidance of traditional crop machinery such as harvesters (STOLL; KUTZBACH, 2001; PILARSKI, 2002) and tractors (BELL, 2000; THUILOT, 2002; LENAIN, 2003; ABIDINE, 2004; BLACKMORE, 2004; NØRREMARK, 2008; ZHANG, 2016; WANG; NOGUCHI, 2016). GNSS has also been used on smaller over-the-canopy autonomous robots (BAK; JAKOBSEN, 2004; BAKKER, 2011). However, under dense crop canopies, the GNSS readings deteriorate due to occlusion, attenuation, and multi-path errors. A reported example is Robotanist, a thin robot capable of driving through a single lane to automate the phenotyping process in sorghum crops (MUELLER-SIM, 2017). The authors highlight that GNSS navigation is a capability to be lost as season progresses and sorghum plants becomes taller than GNSS antenna. Figure 5 shows an example for platforms used for GNSS-based navigation research and their background show the conditions where they usually operate.

Figure 5 – Examples of GNSS-based works using (a) A conventional agricultural machine; (b) An over-rows robotic platform; (c) Narrow single lane robot.

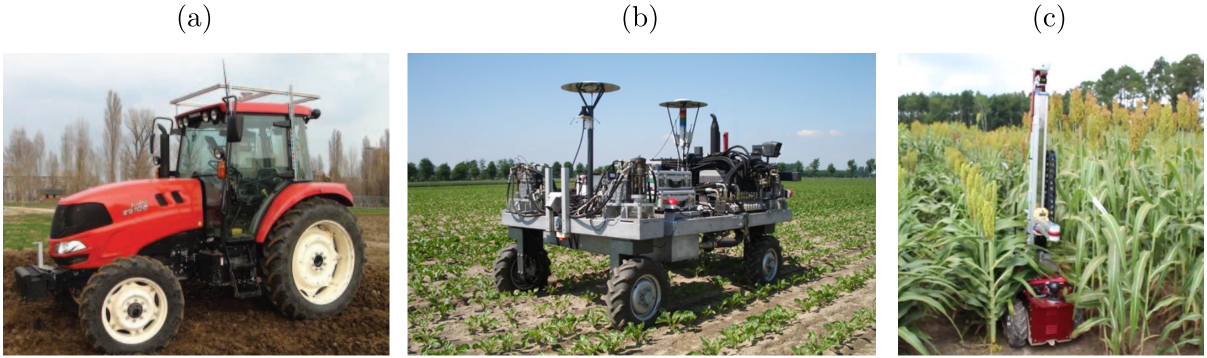

Source: (a) retrieved from Wang and Noguchi (2016) (b) retrieved from Bakker, Asselt, Bontsema, Müller and Straten (2011) (c) retrieved from Mueller-Sim, Jenkins, Abel and Kantor (2017).

South Atlantic Magnetic Anomaly (SAMA) may degrade the GNSS data quality in several countries in South Hemisphere since it affects from West Africa to South America and from Equator to Antarctica (ABDU, 2005; SPOGLI, 2013). Due to this anomaly, trans-ionospheric signals, such as those from GNSS satellites, present irregular behavior. Therefore, reliability of GNSS-based navigation systems is compromised. Additionally, some obstacles (e.g. buildings, fixed places to avoid) can be mapped but GNSS is unable to identify dynamic and unexpected ones such as animals, humans, stubble, or machines. Therefore, GNSS alone cannot provide safe autonomous navigation of mobile robots in agricultural environments (REINA, 2016). Allied to that, Rovira-Más, Chatterjee and Sáiz-Rubio (2015) affirms that redundancy and continuous fail-safe checking are required for long-term navigational solution stability in agricultural field because of multi-path reflections and unpredictable signal-blockage. The cited works may not experience these issues as the platforms are big enough to allow the receiver to be well above the canopy. But this cannot be said when the vehicle operates under canopy, such as in orchards (BERGERMAN, 2015), vineyards (SANTOS, 2015) and late seasons corn and sorghum (MUELLER-SIM, 2017).

Subsequently, a lot of research has been placed on GNSS-free systems capable of autonomously navigating robots through crop lanes. For such purpose, devices that captures the robot's surroundings are usually employed: camera and LiDAR. The first is a highly versatile sensor, usually operating in the infrared, near-infrared or visible spectrum to extract both color and depth information, while the second accurately measure a relative vectorial position (distance and direction) of nearby objects (BECHAR; VIGNEAULT, 2016).

2.2 Cameras

The crop-row identification has been actively tackled with cameras (MONTALVO, 2012; JIANG, 2015; ZHAO; ZHANG, 2016; ZHAI, 2016). Although different processing methods are used, a common characteristic between them is the need of an image from above canopy. Figure 6a shows an usual output of such systems. Moreover, such vision-based systems are usually developed for tractors (Fig. 6b), which have three characteristics in advantage to small vehicles: 1. A higher camera position allows a broader view, consequently a single image contains information for several meters ahead; 2. GNSS systems are reliable and they can be used between processing loops to keep the vehicle on track; 3. Soil unevenness has less effect on larger vehicles.

Figure 6 – (a) Output example of a vision-based crop row detection where red lines show the detected rows; (b) A tractor equipped with a camera on its top to detect rows in early stages of corn. The region of Interest (ROI) is delimited by the red rectangle in front of the tractor and it refers to the region within camera picture that will be used to detect the rows.

Source: (a) retrieved from Jiang, Wang and Liu (2015); (b) retrieved from Guerrero, Ruz and Pajares (2017).

Albeit successful identification of crop rows on recorded data, subsequent field testing has usually not been reported. When reported, it was restricted by lighting conditions (MORIMOTO, 2005; TILLETT, 1998), limited to few experiments (ZHANG, 2018; RADCLIFFE, 2018; HIREMATH, 2014; XUE, 2012; SUBRAMANIAN, 2006), not used for autonomous navigation (BAKKER, 2008) or tested on simulated environments, either software simulators (XAUD, 2019; DØRUM, 2015) or a physical one (ORTIZ; OLIVARES, 2006). Figure 7 shows an example for each type of simulations. Note that they do not consider ground unevenness, straying leaves, presence of weeds or other irregularities.

Guerrero, Ruz and Pajares (2017), García-Santillán, Montalvo, Guerrero and Pajares (2017) detect straight crop rows even in the presence of weeds in early stages of maize fields.

Figure 7 – Simulated environments to validate the row detection (a) Software simulator (b) Mock-up setup.

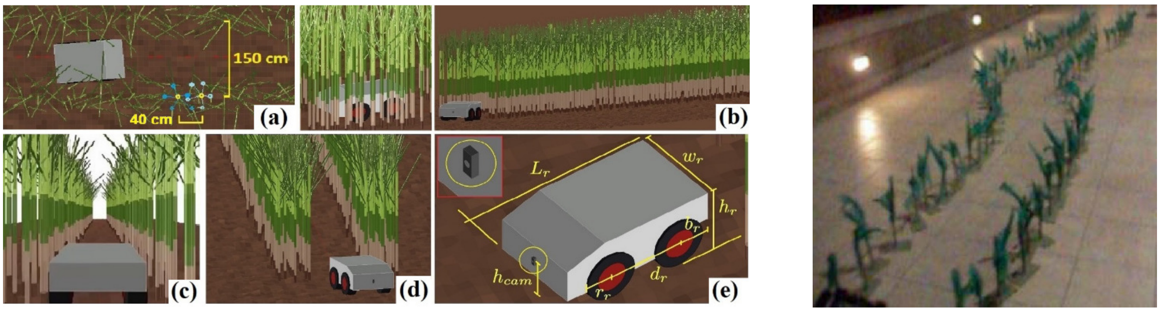

(a) (b)

Source: (a) retrieved from Xaud, Leite and From (2019); (b) retrieved from (ORTIZ; OLIVARES, 2006).

The first uses such knowledge to fine tune a GNSS-based navigation for increased crop safety. Also in maize field, (HIREMATH, 2014) shows an image-based particle filtering for navigation with a small robot (Fig. 8a). But it requires a downward-looking camera at a height of 1.65 m (Fig. 8b), thus limiting the use of such method in later crop stages. Moreover, the system was only tested for plant sizes in the earlier stages (ranging from 0.1 m to 0.8 m).

Figure 8 – (a) Robot used for autonomous navigation in corn crops tested until plants reach height of 0.8 m. Note the downward-facing camera at the top of the mast and a 2D LiDAR fixed on the front part of the robot, next to the wheel; (b) A top view provided by camera.

(a) (b)

Source: both retrieved from Hiremath, Evert, Braak, Stein and Heijden (2014).

The common issues of illumination sensibility and requirement of knowledge about crop-specific features such as color, spacing and periodicity are addressed by English, Ross, Ball and Corke (2014). They introduced a method that extracts and tracks the direction and lateral offset of the dominant parallel texture in simulated overhead view of the scene. However, it still requires the view from above canopy. Additionally, the method assumes a leveled camera attitude with respect to the ground. Again, a larger vehicle has advantage as it tends to sit relatively flat to local terrain, allowing such attitude condition for the camera even if an external stabilization is not performed.

2.3 Light Detection and Ranging (LiDAR)

Laser instruments, as the LiDAR, have the advantage of providing non-contact measurements. For this reason alone, they are of great interest for many industrial applications (AMANN, 2001). Moreover, as laser scanners provide direct measurements of objects in the world, they are well suited for the task of obstacle detection and localization in mobile robotics (SIEGWART, 2011). Among others, several works (POULIOT, 2012) and (REINA, 2016) justify usage of such sensors in mobile robotic applications: Range detection, simple computing, good acquisition speed and improved robustness in outdoor conditions accompanied by drop in their price.

Interestingly, although laser rangefinders were already being researched on mobile robots since 1980s (LEWIS; JOHNSTON, 1977), Hague, Marchant and Tillett (2000) points out that, until 2000s, LiDAR was only reported in agricultural applications to be used as part of a *total station*, therefore requiring laser mounted on vehicle and detectors positioned around the workspace or the other way around. Subsequent communication link between such fixed detectors and vehicle is necessary to report detection time for triangulation by the positioning system. This agrees with stated by Hague, Marchant and Tillett (2000), page 11: "Whilst interest in automated agricultural vehicles has endured, it has done so in relative isolation from the field of mobile robotics."

In the case of row following tasks, most LiDAR researches aimed orchards (BARAWID, 2007; Ji Zhang, 2013; BERGERMAN, 2015; BELL, 2016; LEMOS, 2018). Figure 9 shows two examples of such works. Indeed, Bergerman, Maeta, Zhang, Freitas, Hamner, Singh and Kantor (2015) has proved that 2D LiDAR provides enough information for row following in well-structured tree rows. They use a family of autonomous orchard vehicles relying on two-dimensional laser scanner, wheel and steering encoders for its perception. Capable of row following and turning, such robots replace ladders used by workers to collect fruits. According to the authors, such change brought up to 58% efficiency gains for fruit production tasks while also improving safety and comfort to orchard work.

A commonly employed LiDAR solution when ground vegetation occludes tree trunks is the use of 3-D point clouds (BELL, 2016; Ji Zhang, 2013). The first uses a Velodyne VLP-16 3D laser scanner to enable autonomous navigation of a Pioneer P3-AT robot in pergola structured orchards (Fig. 10a), where a sparse array of trunks and posts hold up a canopy, which resembles a ceiling. Ji Zhang, Chambers, Maeta, Bergerman and Singh (2013) used a custom-built 3D unit to retrieve a 3D point cloud to address navigation when tree canopies are irregular and high weeds are present. Such module

Figure 9 – Examples of 2D LiDAR being used to guide (a) Tractor (b) Orchard platform.


(a) (b)

Source: (a) retrieved from Barawid, Mizushima, Ishii and Noguchi (2007); (b) retrieved from Bergerman, Maeta, Zhang, Freitas, Hamner, Singh and Kantor (2015).

was constructed by adding a rotational degree of freedom to a planar LiDAR with the use of a motor (Fig. 10b). It is a lower cost solution compared to the Velodyne VLP-16, but adds complexity to the system, either construction itself or maintenance. Another interesting option is using a single 2D LiDAR in push-broom configuration where a fixed 2D scanning device populates a 3D point from being "pushed" through environment by a vehicle (BALDWIN; NEWMAN, 2012).

Figure 10 – (a) Pergola structure of a kiwifruit orchard (b) Custom-built 3D unit.


(a) (b)

Source: (a) retrieved from Bell, MacDonald and Ahn (2016) (b)retrieved from Ji Zhang, Chambers, Maeta, Bergerman and Singh (2013).

Riggio, Fantuzzi and Secchi (2018) also highlights the issues from using RTK-GNSS (requirement of base station and multiple connections to GNSS satellites) and cameras (performance affected by illumination conditions). They use a Pioneer 3-AT robot to navigate through vineyard to collect data for yield estimation. To follow row, the robot uses a SICK S300 Expert laser scanner limited by software to mimic less expensive devices, although specific limitations are not clear. To filter out probable readings from tall grass, weeds, hanging twigs or even ground when laser scanner is tilted due to rough terrain, the method rejects points that do not have the expected distance between trunks. The line following state showed a distance error with mean value less than 0.05 m and value within 0.1 m more than 93% of time.

Corn and sorghum fields crops greatly differ from orchards. Instead of well-defined tree trunks, weeds and hanging leaves can be easily mistaken with or even occlude the stems in the mentioned crops. Normal spacing between tree rows is few meters while it is around 0.8 m in corn/sorghum. Hence, a dense and cluttered environment is expected for such crops, especially in later growth stages. In corn crops, some researches with LiDAR-based row-following systems can be found (HIREMATH, 2014; TROYER, 2016).

Hiremath, Heijden, Evert, Stein and Braak (2014) introduces a particle filter (PF) algorithm for autonomous navigation in corn fields. The PF can handle different kinds of uncertainties, e.g. noise due uneven terrain and the varying colors, shapes and sizes of the plants, while still accurately estimating the robot heading and lateral deviation. Nevertheless, such method is restricted to plants smaller than 0.6 m. Therefore, it is not certain if the system can handle leaves extending to the middle of the lanes.

A row-following platform is demonstrated by Troyer, Pitla and Nutter (2016). Although it uses only two single-reading LiDAR sensors, it presented reasonable results for the indoor case. But even with a flat terrain and PVC representing corn plants, the system failed. Indeed, as the sensors provide a single distance reading at a time, only one measurement is available for each side, and it may not even correspond to the stem.

2.3.1 Mapping

Another approach is to generate a map and use it to navigate. Shalal, Low, McCarthy and Hancock (2015) remotely controls the CoroWare Explorer platform (Fig. 11a) through persimmon orchard to collect sensory data and construct an offline map to be used as an *a priori* map for subsequent robot localization.

The origins of the Simultaneous Localization and Mapping (SLAM) problem occurred at the 1986 IEEE Robotics and Automation Conference held in San Francisco. It asks if a mobile robot placed at an unknown environment can incrementally generate a consistent map while simultaneously locating itself within this map. Durrant-Whyte and Bailey (2006) stated that SLAM could be considered a solved problem at theoretical and conceptual level, but acknowledged that substantial issues remained to implement more generic solutions. Indeed, although a practical SLAM would lead to truly autonomous robots, very few successful cases due to SLAM usage on autonomous robots in agricultural fields have been reported.

Both Christiansen (2011) and Cheein, Steiner, Paina and Carelli (2011) report successful online implementations of EKF-SLAM to orchards and EIF-SLAM to olive groves, but the vehicles were always manually steered. The first fused data from SICK LMS-

200 LiDAR, ADIS1650 6DOF Inertial Measurement Unit (IMU) and RSA 607 CANopen absolute encoder on wheels while the second used a combination of 30 m range SICK 2D LiDAR and a Bumblebee 2 stereo camera (only one of the cameras was used). Figure 11b shows the platform and the orchard where data was collected for the first. Figure 12a shows one of the Cheein, Steiner, Paina and Carelli (2011) mapping process. Note that the lane is wide and there are well-defined trunks.

Figure 11 – Platforms used to collect field data (a) A small prototype (b) A tractor.


(a)

(b)

Source: (a) retrieved from Shalal, Low, McCarthy and Hancock (2015); (b) retrieved from Christiansen (2011).

Santos, Sobreira, Campos, Santos, Moreira and Contente (2015) and Lepej and Rakun (2016) ran their SLAM implementations on recorded data from vineyard (Fig. 12b), apple orchard (Fig. 12c)/vineyard(Fig. 12d) respectively. The first uses Hokuyo URG-04LX-UG01 LiDAR, Sparkfun 9DOF Razor IMU, Omron E6A2-CW5C wheel encoder, RFID (Radio-Frequency IDentification) tags and GNSS for the mapping and localization while the second relies only on a SICK TIM 310 LiDAR sensor. Although localization performance was deemed sufficient for autonomous navigation purpose, such SLAM implementations have not been reported on robots autonomously navigating on those fields.

Astolfi, Gabrielli, Bascetta and Matteucci (2018) reports field experiments of a Husky robot autonomously navigating through vineyard (Fig. 12e) with the support of a map. The mapping phase offline reconstructed such map with data collected manually driving the robot. The authors state that soil changes and the time difference between map generation (with logged data on winter therefore bare vegetation) and field testing (summer time with vines full of leaves and grass on the terrain) posed difficulties in autonomous navigation which were currently being worked on.

2.4 Discussion

Chapter 1 provides an overview of current agricultural approaches to meet future demands. In particular, next level precision agriculture, phenotyping and weed control

Figure 12 – Environments where some mapping was tested (a) Olive grove; (b) Mountain terraced vineyard; (c) Apple orchard; (d,e) Vineyard.

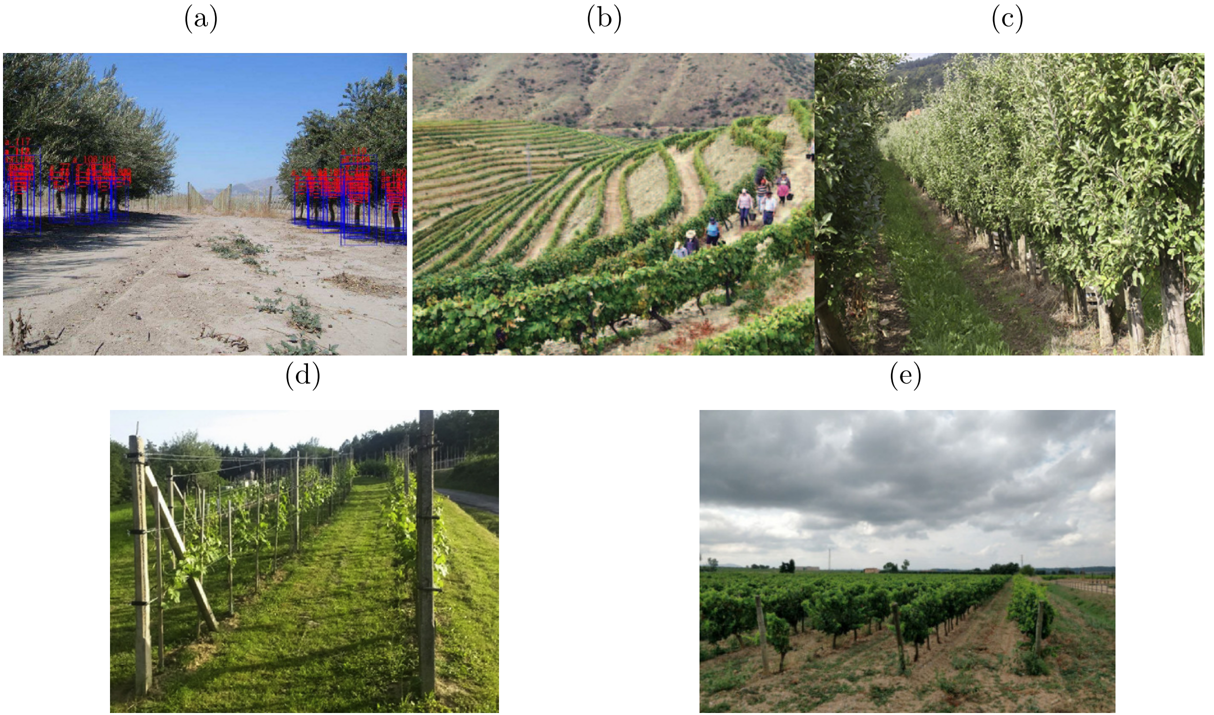

(a) (b) (c)

(d) (e)

Source: (a) retrieved from Cheein, Steiner, Paina and Carelli (2011); (b) retrieved from Santos, Sobreira, Campos, Santos, Moreira and Contente (2015); (c) and (d) retrieved from Lepej and Rakun (2016); (e) retrieved from Astolfi, Gabrielli, Bascetta and Matteucci (2018).

have a common basic task: Crop scouting. Since it is a repetitive, tedious, labor intensive and time-consuming task, there are clear motivations to use autonomous platforms.

Indeed, according to Shamshiri, Weltzien, Hameed, Yule, Grift, Balasundram, Pitonakova, Ahmad and Chowdhary (2018), "*weed control and precise spraying are perhaps the most demanded applications for agricultural field robots*". Rapid advances in plant breeding have been capped due to *phenotyping bottleneck*, caused by current phenotyping practices being highly labor intensive, costly nature and prone to human measurement errors (FURBANK; TESTER, 2011; RAHAMAN, 2015). To overcome such issues, Fahlgren, Gehan and Baxter (2015) highlights the rise use of vision-based high-throughput phenotyping platforms. Suprem, Mahalik and Kim (2013) states that *"soil sampling is the foremost process in the field of precision agriculture."* In such context, Embrapa Instrumentation has been conducting researches with laser-induced breakdown spectroscopy (LIBS) equipment aiming *in situ* soil analysis. All three solutions above bring significant improvement in agricultural practices, but they can be even further optimized if the robotic platform is also able to autonomously navigate the crop field.

Lightweight ground robots have the potential to fill the gap between heavy agricultural equipment and human utilized tools. They enable the execution of high-precision management (e.g. individual plants data collection) that otherwise would be too expensive or time consuming). Moreover, the lightness of these robots also prevents soil compaction, a common problem due to traditional machinery transit (BLACKMORE, 2016; TORGERSEN, 2014; BECHAR, 2010). Development and use of such lightweight ground robots also synergize with a current trend in agricultural field robotics towards swarm of small scale robots and drones (SHAMSHIRI, 2018). Despite mentioned advantages, a perception subsystem for a lightweight robot also faces challenges, which include limited computational/supply power onboard and greater influence from ground unevenness and environment (e.g. robot can be easily covered by vegetation).

Particularly, while orchards have been relatively synced with state-of-art robotics, the very few appearances of autonomous platforms that fit between narrow sub-meter crop rows emphasizes the existing knowledge gap about the latter environment. Indeed, as of 2016, extensive field testing of autonomous robots in agriculture has mostly been reported for cultures with ample space between rows, such as orchards (BELL, 2016; BERGERMAN, 2015), or for over-canopy robots for sub-meter crops (ÅSTRAND; BAERVELDT, 2005; TILLETT, 1998). Field experiments in narrow crops as corn have been either limited to few traveled distance (XUE, 2012) or to early stages (HIREMATH, 2014; HIREMATH, 2014). Some works were tested only in mock-up scenarios (TROYER, 2016) or simulators (XAUD, 2019).

Camera sensitivity to light usually limits the autonomous operation to certain periods of the day or requires frequent calibration (MORIMOTO, 2005). To mitigate this problem, many works use the camera under perspective projection, i.e. not coincident with the vertical/horizontal vehicle axes, (GARCÍA-SANTILLÁN, 2017; ENGLISH, 2014; GUERRERO, 2013; MONTALVO, 2012; ROMEO, 2012; PILARSKI, 2002) or even straight downwards ground (HIREMATH, 2014; TILLETT, 1998). Especially the last case, this physical requirement usually depends upon an overhead view of the field, thus limiting the operation on fields that greatly changes over season, e.g. corn and sorghum that after couple months can easily grow above 2 m. More recent approaches to address varying lighting conditions relies on neural networks and machine learning (XAUD, 2019), which strongly requires dedicated hardware such as GPU enabled computing units. Although costs and form-factors are rapidly becoming more accessible, embedding such computers on field robots is not trivial.

Although both types of sensor (LiDAR and cameras) are affected by weather phenomena (e.g. fog and rain) or other environmental factors (e.g. dust, smoke and occlusion), LiDAR are not as sensitive to illumination conditions as cameras. The range of view can also be larger for LiDAR (HIREMATH, 2014; REINA, 2016). Finally, the most interesting advantage of LiDAR is the capability to provide off-the-shelf distance measurements with accurate ranging over medium range (up to 30∼40 m) and fast operation (REINA, 2016). Indeed, Bergerman, Maeta, Zhang, Freitas, Hamner, Singh and Kantor (2015) has established that 2D LiDAR suffices for autonomous navigation in orchards. All the above highlights a clear research gap on extensive field testing of LiDAR sensors for narrow crops, such as corn and sorghum, whose height quickly becomes an issue and most platforms cannot travel through them.

The data provided by a 2D LiDAR can be seen on Fig. 13. Unlike indoor environments, there are no walls, i.e. continuous objects to follow. The rows form a loose resemblance of a corridor and due to the natural plant growth/movement of leaves because of weather, a similar configuration of a given position within crop is mostly unlikely as time passes. The lack of time-invariant landmarks (e.g. doors for buildings or slow growing orchard/vineyards/forestry trunks) poses a scenario of an ever-changing and long corridor. The author makes the hypothesis that such characteristics discourage usage of mapping techniques on crops similar to corn. Indeed, to the best of author's knowledge, no mapping researches on corn or sorghum has been developed up to 2020. Additionally, Aguiar, Santos, Cunha, Sobreira and Sousa (2020) concludes that the current state-of-art of localization an mapping in agriculture and forestry is still premature. Particularly towards autonomous navigation, only five of the 15 collected works have some field experiment, all in orchards or vineyards.

Figure 13 – Sample of 2D LiDAR scan within corn rows. The measurements allows direct range knowledge to nearby objects. Note the loose definition of a left row for $x \approx -0.5$ m and a right row for $x \approx 0.5$ m.

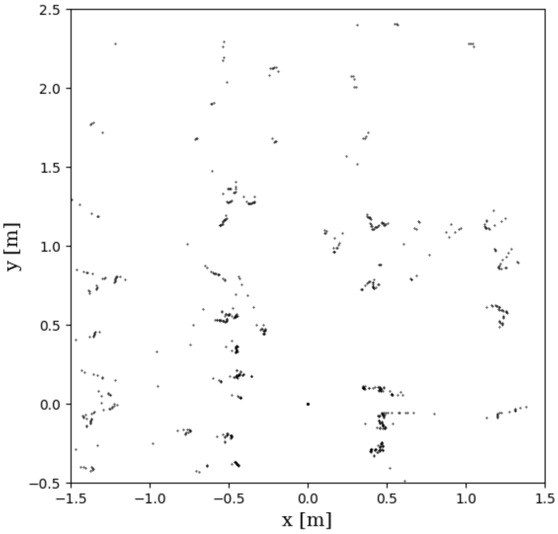

Source: author's own elaboration.

Although mapping may not be the goal due to previous hypothesis, the robot still needs to locate itself with respect to the lateral rows. Many works have addressed the task of lateral distance estimation as a problem of extraction of best line(s) on any given instant. Particularly with 2D LiDAR, which does not contain information other than range and intensity to a detected object, the assumption of existence of a best line weakens as the interaction between the LiDAR sensor and the surroundings becomes more frequent. In environments such as orchards (BERGERMAN, 2015), it is highly unlikely that the sensor will be totally or partially covered. But in corn and sorghum, the leaves from one row may be hanging further than lane's center and therefore, the physical interaction between sensor and environment becomes inevitable (Fig. 14a and 14b). From such low expectation of existence of a best lines to represent the rows, the author makes the hypothesis that line extraction methods such as Random Samples and Consensus (RANSAC), Hough Transform or many other computationally intensive methods (MALAVAZI, 2018; VIDOVIC, 2016) do not address the task. Instead, the application of least squares linear regression on a suitable section of the sensed data seems a cost-effective solution.

Figure 14 – Sensor readings for a robot driving through a corn crop. A forward-facing camera and a 2D LiDAR with its reading plane parallel to ground are both located in the front part of the robot. (a) Picture of incoming leaves in the middle of the lane (b) A LiDAR scan when the sensor encounters the leaves shown in (a).

(a)

(b)

Source: retrieved from Higuti, Velasquez, Magalhaes, Becker and Chowdhary (2018).

A building wall is usually continuous and consecutive LiDAR scans will provide much similar measurements to such wall except the borders and errors intrinsic to the sensor. However, due to the nature of crop rows, different parts of the row will be detected and because of that, considerably different lines are extracted from the scans. Additionally, ground mobile robots usually have dead reckoning, i.e. combination of robot's orientation/inclination measurement with appropriate velocity information to integrate movement over time and obtain a position estimate (SIEGWART, 2011). Since these two estimations lead to relative distances on space, they can be compared. Therefore, there is a need to handle the discontinuities and to allow sensor fusion.

In this context, Kalman (1960) presents a recursive filter for state estimation of stochastic discrete-time linear dynamic systems, commonly known as Kalman Filter. Indeed, the problem above requires the estimation of an state, the true value of position on space with respect to rows. Also, it is a dynamic system that is measured/estimated on discrete time intervals from the intrinsic nature of used digital devices. It is also subject to stochastic errors, i.e. in probabilistic terms. But, such system has non-linear characteristics.

For this reason, Extended Kalman Filter (EKF) is used. Literature demonstrates that EKF has been effectively used to reduce line fitting noise (Ji Zhang, 2013), to detect the row's position (distance/orientation) relative to robot (RIGGIO, 2018; BERGERMAN, 2015), to improve desired path (LEMOS, 2018) among many other applications in agriculture.

2.5 Summary of Hypotheses

Additionally to the research questions presented on Sec. 1.4, the hypotheses guided the development towards the desired perception subsystem. They are:

- Usage of a lightweight ground mobile robot. This leads to a platform that will be majority of time under-canopy and that is greatly impacted by ground unevenness;
- Resemblance of crop lanes as ever-changing and long corridor due to lack of time-invariant landmarks. This discourages mapping techniques;
- Frequent occlusion of the sensor or the stalks because of the hanging leaves. Since it gives us a low expectation of existence of a best line to represent the rows, usage of computationally intensive methods to line detection is not justified;
- Unlike walls in corridor, crop rows show much less level of parallelism due to the plant orientation growth, environment effects and the intrinsic spacing between plants. Therefore, the instantaneous lane direction may be better described by the instantaneous direction of the best line candidate for the rows instead of an average value between both line candidates, which could possibly be a far-off value for both rows.

3 MATERIAL AND METHODS

This chapter discusses the required materials, methods and assessment procedure in the development process of a perception subsystem to obtain lateral distances for compact robots within sub-meter crop rows. First, Sec. 3.1 describe the LiDAR, core sensor used for the perception system, Sec. 3.2 exposes all robotic platforms used to test the perception subsystem, and Sec. 3.3 brings an overall discussion about the experimental sites. ***Perception LiDAR*** (PL) is described in Sec. 3.4, the Extended Kalman Filter implementation in Sec. 3.5 and the performance indicators in Sec. 3.6.

3.1 Core sensor

LiDAR is the core sensor of all perception subsystems described in this document. It provides vectorial information (direction and distance) to surroundings objects. A standard single plane LiDAR such as the USD 5K Hokuyo UTM-30LX covers a 270° angular range with resolution of 0.25°, resulting in 1081 readings. It can sense objects up to 30 m with 40 Hz update rate. The basic principle behind LiDAR's functioning and a static characterization are provided in Appendix A. A combination of reduced cost, similar field performance and higher communication reliability (UTM-30LX uses USB) led to adoption of Hokuyo UST-10LX (USD 1.5K) with equal specifications except reduced range to 10 m and use of Ethernet for data communication.

Two considerations shall be made about positioning the LiDAR sensor on the robot: 1) Field of View and 2) Height. The first takes into account the 270° angular range, which is easily achieved without occlusion from robot's own body by either placing it far ahead of robot (hElvis III, TS2017 in Tab. 2) or by putting as the highest device on the robot (TS2018 and TS2020). By putting it on platform's longitudinal axis, symmetry facilitates further calculations. The height directly affects the plane of reading since the considered LiDAR is a 2D one. The closer the sensor is to the ground, it will be more subject to weeds, and ground unevenness may produce enough rolling that sensor reads the ground. And the higher it is placed, the more influence it will have from leaves. Nonetheless, while a variable height placement would be optimal to always place the sensor at a suitable height that allows sensing the stalks and neglect most of leaves and weeds, the bigger picture indicates that the idea to use LiDAR is to allow GNSS-free navigation when robot is operating under-canopy. Therefore, while robot is not covered, a LiDAR-based navigation is not required and a best fixed height would be one that possibly removes more weeds and ground interference. Furthermore, as the crop grows and due to relatively low height of the robots (around 0.3 m), sensor placement on top of robot will gradually be less affected by hanging leaves.

To overcome costs, investigation about 3D point clouds was conducted with the Multi-Layer Sensing System (MLSS), a sensing package designed and implemented by MSc Mateus Gasparino at LabRoM (GASPARINO, 2020). It uses two actuators in orthogonal axes to add two degrees of freedom (roll and pitch) to a 2D LiDAR Hokuyo UTM30-LX, used to retrieve distance measurements from environment. Figure 15 shows the CAD view, the additional degrees of freedom and how the system is attached to hElvis. Additionally, Fig. 15d shows the location of the InvenSense MPU 9120 IMU devices. IMU 1 provides the orientation angles of the MLSS' moving part. Such information is used to know the angle between reading plane and ground at the moment of the scan. And the IMU 2 acquires the orientation angle of the robot, which varies significantly due to soil unevenness. Because MLSS and the robot shares same orientation angles, information from IMU 2 allows the correct spatial transformation of the scans from LiDAR's position (top of the mast) to the origin considered by the perception subsystem (geometric center of the LiDAR at the robot's front part). Additional information is provided on Gasparino, Higuti, Velasquez and Becker (2020).

Figure 15 – a) CAD view of the Multi-Layer Sensing System (MLSS); b) Pitch movement around gray arrow; c) Roll movement around red arrow; d) Actual system with MLSS and positioning of IMU (Inertial Measurement Units) devices.

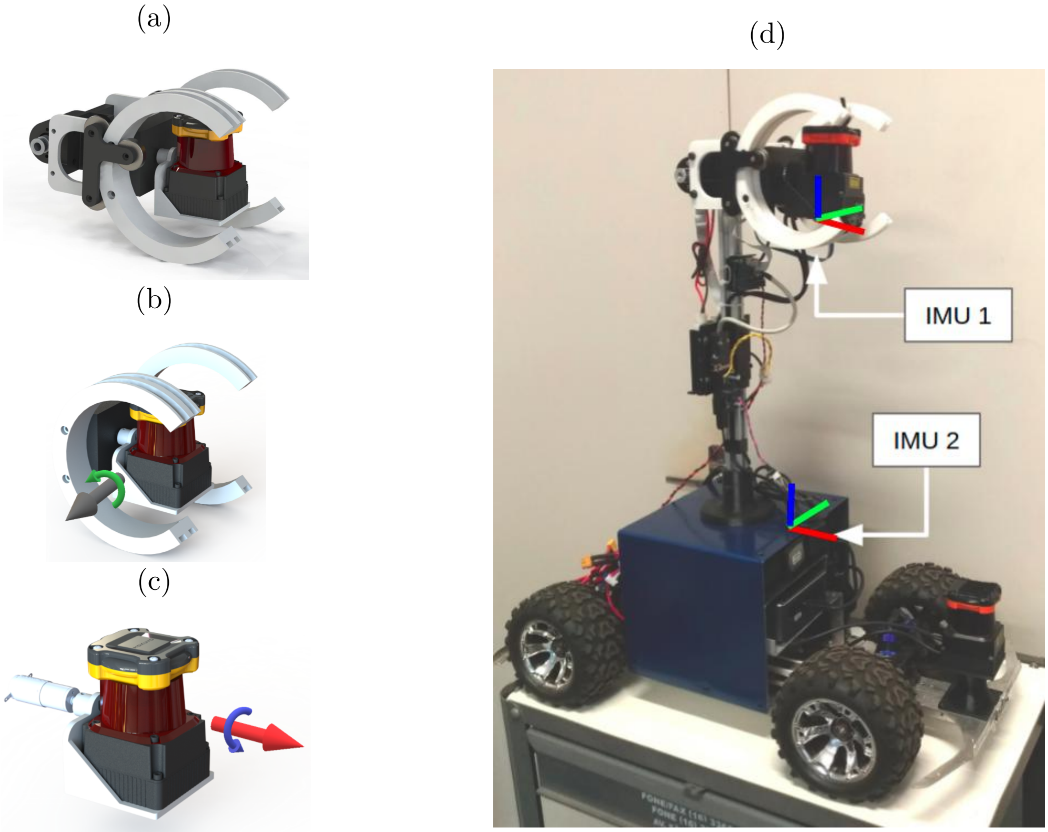

Source: retrieved from Gasparino, Higuti, Velasquez and Becker (2020).

The other sensors such as IMU, motor rotary gauges and GNSS devices will be listed with the used platforms in the next section.

3.2 Robotic Platforms

This study relied on multiple robots to evaluate the autonomous navigation within crop rows. Two general groups may be considered: 1) hElvis, the LabRoM's small car-like prototype; and 2) TerraSentia, a skid-steer robot provided by EarthSense and object of study for the joint research between DASLAB (UIUC) and LabRoM. This section will list the physical characteristics and relevant embedded devices on each used robot. All robots and a summary of their components are presented by Table 2.

3.2.1 hElvis

The hElvis platform has been a research platform since 2010 and suffered several hardware changes to accommodate new requirements. For higher control reliability, the original combustion locomotion module was replaced by a electric one and it is composed by two subsystems: 1) Propulsion with an EPOS2 50/5 controller, an automotive-like differential mechanism, an EC-4Pole Maxon motor suitably coupled to an incremental encoder and 23:1 gearhead; and 2) Steering with EPOS2 24/5 controller, Ackermann mechanism, a power-screw system and a REmax29 DC Maxon motor also coupled to an incremental encoder and 33:1 gearhead. A limitation of such platform is its low ground clearance of about 35 mm, which makes ground unevenness highly relevant to navigation performance.

The first version used for agricultural research is hElvis III. It used a Raspberry Pi 2 running Raspbian Wheezy as main control unit and code was a standard C++ project. An UTM-30LX LiDAR sensor was placed in the center of the robot's front part and an Sparkfun MPU9150 IMU roughly around robot's center of mass. To investigate the usage of 3-D LiDAR information, hElvis III has been upgraded to hElvis IV (Fig. 15d). Besides changing the control unit to an Intel HTPC NUC, with Intel I7 processor, 16GB of RAM and 1TB of solid state drive, the Multi-Layer Sensing System (MLSS), an additional mechanism to stabilize and rotate a 2D LiDAR, was added.

3.2.2 TerraSentia

EarthSense, an UIUC spin-off, has been deploying TerraSentia robots since 2017. The robot is conceived to automate the measurement of plant traits for efficient phenotyping. Its locomotion is a skid drive where two commands are sent to the motors: One for left wheels and another for right wheels. It is approximately the same size as hElvis but it has the advantage of a greater ground clearance and bigger wheels. For this study, three versions have been used.

First, TS2017 had most of the mechanical parts, including wheels, built through additive manufacturing with polylactic acid. This led to an ultralight 6.6 kg robot. It used brushed 12 V DC motors with 131.24:1 Pololu metal gearbox and two-channel Hall-effect

Pololu encoders. The robot had the Hokuyo UTM-30LX in the front part and a Septentrio Altus APS-NR2 RTK-GNSS receiver on its top. TS2018 is a following version with higher torque and speed 118 rpm HD Premium Planetary Gear Motor (reference number: 638324).

Finally, TS2020 has a hard plastic enclosure reinforced by a lightweight metal frame. The brushed motors have been replaced by Maytech Brushless Outrunner Hub Motor with hall-effect sensor. To measure distances, it uses a Hokuyo UST-10LX placed in the front part of the robot. Additionally, TS2020 contains a Bosch BNO0555 IMU on its turning axis and an Ublox Zed-F9P GNSS receiver.

Table 2 – LabRoM robotic platforms (alphabetic order). ⋆ Height of LiDAR's plane of view. ⋆⋆ Average field autonomy for the specified power supply. For the same robot, it is highly affected by the ground unevenness and whether ground is dry or wet.

Characteristics / Robots	hElvis III	hElvis IV	TS2017	TS2018	TS2020
Picture	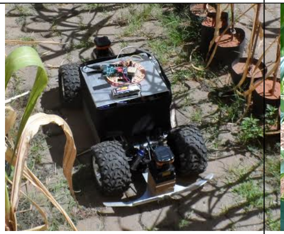				
Width	0.45 m	0.45 m	0.31 m	0.31 m	0.32 m
Length	0.65 m	0.65 m	0.51 m	0.51 m	0.54 m
Height	0.23 m	0.8 m	0.33 m	0.39 m	0.40 m
⋆ LiDAR's height	0.17 m	0.17 m	0.20 m	0.37 m	0.36 m
Locomotion type	Frontal Ackermann	Frontal Ackermann	Skid-steer	Skid-steer	Skid-steer
Power Supply	2x 14.8V LiPO	2x 14.8V LiPO	14.8V LiPO	14.8V LiPO	14.8V LiPO
Main Control Unit	Raspberry Pi 2	Intel I7 NUC	Raspberry Pi 3B	Raspberry Pi 3B	Raspberry Pi 3B + Intel I7 NUC
Embedded LiDAR	1x UTM-30LX	1x UTM-30LX (MLSS system)	1x UTM-30LX	1x UTM-30LX	2x UST-10LX
Embedded IMU	Sparkfun MPU9150	InvenSense MPU9150	Not used	SparkFun 9DoF Razor M0	Bosch BNO055
OS + software implementation	Raspbian Wheezy + standard C++ project	Ubuntu 14.04 + ROS Indigo	Proprietary	Proprietary	Proprietary/ROS Melodic
⋆⋆ Expected field autonomy [hours]	4	2	2	4	1

Source: author's own elaboration.

3.3 Experimental sites

3.3.1 Mock-up setup

Although most of algorithm development may be achieved with field data collected with a manually controlled robot, implementation often faces unexpected interactions between software and hardware. Moreover, field place is often unsuited for major changes since crops, at some point, become too distant from facilities to be have covered desks and access to power outlets for both development laptops and mobile robots. To tackle such logistic issue and mitigate troubleshooting on field testing, fake setups have been used.

The first is composed by 0.5 m PVC tubes vertically placed on wood holders (Fig. 16a). Such modularity allows custom arrangements to evaluate field characteristics such as missing plants, missing row segments, begin/end of lane and curves. And the second uses fake corn instead of PVC tubes (Fig. 16b). A third one is composed of corn planted on pods (Fig. 16c).

Figure 16 – Mock-up experimental sites (a) PVC tubes (b) Off-the-shelf fake corn (c) Corn planted on pods.

(a) (b) (c)

Source: author’s own collection.

3.3.2 Field testing

Several corn and sorghum fields located on São Carlos, SP or across USA (Urbana-Champaign, IL; Columbia, MO) from 2016 to 2020. The common trait is that they are arranged in rows with usual row spacing below one meter. Specific details for each field will be pointed before respective result analysis and discussion. For the under canopy operation, the core sensor (LiDAR) is hardly subject to direct sunlight, thus tests were not restrained to a specific hour of day but happened throughout day (6 a.m. to 6 p.m.). The direct sunlight condition usually happened when leaving the crop, thus the task of navigating through lane is completed.

3.4 *Perception LiDAR* (*PL*)

This section details $\boldsymbol{PL}$, the core perception subsystem used to provide surroundings knowledge to the robotic platforms. As the goal is an extensively field-tested system, constraints have been made to bound the problem of detection of crop rows with LiDAR measurements and subsequently reduce computational requirements.

User-defined constraints

The Region of Interest (ROI) limits the readings that will be further used by the algorithm. Field experience has shown that sub-meter lanes usually have valuable information in the next two meters ($l = 2$). This value could be lower for more cluttered lanes as leaves/weeds would block the view and farther readings would be too sparse. It could be greater for sparse and clean fields. While $l = 2$ has been a reasonable value for most sub-meter lane fields, it is a parameter that can be tuned with respect to each field by observing the general distribution of LiDAR readings.

In one of $\boldsymbol{PL}$ steps, a histogram is used to find the peaks in the LiDAR readings that correspond to the rows. A suitable bin size is key to not have counts of the row across multiple bins. Therefore, bin size should be greater than stalk width. Additionally, a safe margin should be considered to account for expected alignment variation between stalks in the same row.

When $\boldsymbol{PL}$ runs only with LiDAR inputs, it misses comparison with other sensors. As such, another two user-defined parameters *zero_rotation_heading_lim* and *zero_rotation_diff_lane_width* are set to trigger a comparative execution of $\boldsymbol{PL}$ with null pre-rotation of LiDAR readings as relative orientation of robot with respect to lane may be misleading. The first parameter refers to expectation of robot not being greatly rotated with regards to lane, e.g. with an orientation error greater than 30°. And the second refers to the expectation of lane width being within a small variation of few centimeters for consecutive executions. All user-defined constraints are summarized in Table 3.

Geometric and Temporal constraints

Row spacing, i.e. distance between rows when planting, is known. It is also expected that rows are roughly parallel in such region, not having more than $\epsilon = 5°$ difference. Coupled with the ROI, these two assumptions lead to a trigonometric relationship that curvature of the lane should be above $0.5l/\cos(90° - \epsilon) \approx 11.47$ m. Robot's width also plays an important role since LiDAR readings within robot's envelope are straying leaves and other objects, therefore not useful for perception.

Robot's speed is not greater than 1 m/s and since line detection is based on LiDAR readings, it has approximately the same frequency as the sensor (40 Hz). Therefore, only few centimeters displacement is expected between consecutive executions. This narrows

Table 3 – User-defined Constraints

Symbol	Name	Description
r_{x0}, r_{x1}, r_y	ROI limits	ROI limits with respect to {L} reference frame
$BINS\_SIZE$	Histogram's bin size	Desired size of the histogram bins by user. It should be greater than stalk's width and accommodate for expected alignment variation between stalks
$zero\_rotation$ $heading\_lim$	Heading Limit	Threshold value of heading that triggers a comparative execution of ***PL*** with null pre-rotation value for LiDAR
$zero\_rotation$ $diff\_lane\_width$	Lane Width Difference Limit	Threshold for maximal difference of consecutive lane width estimations that triggers a comparative execution of ***PL*** with null pre-rotation value for LiDAR

down each side ROI to a nearby threshold along previous estimates. Similarly to linear movement, angular rate change is physically bounded. As such, the angle of estimated lines cannot vary above a threshold. Geometric and Temporal constraints are summarized in Table 4.

Table 4 – Geometric and Temporal Constraint Parameters

Symbol	Name	Description	Type
RS	Row Spacing	Nominal value for distance between rows when planting	Geometric Constraint
RW	Robot Width	Width of robot	Geometric Constraint
max_diff_bin	Maximal change of bins	Bin with most readings must be at most max_diff_bin units far from bin with most readings from last loop	Temporal Constraint
max_diff_alpha	Maximal change of row angle	Threshold of maximal difference between row angle for current and previous estimates for side $\mathcal{S}$	Temporal Constraint

Overview

PL is represented by ***Estimate*** and ***Validate*** phases in Fig. 17, which shows the general architecture of the code embedded in the robots. There are two important sets of information that are adjusted every execution and that are used in the next loop: *Perception Outputs* and *Analytics Outputs*. The first is composed by the robot's orientation error with respect to lane's direction and the lateral distances. The former contains the previous values for lateral distance, heading, individual row angles, *Histogram Index* and

Table 5 – Reference Frames and Coordinate Systems

Symbol	Name	Description	Type
x	x-axis	Either lane or robot's longitudinal axis	Coordinate axis
y	y-axis	Either lane or robot's traversal axis	Coordinate axis
{R}	Robot Frame	Robot's reference frame	Reference Frame
{L}	Lane Frame	Lane's reference frame	Reference Frame
{G}	Global Frame	World's reference frame	Reference Frame
$\mathcal{S}$	Side	Either left (L) or right (R) side	Generalization
$x_i, y_i,$ r_i, λ_i	LiDAR Readings	A LiDAR reading happens on polar coordinates with radial r_i and angular λ_i. It is converted to cartesian coordinates x_i and y_i	Coordinate System

Table 6 – Internal Variables

Symbol	Name	Description
$m^{\mathcal{S}}$, $b^{\mathcal{S}}$	Line Parameters	Slope and intercept for the line of side $\mathcal{S}$
$\alpha^{\mathcal{S}}$	Row angle	Angle offset between side line and lane's heading
$l^{\mathcal{S}}$	Line Length	Length of the found line for side $\mathcal{S}$
$np^{\mathcal{S}}$	Number of Points	Number of points used to obtain line for side $\mathcal{S}$
$sd^{\mathcal{S}}$	Standard Deviation	Standard deviation of the line for side $\mathcal{S}$
$\Delta d^{\mathcal{S}}$	Distance Estimate Difference	Difference between current and previous distance estimates for side $\mathcal{S}$
β	Angle Increment	Based on heuristics, only one side's row angle is used to update lane heading. Such row angle is further called β

LineScore. For reader's easiness, the symbols used in ***PL*** for Reference Frames/Coordinate Systems, Internal Variables and Output Values are respectively summarized in Tables 5, 6 and 7.

The ***Initialize*** stage imports configuration files with robot's physical characteristics (robot's and wheels' dimensions), threshold values and user-defined values. A current limitation of ***PL*** is the requirement to inform the row spacing nominal value. ***Update*** shows that **ENVIRONMENT** is constantly measured with the onboard sensors to provide updated values for every execution loop. This ***Update*** step has been synced with LiDAR's scan rate. Therefore, whenever a new scan was available, all the other sensors' were updated and used in the calculations. The loop also contains ***Estimate***, ***Validate***

Table 7 – Perception Output Values

Symbol	Name	Description
$d^{\mathcal{S}}$	Lateral Distance	Orthogonal lateral distance from robot to line specified by $\mathcal{S}$
ϕ	Heading Error	Relative orientation/heading error between robot and lane x-axes
LW	Lane Width	Current distance between left and right row estimates
CTE	Cross Track Error	Error between robot and its expected position
$valid^{\mathcal{S}}$	Estimate Validity	States whether estimated line for side $\mathcal{S}$ is valid or not
$LineScore^{\mathcal{S}}$	Estimate Score	Gives a score for the line estimation for side $\mathcal{S}$

Figure 17 – Diagram of robot's embedded code. ***Initialize*** step encompasses the loading of configuration files, starting devices and setting initial values. ***Update*** retrieves the most recent sensor readings. ***PL*** core concepts are represented by ***Estimate*** and ***Validate*** stages. The first obtains the estimated lateral distances and relative heading between robot and lane by processing LiDAR input. Then, ***Validate*** checks the former's output to assess their validity. If valid, the perception outputs can be used by ***Control*** to calculate driving commands.

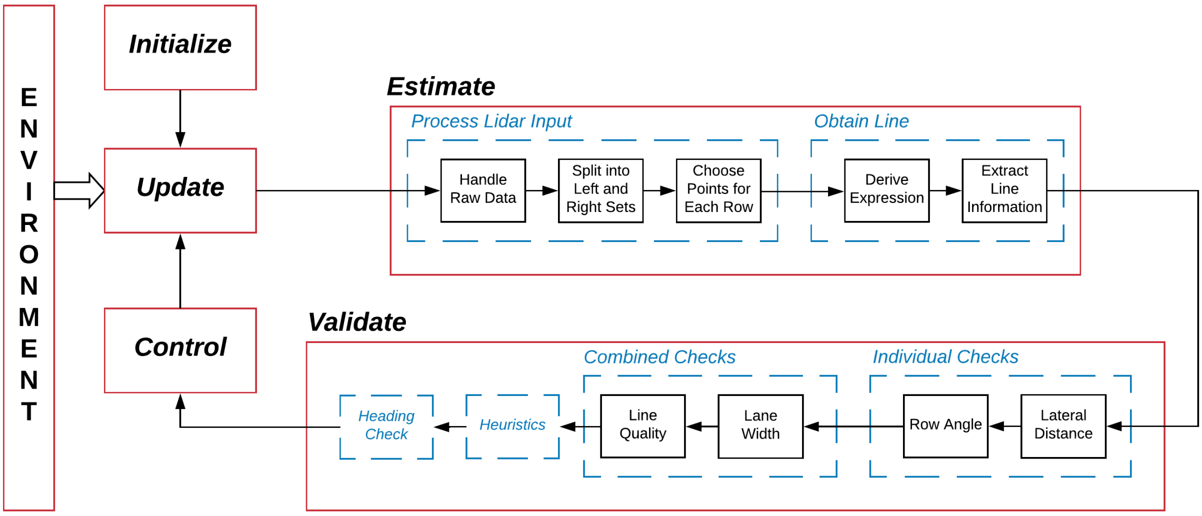

Source: retrieved from Higuti, Velasquez, Magalhaes, Becker and Chowdhary (2018).

and ***Control***. In the first, lateral distances and orientation error are estimated. The second assess the outputs following a heuristics and the latter generates a suitable control action for the locomotion module. Each block will be further described in the following sections. First, the frame coordinates and outputs will be explained.

3.4.1 Frame coordinates and *Perception Outputs*

Figure 18 shows a top view of the usual work environment for the robot TerraSentia 2020, i.e. between crop rows. The LiDAR sensor is in the front part of the robot (see red circle) and it provides scans on a reading plane parallel to ground. The raw LiDAR measurements are 1081-element vectors in polar representation. Each element is a distance measurement associated to a fixed reading angle. A transformation from polar to Cartesian coordinates is performed in the robot frame ({R} in Fig. 18). It is a local coordinate frame firmly attached to the sensor origin, and x-axis is coincident with robot's longitudinal axis and y-axis positive part is to the left of the robot. The lane coordinate frame ({L}) is another local coordinate frame whose origin is also attached to sensor's origin. But instead of rotating with robot as it moves, {L} has the x-axis always aligned with the lane's direction. Finally, the global coordinate frame ({G}) is arbitrarily fixed at some point in the 2D space, for example just outside the field.

Figure 18 – A top view of TS2020 within corn rows. Global G, Lane L and Robot R reference frames. The origins of L and R are attached to LiDAR's geometric center. While x^R is always aligned with robot's longitudinal axis, x^L is parallel to lane direction. ϕ is the angle between these two x-axes. The orthogonal distances between sensor and each lateral row is represented by d^R and d^L. In real world, rows are not perfectly aligned. Therefore, lane direction follows the direction of the side that is best fitted to row, e.g. longest visible row or less dispersed points.

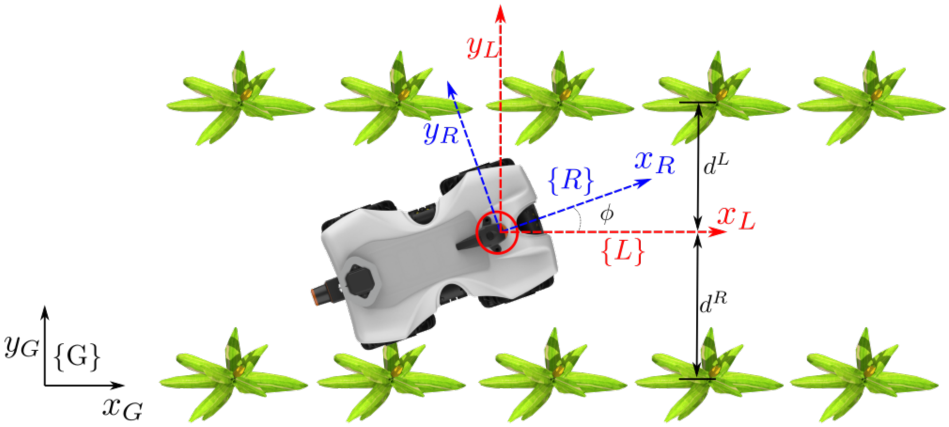

Source: author's own elaboration.

The lateral distances d^L and d^R are the orthogonal distance between LiDAR's center and left or right rows, respectively. The lines to represent each row on side $\mathcal{S}$, where $\mathcal{S} = L$ for left and $\mathcal{S} = R$ for right, are defined by their slope $m^{\mathcal{S}}$ and intercept $b^{\mathcal{S}}$ in the {L} coordinate frame. Therefore, lateral distance for the side $\mathcal{S}$ is given by the orthogonal distance between {L}'s origin $(x_0^{\{L\}}, y_0^{\{L\}})$ and the respective line parameters $(m^{\mathcal{S}}$ and $b^{\mathcal{S}})$

as given by Eq. 3.1. Angle ϕ is the estimate of relative orientation/heading error between robot and lane x-axes.

$$d^{\mathcal{S}} = (k^{\mathcal{S}} + b^{\mathcal{S}} x_0^{\{\mathrm{L}\}} - y_0^{\{\mathrm{L}\}})/\sqrt{(b^{\mathcal{S}})^2 + 1} \tag{3.1}$$

Since coordinate frame {L} is aligned with the lane and lateral distances are calculated as orthogonal distances from origin to respective line representations in this coordinate frame, the lateral distances lie on a segment on x-axis that orthogonally crosses the lane at that given time of calculation. Then, their combination lead to two quantities: Lane Width (LW) and Cross Track Error (CTE). The first, expressed by Eq. 3.2, indicates the current distance between estimated rows, therefore the navigable space for the robot. Because it is expected to be the same as Row Spacing (RS), the nominal value used to plant the seeds, it is used for validation purposes (Sec. 3.4.3) and also to evaluate performance (Sec. 3.6.1). The second, given by Eq. 3.3, is the error between robot and its expected position. Robot's current position is represented by sensor's position, thus in coordinate frame {L}, that is origin $x_0^{\{\mathrm{L}\}} = 0$. And expected position $x_m^{\{\mathrm{L}\}}$ is center of the lane, therefore a midpoint between left ($x_L^{\{\mathrm{L}\}} = -d^L$) and right ($x_R^{\{\mathrm{L}\}} = d^R$) lines. It is used as input to ***Control*** block.

$$LW = d^R + d^L \tag{3.2}$$

$$CTE = x_0^{\{\mathrm{L}\}} - x_m^{\{\mathrm{L}\}} \Rightarrow CTE = 0 - 0.5(x_L^{\{\mathrm{L}\}} + x_R^{\{\mathrm{L}\}}) \Rightarrow CTE = 0.5(d^L - d^R) \tag{3.3}$$

3.4.2 ***Estimate*** block

Estimate stage is fed with raw LiDAR data. First, it processes the input to filter and separate data into two suitable sets, one for left and another for right side (Sec. 3.4.2.1). Then, the lines that represent each side are extracted, if possible (Sec. 3.4.2.2).

3.4.2.1 Process LiDAR Input

The raw LiDAR readings have the polar format, being described by the range (measured distance) r and the associated angle of reading $\lambda \in [-0.75\pi, 0.75\pi]$. First, the readings are converted to Cartesian coordinates ({R} in Fig. 18) using Eq. 3.4 where ϕ_{k-1} is the previous estimate of heading. ϕ_{k-1} is used to suitably rotate readings to obtain rows as parallel as possible to x_R.

$$\begin{cases} x_i = & r_i cos(\lambda_i + \phi_{k-1}) \\ y_i = & r_i sin(\lambda_i + \phi_{k-1}) \end{cases} \tag{3.4}$$

Figure 19 – A top view of TS2020 within corn rows. The black full are the lines that represent the rows. lines A black dashed rectangle readings delimits a section of data that will be further used. It is defined by r_{x0}, r_{x1} and r_y where the first two balances the importance between readings behind with those ahead the sensor. The latter parameter is chosen to avoid readings from rows besides the immediate adjacent ones. Subsequently, a ROI is defined for each side and it is represented by the red dotted rectangles. *RS* is the row spacing, nominal value used for planting.

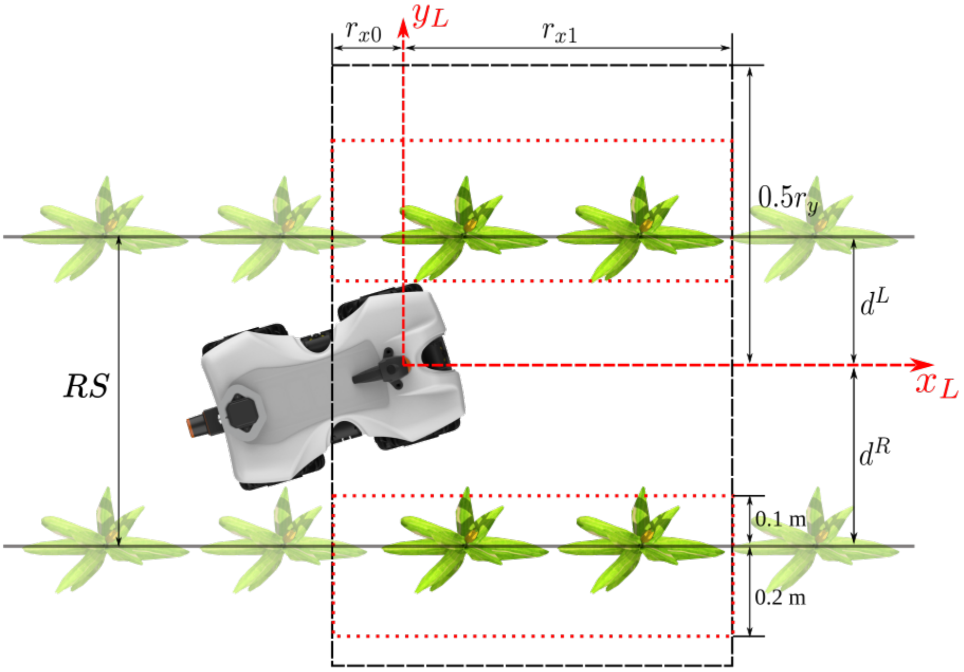

Source: author's own elaboration.

Since robot is within a lane with *RS* that does not exceed 1 m, using all LiDAR mesurements is not effective as it only raises complexity and computational costs. Figure 19 shows the reduction procedure. First, the raw LiDAR input is limited to the region within black dashed rectangle and the output is called *FilteredPoints*. Because it is expected that both sides are equally useful to estimate the row distances, r_y has a midpoint in $x = 0$. On the other hand, r_{x1} and r_{x2} are chosen to balance the influence of readings ahead and behind sensor.

The ROI, pictured by the red rectangle in Fig. 19, is defined for each side. Thus, *FilteredPoints* is further filtered into two *SidePoints* sets (one for each lateral row). The limits in $y - axis$ are suitably updated in the ***Validate*** stage to adjust to last valid estimates of lateral distances.

The next step is to choose the points from each *SidePoints* that most likely reflect the row, i.e. pertain to stalks. This is achieved applying a histogram-based algorithm (**ChooseBasedOnHistogram** in Alg. 1).

Algorithm 1 Pseudocode for choosing readings based on Histogram. Source: extracted from Higuti, Velasquez, Magalhaes, Becker and Chowdhary (2018).

```
ChooseBasedOnHistogram():
    Histogram Bins = fcnHistogram(SidePoints, Histogram Intervals);
    Histogram Index = indexMaxDouble(Histogram Bins);
    validateHistogramIndex(Histogram Index, Previous Histogram Index);
    ChosenPoints = chooseReadingsToBeFitted(Histogram index, Histogram Bins, SidePoints)
```

For each *SidePoints* set, their y-values are sorted by **fncHistogram** into bins whose bin edges are given by *Histogram Intervals*. The bin size is defined by user as $BINS\_SIZE$. It should be greater than stalk's width and accommodate for expected alignment variation between stalks. Then, **indexMaxDouble** finds *Histogram Index*, the index of the bin containing more elements. If it is deemed valid by **validateHistogramIndex**, such value will be used as reference to select the readings for line fitting. The validation process checks if the *Histogram Index* is not an extremity of *Histogram Intervals* and also checks if its current value did not change more than *max_diff_bin*. The first is required because readings from neighboring bins will also be used. And the second avoids great discontinuities. If *Histogram Index* is invalid, previous value replaces it.

Lastly, **chooseReadingsToBeFitted** stores the selected readings in *ChosenPoints*. *Histogram Index* indicates the bin and half bin to each side whose readings should be used. The additional half bin accounts for possible row information that may be spread over more than one bin because the pre-rotation tries to adjust only one side to be parallel to x-axis, and the other may have considerable inclination.

3.4.2.2 Obtain Line

The next step is to use least squares linear regression on *ChosenPoints* to fit a first-order line given by $y = mx + b$. Equations 3.5 and 3.6 gives the slope m and intercept b, respectively.

$$m = \frac{n\sum_{i=1}^{n} x_i y_i - \sum_{i=1}^{n} x_i \sum_{i=1}^{n} y_i}{n\sum_{i=1}^{n} x_i^2 - (\sum_{i=1}^{n} x_i)^2} \tag{3.5}$$

$$b = \frac{\sum_{i=1}^{n} y_i \sum_{i=1}^{n} x_i^2 - \sum_{i=1}^{n} x_i \sum_{i=1}^{n} x_i y_i}{n\sum_{i=1}^{n} x_i^2 - (\sum_{i=1}^{n} x_i)^2} \tag{3.6}$$

If m for a given side is a finite number (it is not if *ChosenPoints* set is empty), a line may be fitted. From it, six characteristics can be extracted: Lateral distance d^S, row angle α^S, length l^S, number of points np^S, standard deviation sd^S and difference between current and previous estimated lateral distance Δd^S. Equation 3.7 defines lateral distance where $\mathcal{S}$ is L for left or R for right side. Equation 3.8 gives row angle, which represents the inclination between the fitted line and robot's longitudinal axis, i.e. x_L axis. Length is the difference between the lowest and highest x-values within set. np^S indicates the number of points used for line fitting for side S. And the last characteristic is given by Eq. 3.9.

$$d_k^S = \left\| \frac{b}{m} \sin(\arctan(m)) \right\| \tag{3.7}$$

$$\alpha_k^S = \arctan(m) \tag{3.8}$$

$$\Delta d^S = \left| d_k^S - d_{k-1}^S \right| \tag{3.9}$$

3.4.3 ***Validate*** block

The frequent occlusion by leaves causes sudden changes in the LiDAR readings, which affects the estimates and they no longer reflects reality. To mitigate this, certain variables are assessed in both ***Estimate*** and ***Validate*** stages. The first handles the individual validity checks while the latter evaluates as a whole. After all validation trials, two booleans $valid^S$ state whether respective side is valid or not, and two $LineScore^S$ hold a quantitative value for estimation quality. ***Estimate*** stage performs two checks:

1. Lateral distance d_k^S is valid if $d_k^S \in (0.5RW, 1.1(RS - 0.5RW))$;
2. Row angle α_k^S is valid if $\left|\alpha_k^S - \alpha_{k-1}^S\right| < max\_diff\_alpha$.

Validate stage continues with three steps:

1. Calculation of current LW_k. If $LW_k \in (1.1RW, 1.2LW)$, LW_k is considered valid. Otherwise, the side with greatest Δd^S is considered as invalid;
2. Calculation of line score $LineScore^S$. Equation 3.10 exemplifies the score for left side. It is a comparison between left and right lines with respect to four aspects: np^S, l^S, sd^S and Δd^S, all calculated in *Obtain Line* stage:
    a A greater np^S indicates more points were used to fit the line, therefore it should be a better representation;
    b A greater l^S indicates that a given side is longer (may be used for more time);
    c A lower sd^S may indicate less presence of outliers such as leaves/weeds not in the same line as the stalks;
    d A lower Δd^S is fundamental to track estimation continuity.
3. Heuristics (Sec. 3.4.3.1).

$$LineScore^L = \frac{np^L}{np^L + np^R} + \frac{ly^L}{ly^L + ly^R} + \left(1 - \frac{sd^L}{sd^L + sd^R}\right) + \left(1 - \frac{\Delta d^L}{\Delta d^L + \Delta d^R}\right) \tag{3.10}$$

Additionally, $LineScore^S$ of the side that was last used as reference receives a 0.1 bonus. This prevents bouncing from better left to better right on consecutive loop executions when the scores are similar.

3.4.3.1 Heuristics

The ***Heuristics*** stage considers the validity status valid^S and score LineScore^S for each line to decide how to update *Perception Outputs* and *Analytics Outputs*. Therefore, there are four cases:

1. Both lines are valid;
2. Only left line is valid and its score is greater than right side;
3. Only right line is valid and its score is greater than left side;
4. None of above.

Depending on the case, heading ϕ_k and lateral distances d_k^L, d_k^R for the step k will be updated diferently. Each case defines an angle increment β such that it updates ϕ_k given Eq. 3.11.

$$\phi_k = \phi_{k-1} + \beta \tag{3.11}$$

In the first situation, β is the row angle α of the line with higher *LineScore*. Only one side, instead of an weighted average of both row angles, is used because real world crops does not present parallelism and therefore an average value would not benefit the detection of any. Using the best score to decide which side to use as reference facilitates that the same side continues being detected.

In both second and thirds cases, β is the row angle α of the respective side. Because only one line is valid, the other side needs to be replaced. For illustration, consider case 2 in Eq. 3.12.

$$d_k^R = \begin{cases} d_{k-1}^R - (d_k^L - d_{k-1}^L) & \text{if} \left|d_k^R - d_{k-1}^R\right| > 0.2LW \\ RS - d_k^L & \text{otherwise} \end{cases} \tag{3.12}$$

Therefore, the invalid d_k^R will be replaced by either a combination of past value and the incremental difference of the valid side or a combination of the nominal value with the valid side. An analogous procedure happens for case 3.

In all three cases above, *Analytics Outputs* are updated with the current variable values. The ROI limits are updated to have one for $y \in (-d_k^L - 0.2, -d_k^L + 0.1)$ and another for $y \in (d_k^R - 0.1, d_k^R + 0.2)$. The regions are not centered on lateral distance estimates to account for unwanted hanging leaves that pull estimation inwards. Finally, on last case, there is no guarantee about the quality of the lines. Because of that, all *Perception Outputs*, *Analytics Outputs* and ROI limits remain unchanged.

3.4.3.2 Final check

The heading ϕ is an accumulator of successive heading difference given by the best row current angle with respect to lane x-axis (x_L). As a safety measure, the method evaluates two conditions every loop: 1) $\phi > zero\_rotation\_heading\_lim$; 2) Difference between current and previous estimated LW is greater than $zero\_rotation\_diff\_lane\_width$. A positive confirmation for any of the cases indicate loss of reliability and all ***Estimate*** calculations are repeated without pre-rotating LiDAR readings with ϕ. If the obtained *LineScore* for the reference side is greater than its normal execution value, therefore a unrotated LiDAR led to higher estimate grades, the loop continues with the values calculated for $\phi = 0$.

3.4.4 Control stage

The ***Control*** step is dependent on which robot is used. In general, this block expects the CTE as input and outputs a desired turn rate. In hElvis III and hElvis IV, this block is either a H∞ controller using the frontal Ackermann geometry reduced to the bicycle model or a PID controller (VELASQUEZ, 2019). For TS2017 and TS2018, it is a PID controller (HIGUTI, 2018). Finally, TS2020 uses a potential field to account for both CTE and heading error.

3.5 Extended Kalman Filter for lateral distance estimation

The robot's mass center forward linear speed in x-axis v_x and angular speed around z-axis ω_z in local coordinates are provided by the onboard odometry and gyroscope, respectively. Using these measurements, robot's mass center pose (x^C, y^C, ϕ^C) from instant $k-1$ to k for elapsed time dt can be calculated with Eq. 3.13:

$$\begin{bmatrix} x_k^C \\ y_k^C \\ \phi_k^C \end{bmatrix} = \begin{bmatrix} x_{k-1}^C \\ y_{k-1}^C \\ \phi_{k-1}^C \end{bmatrix} + \begin{bmatrix} \cos(\phi_k^C)dt & 0 \\ \sin(\phi_k^C)dt & 0 \\ 0 & dt \end{bmatrix} \begin{bmatrix} v_x \\ \omega_z \end{bmatrix} \tag{3.13}$$

Figure 20 – Schematics to show relationship between sensor and mass center positions. The green dashed line represents the left row.

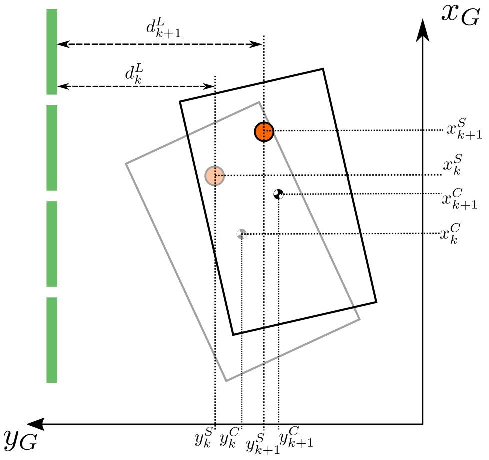

Source: author's own elaboration.

Figure 20 shows that mass center position(x^C, y^C) can be related to the sensor's position (x^S, y^S) with Eq. 3.14:

$$y^S_k = y^C_k + L_{offset} \sin \phi^C_k \tag{3.14}$$

where L_{offset} is the longitudinal distance between mass center and sensor's center. Subsequently, the relationship between lateral distance and sensor is given by Eq. 3.15:

$$\Delta d^L = -\Delta y^S \Rightarrow \Delta d^L = -\Delta y^C - L_{offset}(\sin \phi^C_{k+1} - \sin \phi^C_k) \tag{3.15}$$

Equation 3.15 may be rewritten as Eq. 3.16:

$$\Delta d^L = -\Delta y^C - L_{offset} 2 \sin \left(\frac{\phi^C_{k+1} - \phi^C_k}{2} \right) \cos \left(\frac{\phi^C_{k+1} + \phi^C_k}{2} \right) \tag{3.16}$$

where $L_{offset} \approx 0.1\ m$. For an average time step $dt = 0.04\ s$, angular speed is less than $1\ rads^{-1}$, which leads to $\Delta\phi^C = \phi^C_{k+1} - \phi^C_k \Rightarrow \Delta\phi^C = \omega_z dt \Rightarrow \Delta\phi^C < 0.04$ and second term of Eq. 3.16 right side is less than a millimeter. Such value is already within sensor's measurement error and carries the uncertainty of heading estimation/time integration. For such reasons and to simplify further calculations, it can be assumed that $\Delta d^L \approx -\Delta y^C$. From Eq. 3.13, Eq. 3.17 is derived:

$$\Delta d^L \approx -\Delta y^C \Rightarrow d^L_{k+1} - d^L_k = -v_x \sin \phi^C_k \Rightarrow d^L_{k+1} = d^L_k - v_x \sin \phi^C_k \tag{3.17}$$

Analogously, Eq. 3.18 expresses right lateral distance difference:

$$d^R_{k+1} = d^R_k + v_x \sin \phi^C_k \tag{3.18}$$

Consider the vector state $X = \left(d^L \; d^R \; \phi \; \dot{\phi} \right)^T$ where d^L is the distance to left row, d^R is the distance to right row and ϕ is the robot's heading. The process can be modelled with Eq. 3.19 where actual state x_k is a function $f(\cdot)$ of past state x_{k-1} and control inputs u_k, and $h(\cdot)$ relates the state x_k to the measurement z_k. The process ω_k and measurement ν_k noises are both assumed to be zero mean Gaussian noises with covariance $\mathbf{Q_k}$ and $\mathbf{R_k}$, respectively.

$$\begin{aligned} x_{k+1} &= f(x_k, u_{k+1}) + \omega_{k+1} \\ z_{k+1} &= h(x_{k+1}) + \nu_{k+1} \end{aligned} \tag{3.19}$$

In the predict step, $f(\cdot)$ (Eq. 3.20) estimates the state using the linear velocity v_x and angular velocity $\dot{\phi}$, respectively from odometry and IMU. Subsequently, in the update step, the innovation occurs by taking into account the calculated values of lateral distances and robot's heading that are obtained from the LiDAR point-cloud (either raw 2D or processed 3-D).

$$f(x_k, u_{k+1}) : \begin{bmatrix} d^L_{k+1} & = & d^L_k - v_x dt \sin \phi_k \\ d^R_{k+1} & = & d^R_k + v_x dt \sin \phi_k \\ \phi_{k+1} & = & \phi_k + \omega_z dt \\ \dot{\phi}_{k+1} & = & \omega_z \end{bmatrix} \tag{3.20}$$

The described EKF for lateral distance estimation becomes an additional stage between ***Validate*** and ***Control*** blocks in Fig. 17. Therefore, its estimations feed the ***Control*** block to calculate the CTE and generate the suitable control action. Additionally, EKF estimates update the distance and heading estimates in *Perception Outputs* to be used in the subsequent execution loop. Because such EKF is an addition to previous ***PL***, its use will be further referred as ***PL+EKF***.

3.6 Performance indicators

The ultimate value given by an autonomous system to the user is freedom to do something else. In this current stage, it means that the operator can just follow the robot through the crop lanes. Instead of giving full attention to drive the robot, the operator can focus on another tasks such as visual inspection and annotation. A glimpse of what happened on field is given by the interventions - moments that operator had to switch from autonomous to manual driving mode. Table 1 shows the five most common intervention types while in autonomous mode.

First, an *End of Lane* intervention indicates that the robot has successfully traversed the lane from the starting point until the end. Sometimes, robot stops midway either because of an operator request or safety emergency stop. This describes the *Middle of*

Lane Stop. These two types can be integrated as a key performance indicator of successful conclusion of crop segment, whether it is a lane from begin to end or a small section of interest, defined by user. The unsuccessful trials finish with a collision to one of side rows (*Left Hit* or *Right Hit*). The last intervention depends on the field arrangement and it refers to the *Gap* situations, where at least 0.5 m no-plant space exists on both sides. This often makes robot to lose track of its current lane.

While all interventions are relevant, this document focuses on those caused by or that are within the scope of the proposed ***PL***. Other interventions' causes include robot's hardware and instabilities of the locomotion controller.

3.6.1 Method to evaluate Perception Subsystem performance

3.6.1.1 Ground Truth

Besides difficulties for the Perception Subsystem itself, assessing it is another major complication. Indoor and most urban outdoor can be translated into maps with landmarks e.g. walls, corners, objects and buildings. In the case of agricultural fields, the best chance would be getting virtual walls from the stems. Although plants are mostly fixed where they were seeded, virtual walls extracted from the field highly depends on visible stalks, which have different width, upward direction of growth and occlusion from leaves. Insertion of artificial landmarks have many disadvantages due to number of different fields used, extensive lengths and manual labor to place and remove them. Moreover, in such under-canopy environment, RTK-GNSS suffers from signal degradation due to loss of satellite view and multi-path. Therefore, it does not offer a reliable ground truth, where tests using RTK-GNSS presented up to 1.5 m error, far greater than the robot dimensions and nominal row spacing. A stick to raise GNSS antenna above coverage is not feasible since plants have more than 2 m and such stick would get entangled and heavily oscillate due to ground unevenness. Allied to that, the ground unevenness/clutter combined with the robot's light weight worsens the odometry/IMU measurements. Markers placed on ground would require constant maintenance because the robot would go over it, which also raises a ground condition change. For such reasons, the LiDAR readings themselves are chosen to evaluate the perception performance.

A ground truth can be acquired by manually choosing the best lines for each lateral row in the LiDAR data. This requires frame by frame inspection to determine four points for each frame (two per side). Subsequently, Eq. 3.7 computes the lateral distances. These two values, manually obtained distance left and right can be combined in similar way as ***PL*** estimates: 1. Ground Truth Lane Width (LW^{GT}) with Eq. 3.2); 2. Ground Truth Cross Track Error (CTE^{GT}) with Eq. 3.3. These values can be directly compared to ***PL*** outputs.

Table 1 – Intervention Types related to the interaction between robot and environment. All of these require manual operation to recover robot to autonomous mode.

Type	**Front camera frame**	**LiDAR scan**	**Description**
Middle of Lane Stop		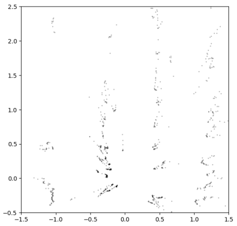	This happens when robot stops either from operator request or safety emergency stop.
End of Lane		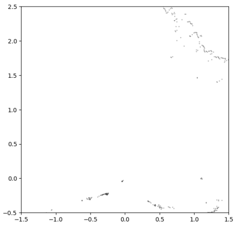	This happens when robot reaches end of lane.
Left Hit		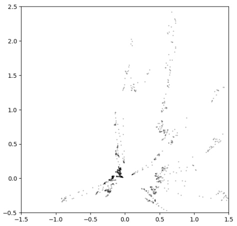	This happens when robot hits the left row of the lane it should be following.
Right Hit		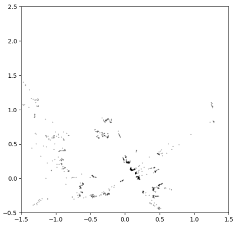	This happens when robot hits the right row of the lane it should be following.
Gap		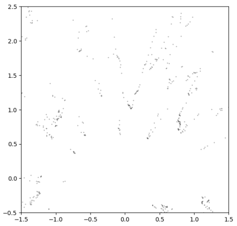	This happens when robot cannot find entrance to lane after a gap.

Source: author.

3.6.1.2 Quantity to assess performance

In general terms, CTE is a great indicator of control performance, as it closely describes the path performed by the robot while driving in the middle of the rows. For example, it is possible to analyze oscillatory behaviour, overshoot and steady state error. Additionally, it indicates when disturbances (mostly due to ground influence) occurred by observing inconsistencies in the (CTE). Disturbances in the ground make the robot to slip, slide and/or fall that lead to lateral row estimation discontinuities, subsequently (CTE) also has sudden changes. Nonetheless, exactly for also accounting the control and disturbances, (CTE) does not contribute to a straightforward characterization of perception performance. For this to happen, an external source of positioning such as a centimeter-level accurate RTK-GNSS would be required to eliminate the influences other than the perception itself.

On the other hand, an appropriate perception subsystem should correctly estimate LW regardless of the robot's position between rows. Moreover, manual ground truth provides expected lateral distances, which can be compared to the estimated values. Henceforth, LW, either compared with its counterpart ground truth or the expected row spacing, is selected as a major quantitative measure of the perception performance.

3.6.1.3 Visual interpretation of experiments

Additionally, a visual reconstruction of traversed crop lanes may be achieved from the knowledge of the lateral distances coupled to the respective robot's localization. With respect to the axis traversal to movement, the instantaneous position y^R is given by CTE. And with respect to the axis along movement, the position x^R can be estimated from the robot's forward speed v_x integrated over time. The $\boldsymbol{PL}$ also outputs the heading relative to the rows ϕ, which is assumed as the robot's heading ϕ^R. For a given instant k, Eq. 3.21 shows the robot's pose.

$$\begin{aligned} x_k^R &= x_{k-1}^R + v_x(t_k - t_{k-1}) \\ y_k^R &= 0.5(d_k^R - d_k^L) \\ \phi_k^R &= \phi_k \end{aligned} \tag{3.21}$$

The key point is transforming the lateral distances, which are on a local reference frame fixed on LiDAR's center, to the global reference frame given by the pose (x_R, y_R, ϕ_R). Equation 3.22 shows the required calculations to obtain the global position $[x_k^{d^L}, y_k^{d^L}, \phi_k^{d^L}]^T$ of the left lateral estimate for the instant k. An analogous calculation is performed for right side.

$$\begin{bmatrix} x_k^{d^L} \\ y_k^{d^L} \\ \phi_k^{d^L} \end{bmatrix} = \begin{bmatrix} \cos(\phi_k^R) & -\sin(\phi_k^R) & x_k^R \\ \sin(\phi_k^R) & \cos(\phi_k^R) & y_k^R \\ 0 & 0 & 1 \end{bmatrix} \begin{bmatrix} 0 \\ (-1)^\alpha d_k^L \\ 1 \end{bmatrix} \tag{3.22}$$

where α is 0 for left side and 1 for right side.

3.6.2 Full Path Navigation Field tests

The complete Full Path Navigation performance assessment is beyond this thesis scope. Nonetheless, there are several lane traversals from begin to end, further referred as segment, and they provide an insight about ***PL*** performance after EKF's measurement noise covariance R became variable. Because the complete system significantly changed throughout field tests while ***PL*** remained the same, only interventions caused by ***PL*** within lane will be discussed.

Four sets of experiments were carried out to evaluate the full path navigation system. The first three occurred in Autonomous Farm to perform paths composed of more than a single continuous lane. An U-shaped trajectory (Fig. 21a) has two 125 m segments where robot should be controlled by Perception Subsytem and one transition section to be controlled by GNSS-based navigation. An eight-shaped (Fig 21b) has fours segments (two 125 m and two 80 m) and four transitions.

Figure 21 – Desired paths (a) U-shaped (b) 8-shaped.

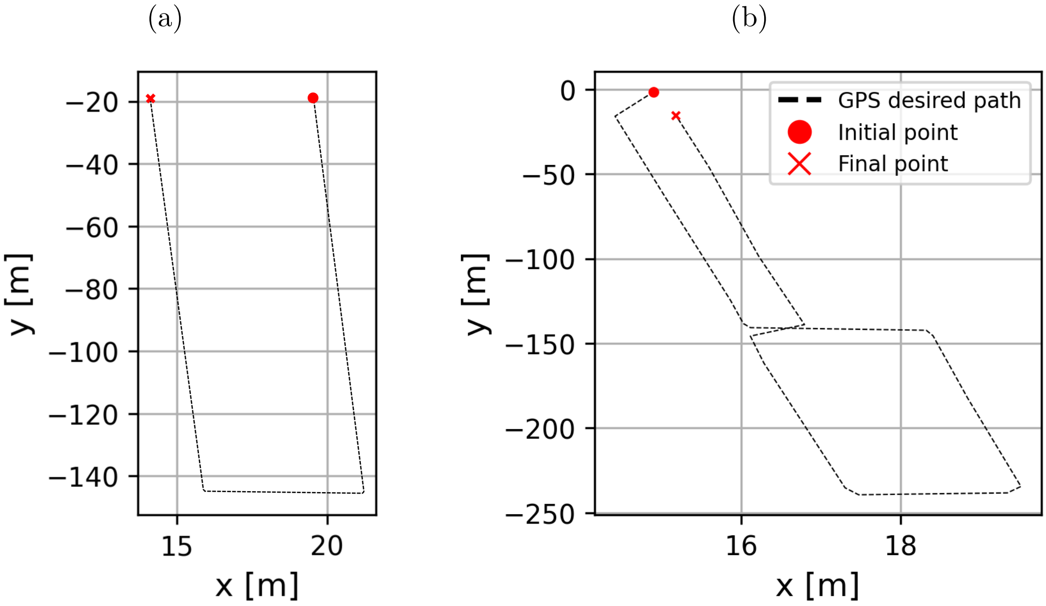

Source: author's own elaboration.

The longest achievable path in Autonomous Farm with current hardware is shown by Fig. 22a. It has seven segments and also seven transitions. The whole path has around 1.15 km where 920 m (79%) required within rows navigation. The final path (Fig. 22b) was carried out on another corn farm in Champaign, IL, where ground unevenness is highly present in the form of tractor wheel tracks. It has four 370 m segments with three transitions and due to its format, it will be further referred as serpentine path.

Figure 22 – Desired paths (a) Longest (b) Serpentine.

(a) (b)

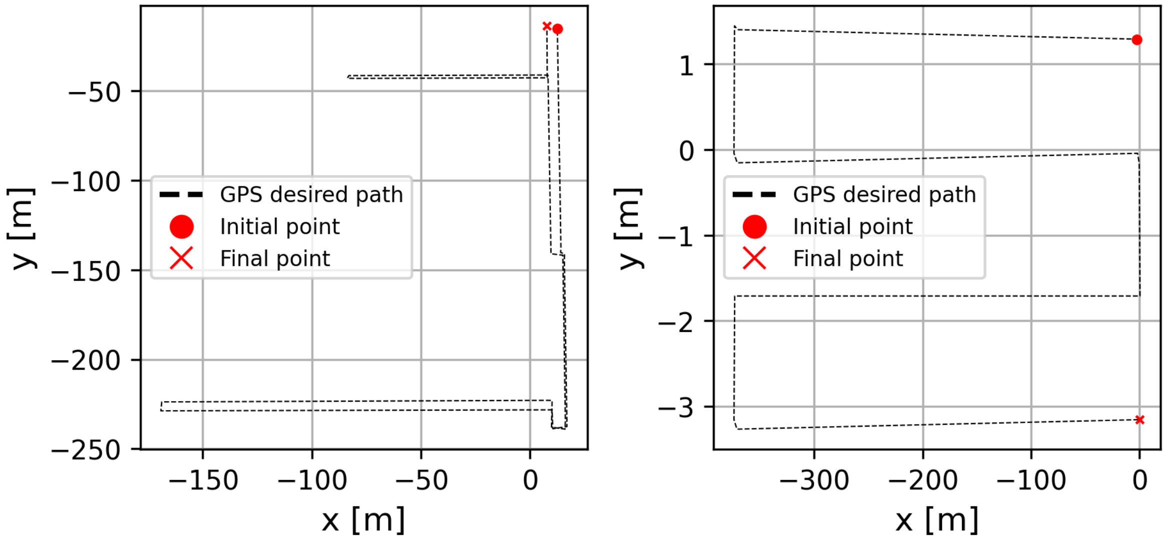

Source: author's own elaboration.

4 RESULTS

This chapter reports and discusses the field experiments from 2016 to 2020 on multiple corn and sorghum fields. First, Sec. 4.1 shows a brief overview of how studies of LiDAR-based autonomous navigation for agriculture fields started at LabRoM. Then, Sec. 4.2 presents the results using ***PL***. Subsequently, Sec. 4.3 compares ***PL***'s performance when the input comes from a standard fixed 2D LiDAR and from MLSS, the Multi-Layer Sensing System (Sec. 3.1). Section 4.4 presents the field results for ***PL+EKF***, i.e. after an EKF for distance estimation (Sec. 3.5) is coupled to ***PL***. Finally, Sec. 4.5 reports the results from *Full Path Navigation* with respect to ***PL+EKF*** performance. Supplementary videos are provided at <https://youtube.com/playlist?list=PLw-FoMhUDiCCgL4CjqeF3PzWBfzDXFzjQ>. Their number match the respective footnote along the text.

4.1 Corn planted on pods

Around 2016, the laboratory focus was on the control development. As such, a H-∞ was developed on hElvis III and tested on a set of four rows of corn planted on pods with nominal 1 m row spacing (VELASQUEZ, 2016; GUERRERO, 2016). Figure 23 shows a typical LiDAR scan in such environment.

Figure 23 – A LiDAR scan in the corn pods setup. Note that row spacing is around 1 m to have both rows well defined.

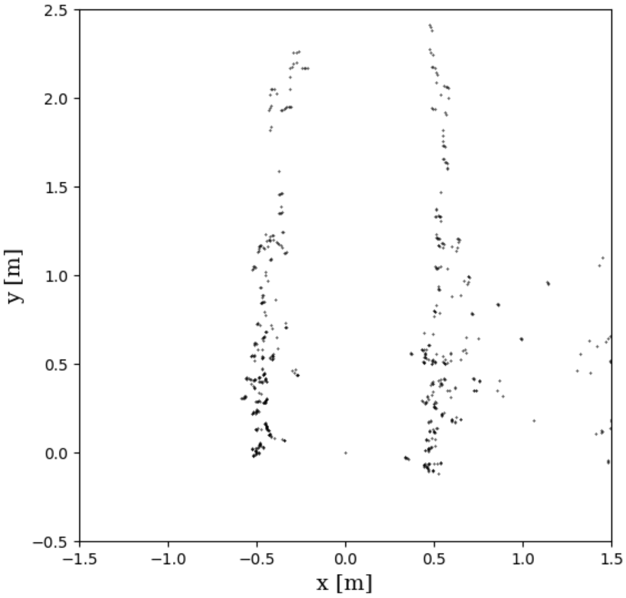

Source: author's own elaboration.

The row detection relied on the average value for a limited window of readings for each side. This is highly susceptible to weeds in the middle of lane, to hanging leaves and missing plants. For such reasons, weeds were constantly removed or at least trimmed below LiDAR's line of sight. Moreover, the 1 m row spacing is wider than standard (0.8 m) to completely avoid interaction between sides from hanging leaves. Height/stage of the plants did not interfered in the results as long stalks could be sensed by LiDAR and leaves did not hang towards middle of the lane on the sensor's plane of reading. Because no occlusion ever occurred, all failures to complete these field tests happened for two reasons: hElvis III attempts to change lanes and IMU erratic drift.

Both Guerrero (2016) and Velasquez, Higuti, Guerrero, Milori, Magalhaes and Becker (2016) include open-loop headland maneuver. The first totally relied on IMU information while the latter used a second LiDAR placed on the rear side of the robot to provide distance measurements when hElvis III was going backwards, part of the turning maneuver. Although it reached relative success in this environment, it heavily relied on well behaved entrances, i.e. no weeds, regular placement of plants and flat to low soil irregularity.

A lane reconstruction is provided by Fig. 24. First, note that lighter colors are the raw estimates, i.e. the orthogonal distance between LiDAR sensor and respective row. Therefore, they consider that robot was moving only in x-axis ($y = 0$). Equation 3.22 considers the current robot's pose to correctly place the raw estimates into a coordinate frame fixed to world, e.g. the one centered at the beginning of the lane. Such transformation results in the adjusted position of the rows (dark green for left and dark blue for right side) and the robot's path is described by magenta line (PL CTE).

Figure 24 – Reconstruction of one of the lanes from the corn pods setup. Note that hElvis III started with an offset with respect to center of the lane (see magenta line), in this case 0.159 m towards left row (dark green).

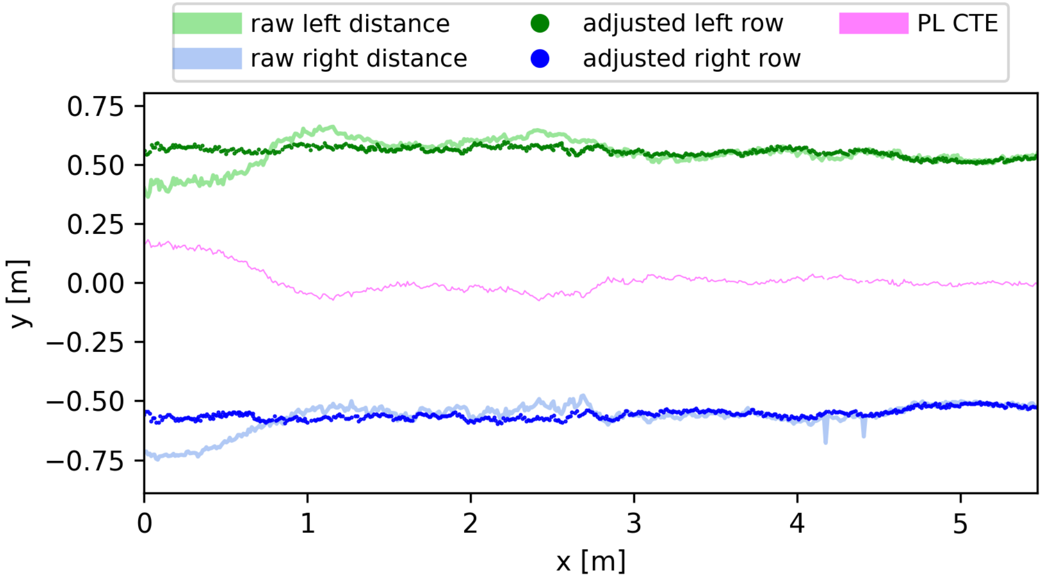

Source: author's own elaboration.

Figure 24 pictures an experiment where robot started parallel to lane but with an initial offset of 0.159 m towards left row. For such reason, its initial raw estimates indicate 0.399 m for left (light green) and 0.717 m for right side (light blue). As it can be seen by magenta line, the robot successfully returned to the center of the lane after 1 m. Such offset was imposed to evaluate the control system, out of this study's scope. An autonomous run of hElvis III performing the path is available online[1]. It is fast-forwarded 16 times. The evaluation set was composed of 65 m of autonomous navigation using this version of perception subsystem.

4.2 *Perception LiDAR* (LiDAR-only Perception Subsystem version)

Figure 25 – Conditions under TS2017/TS2018 and hElvis III have been tested. (a) Late stage corn; (b) Late stage sorghum; (c) Mock-up scenario; (d) Early stage corn; (e) Corn with weed control; (f) Corn without weed control.

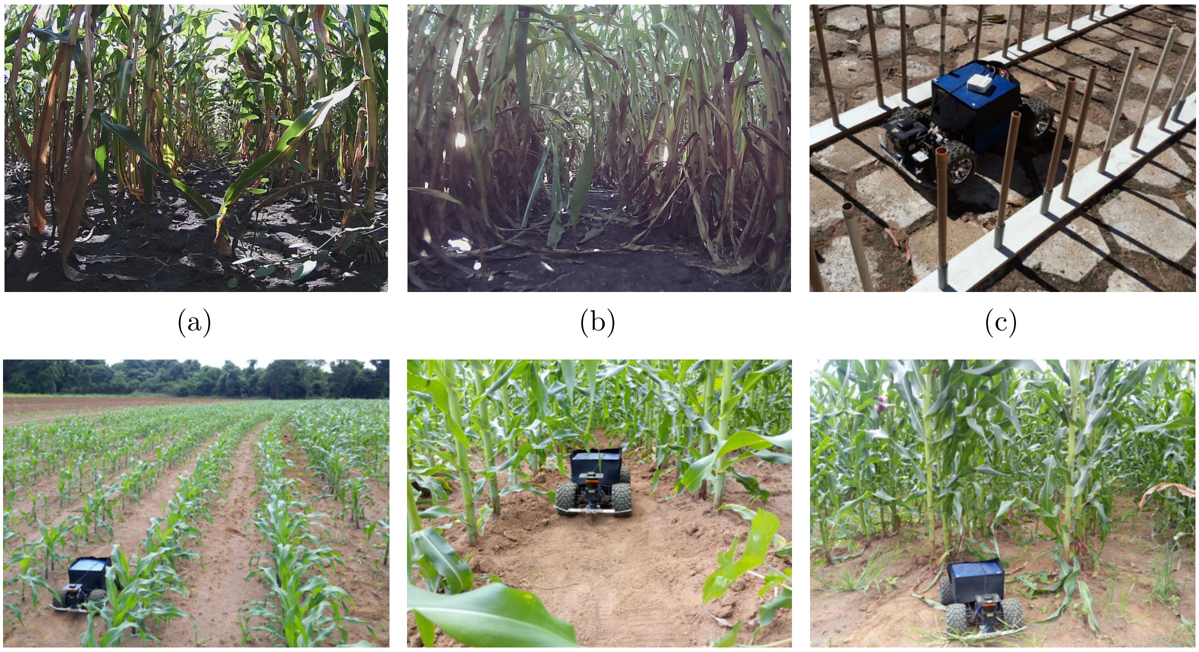

(a) (b) (c)

(d) (e) (f)

Source: (a) and (b) are retrieved from Higuti, Velasquez, Magalhaes, Becker and Chowdhary (2018) and (c)-(f) from Velasquez, Higuti, Guerrero, Gasparino, Magalhães, Aroca and Becker (2019).

The previous experience with high reliance on IMU performance, which was inconsistent, led us to develop a perception that would require only input from the laser range sensor. Another key change to enable field operation was using previous estimates to define ROIs for each lateral row instead of blindly trying to search rows within a general ROI. Such system has been tested with TerraSentia 2017 and TS2018 in 381 times in multiple corn (Fig. 25a) and sorghum (Fig. 25b) fields in the state of Illinois, logging 6247 m of

---

[1] <https://youtu.be/-lnMmoo_l4s>

autonomous run. This was performed by author and also external people using another TS2018 with same ***PL*** configuration in similar corn farms. The nominal row spacing ranges from 0.7 m to 0.9 m, majority of the lanes had rows on both sides and length was at least 3 m. Additionally, ***PL*** was tested with hElvis III in the mock-up scenario (Fig. 25c), young corn with approximately 0.5 m height (Fig. 25d), 2 m tall corn with weed control (Fig. 25e), and 2.2 m tall corn without weed control (Fig. 25f).

Table 8 summarizes the autonomous experiments, which may be part of two sets: 1) JFR and reported by *External People* with results published in Higuti, Velasquez, Magalhaes, Becker and Chowdhary (2018); 2) PA with results published in Velasquez, Higuti, Guerrero, Gasparino, Magalhães, Aroca and Becker (2019). Note that success rate, the measure of autonomously finishing the desired segment within crop, is around 89%.

Table 8 – Summary of experiments conducted with ***PL***.

Field Type	Part of	Number of Runs	Successful Runs	Success Rate	Total Distance Traveled [m]
PVC	PA set	12	$*$	$*$	90
Corn	JFR set	65	60	92.3%	2137
	PA set	7	$*$	$*$	320
	External People	70	62	88.6%	3450
Sorghum	JFR set	246	220	89.4%	660

$*$ indicates that such characteristic was not evaluated.

Source: author's own elaboration.

4.2.1 Ground Truth

Because the ground truth is manually done frame by frame, it produces the overall best achievable selection of the lateral rows while classifying scans that do not provide enough information to obtain the lines, therefore patterns can be learned. Furthermore, the use of LiDAR in later seasons of corn/sorghum is uncharted, and henceforth, the manual ground truth is fundamental to set the expectations with regards to the extraction of lateral rows in field conditions with LiDAR on the moving robot. Due to its time-consuming process, five representative experiments in the JFR set were chosen to have a glimpse of the variety of situations under which robot was submitted.

Figure 26 shows the lane width obtained with manual ground truth (LW^{GT}) in red

Figure 26 – Lane width obtained with manual ground truth (red) and with ***PL*** (blue) for five autonomous runs: Two corn, two sorghum and one highly cluttered sorghum. Nominal row spacing were 0.76 m, 0.8 m, 0.7 m, 0.91 m and 0.91 m, respectively. The black circles on boxplots are outliers, values 1.5 times interquartile-range above first or below third quartile.

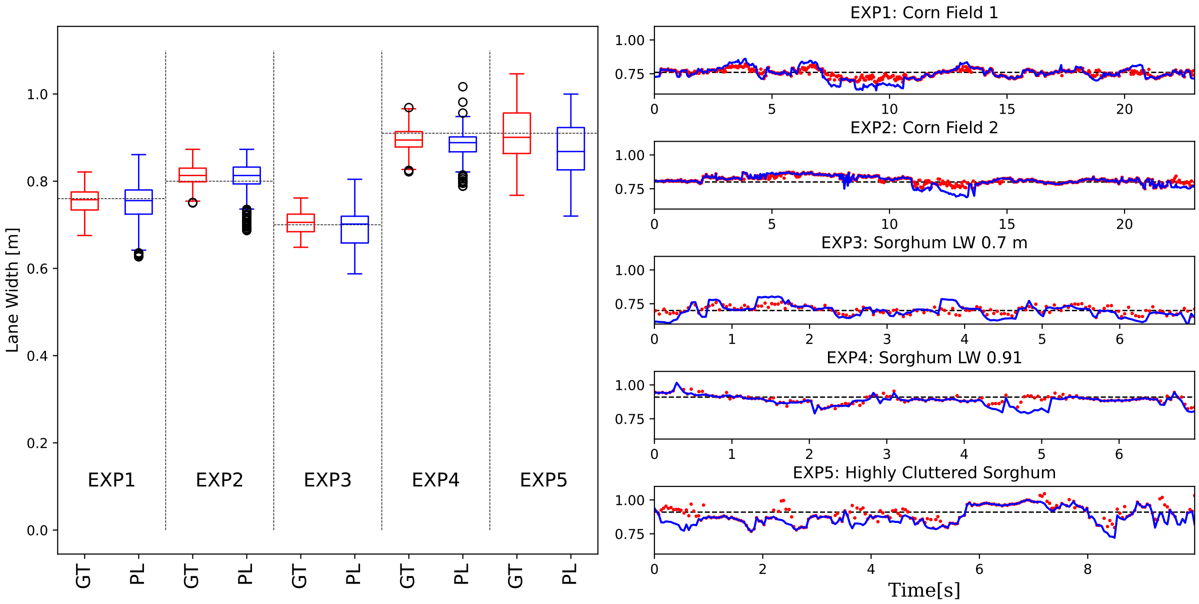

Source: author's own elaboration.

and with ***PL*** (PL) in blue for five experiments of JFR set: Two corn (EXP1 and EXP2), two standard sorghum (EXP3 and EXP4) and one highly cluttered sorghum (EXP5) where around 80% of the scans had some level of sensor occlusion. The nominal lane widths were 0.76 m, 0.8 m, 0.7 m, 0.91 m and 0.91 m, respectively. The boxplots to the left display the lane width distribution where the mean values for ground truth is close to the nominal, but also that there is a significant difference between the lowest and highest values (up to 0.27 m in EXP5). Estimations with PL are usually more spread with more outliers but its overall behavior follows the one presented by LW^{GT}. The outliers show a tendency of ***PL*** to underestimate the lane width, which is expected due to stalks being hidden by leaves, therefore a lower perceived lateral distance. Additionally, Fig. 26 also shows the time-series plots for the acquired lane widths. Especially in EXP 5, the reader can note a greater variability even for manually finding the lateral rows. This is due to the higher quantity of leaves and clutter within lane, which hides the stalks or covers the sensor.

Table 9 shows a great agreement between LW^{GT}, RS and ***PL*** outputs. The exception occurs in *Highly Cluttered Sorghum*. In this set, only 56.04% of ground truth are below 0.05 m error from nominal value and 74.88% of ***PL*** has an error lower than 0.05 m when compared to ground truth. This happened because such set has frequent occlusion of the sensor.

Table 9 – Manual ground truth (LW^{GT}) is compared to nominal value of row spacing (RS) and estimated values (PL).

Experiment	abs(LW^{GT}-RS) <0.05m [%]	abs(LW^{GT}-RS) <0.1m [%]	abs(LW^{GT}-PL) <0.05m [%]	abs(LW^{GT}-PL) <0.1m [%]
Corn I	92.06	100.00	88.20	99.79
Corn II	88.98	100.00	92.04	99.59
Sorghum I	94.81	100.00	80.52	98.05
Sorghum II	86.49	100.00	92.57	96.62
Highly Cluttered Sorghum	56.04	90.82	74.88	87.92

Source: author's own elaboration.

4.2.2 Field Experiments

The field experiments have a great variation with respect to the the LiDAR scan. It is dependent on many factors, with major influences from the culture (corn, sorghum), type (breeding, production, research) and stage of growth. This section displays selected field experiments in corn and sorghum fields to expose the most significant issues that potentially lead to perception failures. First, Figs. 27 and 28 show a LiDAR scan (subplot a), the correspondent surroundings (subplot b) and the estimated LW (subplot c) with the instantaneous value marked with a red circle. Supplementary material provides video footage of TS2017 autonomously navigating in: 1) Corn field[2]; 2) Sorghum [3]; 3) Cluttered sorghum[4] 4) A sample perception execution for corn along with GNSS measurements and frontal camera images[5].

4.2.3 LiDAR and estimated lane widths

Figure 27 shows an instant in corn crop where stalks are covered by leaves, which usually go downwards, having few leaves projecting to the lane center. This prevents picking the stems to form the lateral row, leading to LW underestimates as marked by the red circle in Fig. 27c, but it works in a conservative way to keep the robot in the middle of the lane.

Figure 28 shows a typical situation where sorghum leaves occlude LiDAR field of view. Compared to corn, there is a much higher chance to find leaves in the center of the lane, especially when the sorghum is below 2 m. As it can be seen in Fig. 28a, the LiDAR scan is hardly useful unless the previous scan information helps, such as providing the last position of the left lateral row around $x = -0.4$ m. Exactly for considering past

---

[2] <https://youtu.be/HWozE63mbXE>
[3] <https://youtu.be/1T85xOlj5q4>
[4] <https://youtu.be/bdHirrMSPio>
[5] <https://youtu.be/BMGBuP1Xuqk>

Figure 27 – Autonomous run in corn field where there is a great number of leaves covering the stems. This leads to underestimates of the lateral distances, but they are still valuable to keep the robot in the middle of the lane. Plot (a) shows a LiDAR scan with the device positioned at the origin. Plot (b) provides a view of the robot's surroundings at the instant of plot (a). Plot (c) is a *LW* time plot, having the current instant marked with a red circle.

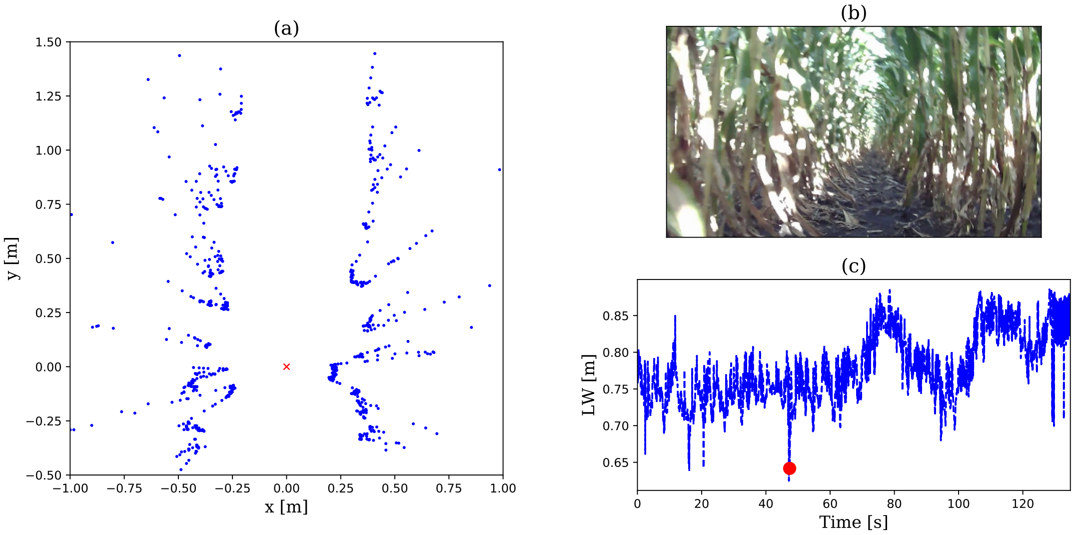

Source: author's own elaboration.

information to filter current readings, ***PL*** has been able to provide an estimate for most of the LiDAR scans.

Figure 28 – Autonomous run in sorghum field. The plots show when leaves occlude the LiDAR, a typical situation in such crop. In the case of sorghum, ***PL*** can use past estimates to filter the readings caused by the leaves interference.

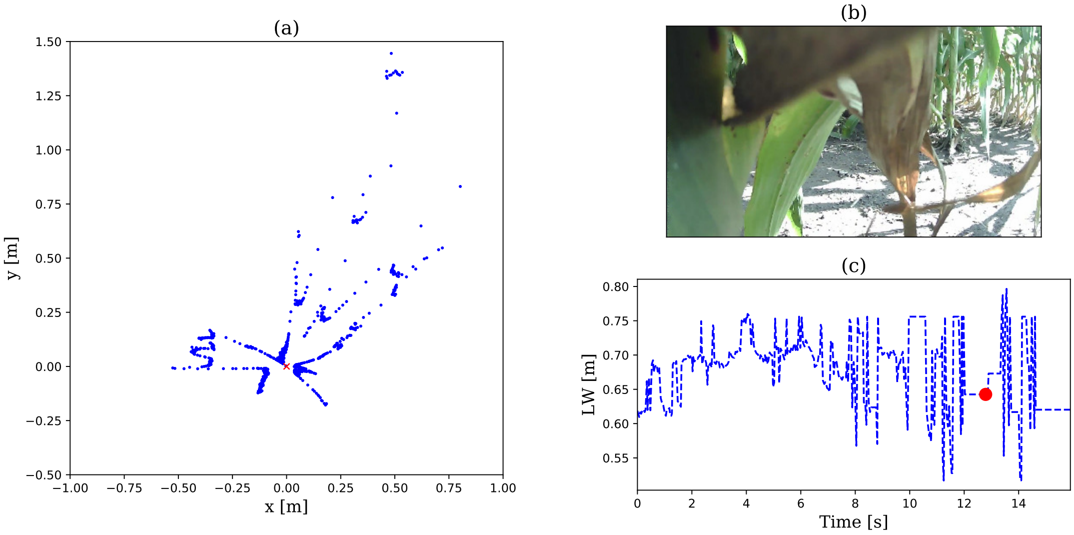

Source: author's own elaboration.

4.2.4 Field Experiments Remarks

Note that sudden changes happen in LW as it was expected from ground truth. This was bounded to happen because the $\boldsymbol{PL}$ filters out a significant portion of the LiDAR readings resulting in small regions of used measurements for the line fitting, but it does not classify whether the reading pertains to a leaf or a stem. Also note that close to the end of the experiments LW becomes even more unstable or it gets fixed at the RS. This happens because of the natural decrease of information in the end of the row and increasingly less readings are used to generate the lateral row. If any of the obtained lines are judged as invalid by ***Validate*** stage in $\boldsymbol{PL}$, then estimated lateral distances are adjusted such that their sum results in the nominal value.

4.3 Experiments with MLSS

Figure 29 shows the experimental site for the MLSS field tests. It is a corn crop with standard row spacing of 0.8 m. A suitable row containing significant number of leaves on both LiDAR sensors was chosen to compare the lateral distance estimates. Because MLSS had processing times averaging 0.3 s, field data was collected in manual mode and offline processed. For each experiment, hElvis IV traveled roughly 10 m with an average forward speed of 0.2 m/s. The findings were reported in Gasparino, Higuti, Velasquez and Becker (2020). An unsuccessful trial of autonomous hElvis using MLSS is provided in the supplementary material[6].

Figure 29 – Corn crop on Embrapa Lanapre's facility

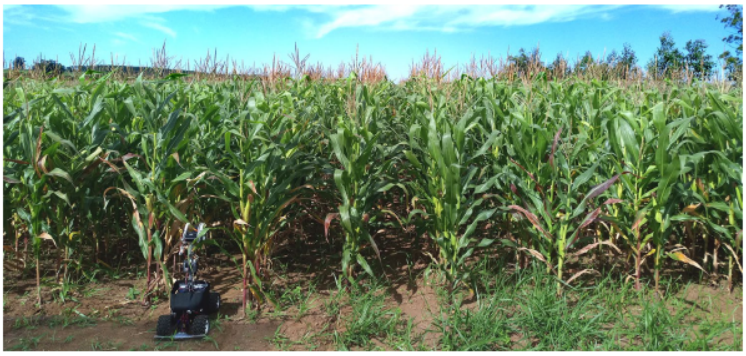

Source: retrieved from Gasparino, Higuti, Velasquez and Becker (2020).

Figure 30 presents eight experiments. The estimated lane width mean value and standard deviation were offline calculated using $\boldsymbol{PL}$ for *Standard LiDAR* (fixed in the robot's front and reading plane parallel to ground) and MLSS. Although mean values of both systems are around the nominal value, MLSS has lower variation within different experiments and also lower standard deviation within a single run than *Standard LiDAR*.

---

[6] <https://youtu.be/_Ij8UfwekUY>

Figure 30 – Estimated lane width mean value and standard deviation for each of the experiments. Blue/navy elements for estimates based on the *Standard LiDAR*, a fixed 2D Hokuyo UTM-30LX, and red/orange for MLSS estimations.

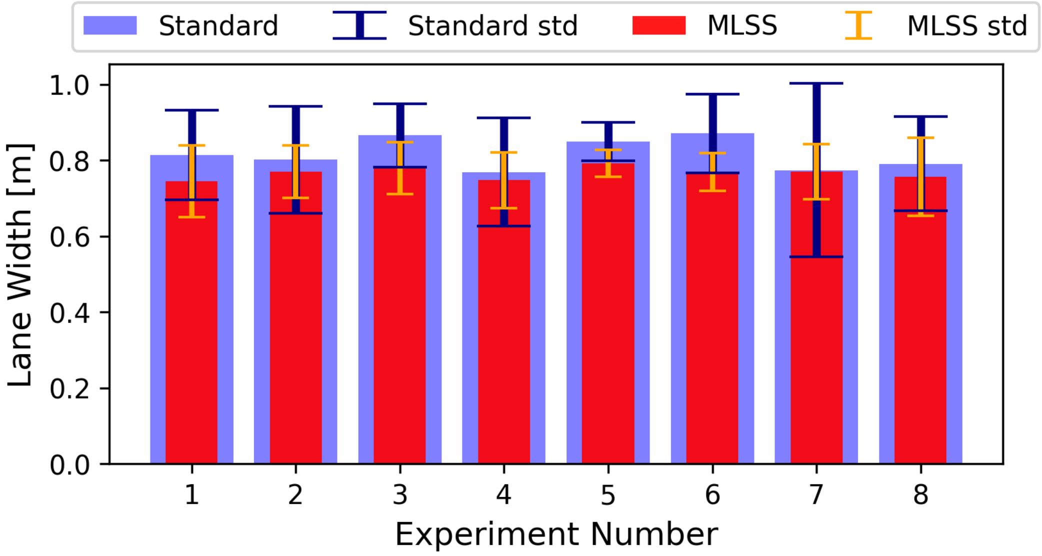

Source: generated based on data from Gasparino, Higuti, Velasquez and Becker (2020).

Figures 31 and 32 show the lane reconstruction for a field trial where the robot turned left (see 2 m in x-axis), stayed close to left wall for around four meters and then roughly returned to center. Such situation allows us to compare how the two different inputs affected PL performance since there will be a greater number of leaves that can cover the sensor when robot is closer to one side. It is noticeable in Fig. 31 that PL had severe issues to obtain estimates, especially for right side, using *Standard LiDAR*. Only 11.63% of *LW* are within 0.05 m error range from nominal value and 22.28% exceed 0.1 m difference.

On the other hand, Fig. 32 presents the PL output using MLSS. It is less affected but also under-measured the lateral displacement. In this case, 64.02% are within 0.05 m limits and only 1.92% is above 0.1 m error.

4.4 Perception Subsystem with EKF for distance estimation (*PL+EKF*)

PL+EKF was field evaluated in several corn crops in USA. The matrices Q and R , respectively model and measurement error covariance matrices, took into account the sensor's expected accuracy. Therefore, Q has been set to $\mathrm{diag}\begin{pmatrix}0.001 & 0.001 & 0.01 & 0.01\end{pmatrix}$ and R to $\mathrm{diag}\begin{pmatrix}0.05 & 0.05 & 0.5 & 0.5\end{pmatrix}$. Section 4.4.1 provides a direct comparison between the system with (PL+EKF) and without EKF (PL) usage. Then, sections 4.4.3, 4.4.2 and 4.4.4 present additional field reports with TerraSentia robot running only PL+EKF. These additional sets have been provided by EarthSense.

Figure 31 – Lane reconstructed from distance estimates using the Standard 2D LiDAR output

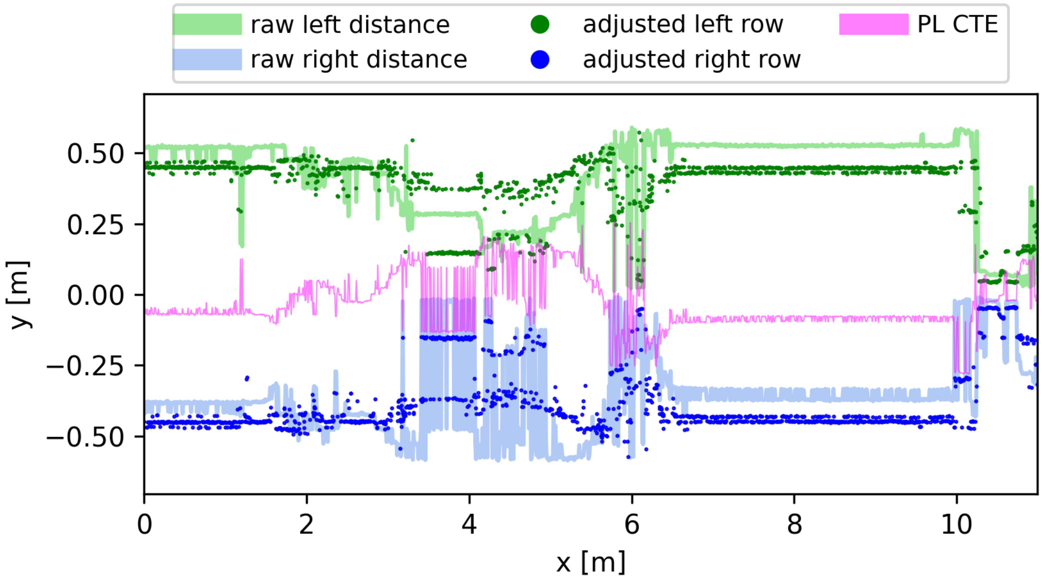

Source: author's own elaboration.

Figure 32 – Lane reconstructed from distance estimates using the output from MLSS

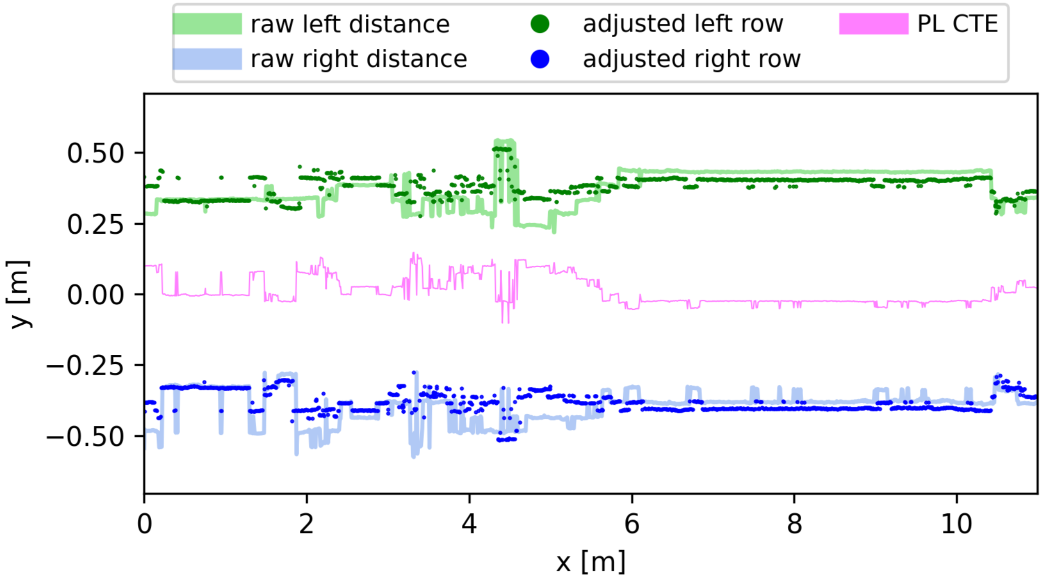

Source: author's own elaboration.

In these experiments, Perception Subsystem (both ***PL*** and ***PL+EKF***) uses the LiDAR readings inside a bounding box from 0.1 m to 1.9 m ahead and 0.75 m to both sides of the sensor. Opposed to previous work, the distance readings behind LiDAR are not considered anymore. Because robot has been facing denser crops, robot may push away straying leaves that are in the middle of the lane. But as soon as the robot passes, those leaves bounce back and usually form a dense curved shape, which allows multiple starting points for straight lines, depending on the forward occlusion.

4.4.1 Controlled Tests

The controlled tests happened in two sites: the UIUC research corn field, further referred as Autonomous Farm, and in a commercial-like farm with curve, both in Urbana-Champaign, Illinois, USA. Figure 33 shows the average field condition for each set of tests. The 42 experiments occurred in five scenarios: straight rows, straight rows with gaps, varied LiDAR update rate, border rows, and a commercial crop. The first scenario (lane A) is the best case where both rows exist from begin to end of lane (Fig. 33a). The second (lane B) has 12 gaps from 0.5 m to 1 m and 1 gap of 2 m (Fig. 33b). The length of both rows were 220 m and their nominal row spacing was 0.75 m. Third scenario used the same lanes and the LiDAR readings were used with different update rates. Fourth were 125 m length border rows (Fig. 33c, d). Finally, fifth scenario was a commercial-like corn crop with 300 m lanes containing a curved section with minimum curvature radius of 8 m (Fig. 33e, f). As a final remark about the field characteristics, usual plant spacing within lane is around 10 plants/m but it randomly varies in the border rows condition (Figure 33d) or it changes due to artificial gaps along the rows (Figure 33b).

Figure 33 – Plots (a) to (e) are from Autonomous Farm. (a) Continuous rows in a research corn crop; (b) Lane with gaps in the research corn crop; (c) External border row of the research corn crop; (d) Internal border row of the research corn crop; (e) Straight part of a row in the commercial corn crop; and (f) Curve part of a row in the commercial corn crop.

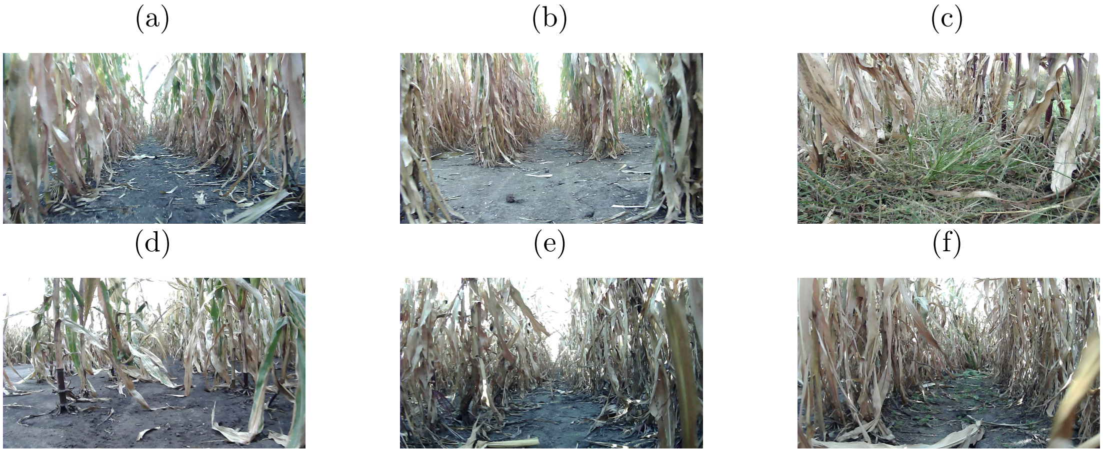

Source: DASLab database.

In general, the error that most leads to collisions is a heading estimation error. To find the lateral rows, Perception Subsystem assumes that Y_P axis (see Fig. 18) divides readings into two regions: one to the left and another to the right. Subsequently, the lateral distance estimate is computed from the respective side set. When heading is wrong, e.g. a $\phi = 0$ in Fig. 18 and Y_P collapses to Y_R, we can expect that top right readings become part of the left set. With this, the left side estimate will point towards right and robot will drive away from left side instead of going towards it to return the robot to the lane center. It should be noted that the scan in Fig. 18 is ideal while field conditions that lead to this error include partial/complete occlusion, leaves that completely block the stem detection, local convergence of rows, and weeds. There are different causes for such error and they will be discussed in the following sections. First, a discussion about ground truth and estimated lane width is provided.

4.4.1.1 Ground Truth

Figure 34 – Dispersion of manual ground truth for the controlled scenarios.

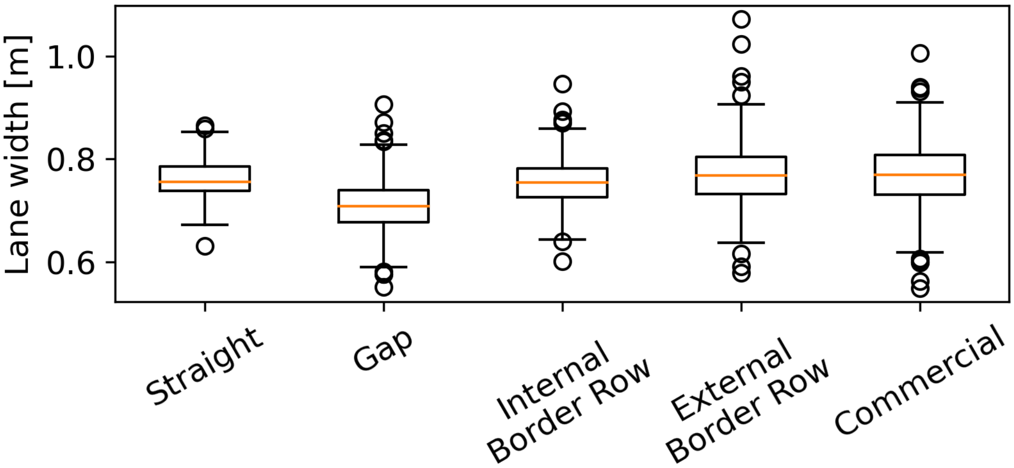

Source: author's own elaboration using DASLab database.

Manual ground truth was obtained for at least 200 scans for each scenario. Figure 34 shows the dispersion for LW_{GT}. Although nominal row spacing is 0.75 m, actual lane width greatly varies and we can expect values from 0.548 to 1.072 m, although at least 83.884% should be within 0.1 m difference. More details are shown by Tab. 10. Both sides may not be always detectable on a scan (see percentage of valid sides) due to occlusion by leaves, gap or sparseness. With respect to difference between annotated lane width and expected value, the difference is lower in the continuous straight lane as expected (83.246% within 0.05 m).

Such difference occurs due to environment characteristics. Gaps are particularly problematic because they introduce several begins and ends of lane. The begin may be blocked by leaves, weeds, fallen plants and LiDAR may not clearly see ahead. There is a progressing drop in readings as robot approaches the end. These two interferes in the process of finding a line representation for the respective side. Similarly, sparseness of plants (mostly in internal border rows) make the system more prone to consider eventual cluster of leaves or weeds as part of the row since there are few plants actually forming the row. In external border rows, there was a great influence of ground unevenness combined with the large amount of clutter along lane. Finally, in the commercial crop, besides mentioned issues, lane width consistency is compromised due to denser foliage, corn that grew angled and the curve.

Table 10 – Manual ground truth for the controlled scenarios.

	Valid left side[%]	Valid right side [%]	Avg. LW^{GT} [m]	abs($LW^{GT} - RS$) < 0.05 m [%]	abs($LW^{GT} - RS$) < 0.1 m [%]
Straight	96	99.500	0.762	83.246	97.906
Gap	96.011	93.162	0.708	53.355	87.700
Internal Border Row	78.200	91.600	0.754	76.218	95.129
External Border Row	84.053	97.010	0.771	65.164	89.344
Commercial	94.340	81.761	0.766	54.959	83.884

Source: author's own elaboration using DASLab database.

The average LW varied from 0.714 to 0.734 for A with a maximum standard deviation of 0.035 m, and from 0.717 to 0.736 for B with a maximum standard deviation of 0.036 m. At least 98% fall within 0.1 m error from the average value of respective experiment. The difference from EKF usage becomes evident for the 0.05 m error: while PL+EKF kept at least 94% for A and 98.5% for B, PL had 83.6%, 86.8% for A, and 86.2% and 86.6% for B.

4.4.1.2 Autonomous Farm

There were 114 interventions in this subset, which can be broadly divided into two categories: without and with EKF usage. From this total, 53 will not be considered in this analysis because 6 (11.321%) are hardware issues, 1 (1.887%) is operator manual stop, 10 (18.868%) are bad starts, and 36 (67.925%) are end of lanes. The first category, experiments without EKF usage, concentrates 86.885% (53) of the remaining 61 interventions. Subsequently, the second category shows a significant decrease in collisions happening on gaps (from 11 to 4) and PL related issues (from 41 to 4).

Lane A provides a reference as it is the less externally influenced and its representation can be seen in Fig. 35. The GNSS measurements did not achieve RTK fix and they are plotted for comparison (red). Although CTE and experimental notes indicate that robot stayed within rows and around center of lane, the same cannot be observed from the positioning given by GNSS.

Table 11 shows that five interventions happened in runs 1 and 3. Except the second one for PL, all of them were end-of-lane interventions, i.e. robot got to the end of the lane and required manual operation to go to next lane. That intervention was a collision after

Figure 35 – Representation of lane A. The vertical gray line represents the end-of-lane intervention.

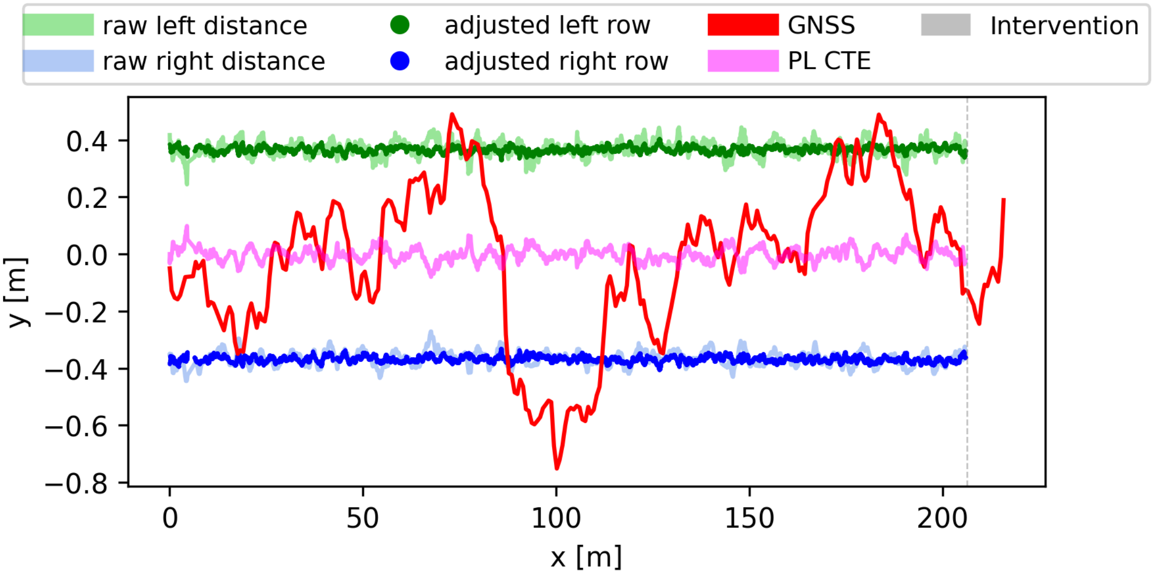

Source: author’s own elaboration using DASLab database.

heading estimation diverged due to most of both sides being occluded by leaves in the middle of the path.

Table 11 – Number of interventions on lanes A (straight with gaps) and B (straight and continuous) in Autonomous Farm.

	Run (Lane)			
	1(A)	2(B)	3(A)	4(B)
PL+EKF	1	1	1	2
PL	1	5	2	7

Source: author’s own elaboration using DASLab database.

All not end-of-lane interventions (8 of 12 for B) happened while crossing or soon after robot crossed the gap. This happened because of heading estimation error. In this case, as robot approaches a gap, there are fewer readings from the rows and they may not be from stems. These two factors combined destabilize heading estimation near gap. To illustrate this, Fig. 36 shows heading estimates from Perception Subsystem (blue and red dots) and yaw measurements from IMU (light blue and magenta lines) for the same gap in both 1(B) experiments.

The gray dashed box represents the time window when robot crossed the gap. It may be noted that estimates worsen as robot approaches the gaps. Because of such bad heading, even though rows may be visible after gap, they are split into wrong sets and robot may be following bad fitted lines. Indeed, the estimates greatly differed from expected inside gap window but they recovered as robot approached the rows (right side of

Figure 36 – Heading analysis around gap (gray dashed box) for both runs in lane 2(B): blueish features for the run using ***PL+EKF*** and reddish for the ***PL*** run, without EKF. For each run, the dots depict the heading estimate from perception subsystem, dark blue for ***PL+EKF*** and red for ***PL***, while the dotted lines show the respective heading reading from IMU, light blue for ***PL+EKF*** and magenta for ***PL***.

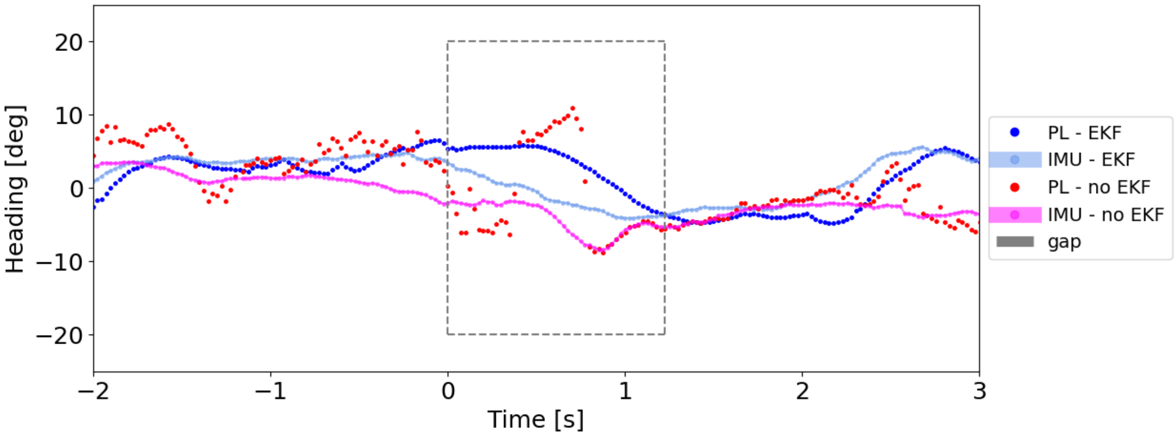

Source: author's own elaboration using DASLab database.

the dashed box in Fig. 36). Depending on how misaligned the robot left rows before gap, it may run diagonally, and can hit one of the rows, enter the neighbor lane or recover to the correct lane. This last option, when robot was already going away, is usually accompanied by a strong control action that causes an oscillatory driving and robot may crash soon after it enters the lane. Finally, Fig. 36 also exposes the difference between PL (red) and PL+EKF (blue). The estimates with EKF do not disperse and resemble the IMU readings. Even though differences are bigger around gaps, they are not as drastic as without EKF and they even allowed robot to cross all minor gaps. The only collision occurred in the 2 m gap, when robot lost track of the lane and went away.

Table 12 – Number of interventions in runs that simulate different LiDAR frequencies. The tests occurred on the same A and B lanes.

	Run (Lane)					
	40hz		10hz		5hz	
	1(A)	2(B)	1(A)	2(B)	1(A)	2(B)
PL+EKF	1	2	1	2	1	3
PL	2	5	2	8	1	11

Source: author's own elaboration using DASLab database.

Table 12 shows the number of interventions in runs with variable LiDAR update rate. Since nominal update rate is 40 Hz, this frequency experiments agree with Tab. 13. It can be noted that number of interventions do not change when EKF is used. In lane B, both 5 Hz and 10 Hz presented three more interventions, all collisions, than 40 Hz. Besides the gap problem, less updated measurements prejudiced stabilization after occlusions because while a scan without occlusion is yet to be processed by Perception Subsystem, the robot blindly drives forward. Indeed, since calculation of control action requires updated estimates, while these are not available, the control remains the same. A constant control command coupled to a 0.7 m/s linear speed may lead to robot overshooting the reference - middle of lane. This oscillating behaviour is clear on Fig. 37 between 200 and 300 s.

Figure 37 – The cross track error comparison between PL+EKF with 5Hz (red) and 40Hz (blue).

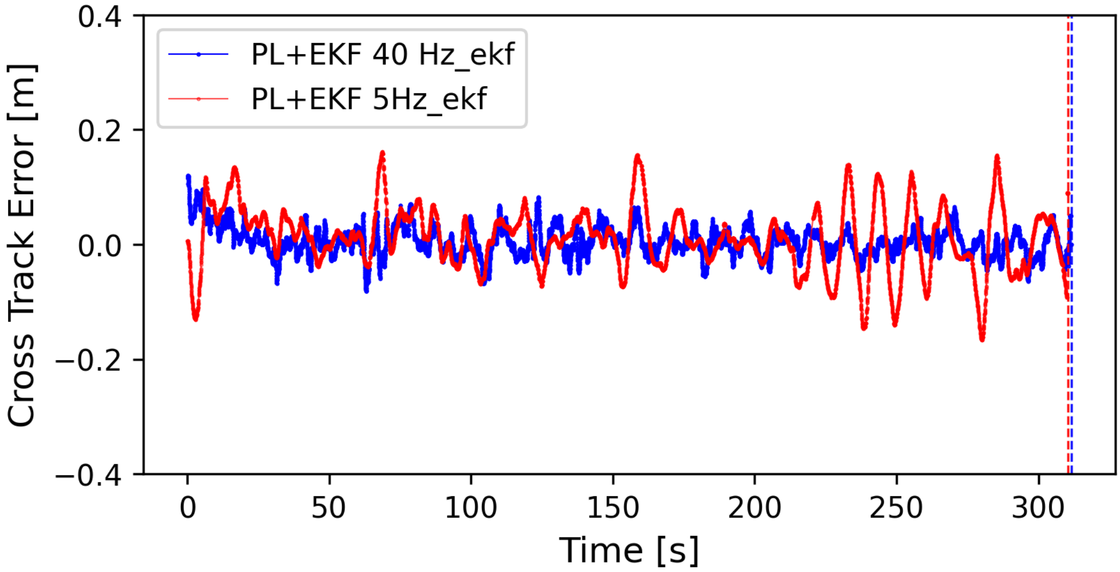

Source: author's own elaboration using DASLab database.

Fifty-four interventions happened in the border rows: 16 end-of-lane, one hardware issue, and 37 collisions. Control, hardware, bad start were responsible for 4 collisions. The other 33 happened due to some error in Perception Subsystem: could not recover from an occlusion (1), wrong distance validation step (6), wrong heading estimation (25), extended occlusion(1), and wrong point picking (2). From the five reasons, the last three either became evident or were intensified because of test characteristics, i.e. significant clutter between rows (external border rows) or scarcity of readings in some regions (internal border rows).

Figure 38 shows lane D traversed with PL. The gray vertical lines show all interventions that happened. On this experiment, GNSS could achive RTK fix and it shows great agreement between estimated path (PL) and actual one (GNSS).

4.4.1.3 Commercial-like corn crop

Finally, the last scenario in controlled tests was the commercial crop containing a section with a minimum curvature radius of 8 m. There were 72 interventions (Table 14)

Table 13 – Number of interventions in border rows of a plot in Autonomous Farm. The used lanes are two (C and D) closest to an inner path road and another two (E and F) closest to the highway. While the former ones have sparser rows than nominal due to randomly removed/fallen plants, the latter merge with roadside grass and bushes.

	Run (Lane)							
	1(C)	2(D)	3(C)	4(D)	5(E)	6(F)	7(E)	8(F)
PL+EKF	2	1	1	2	1	3	1	2
PL	6	9	4	3	4	5	4	6

Source: author’s own elaboration using DASLab database.

Figure 38 – Representation of lane D, an internal border one. Opposed to Fig. 35, there were several interventions.

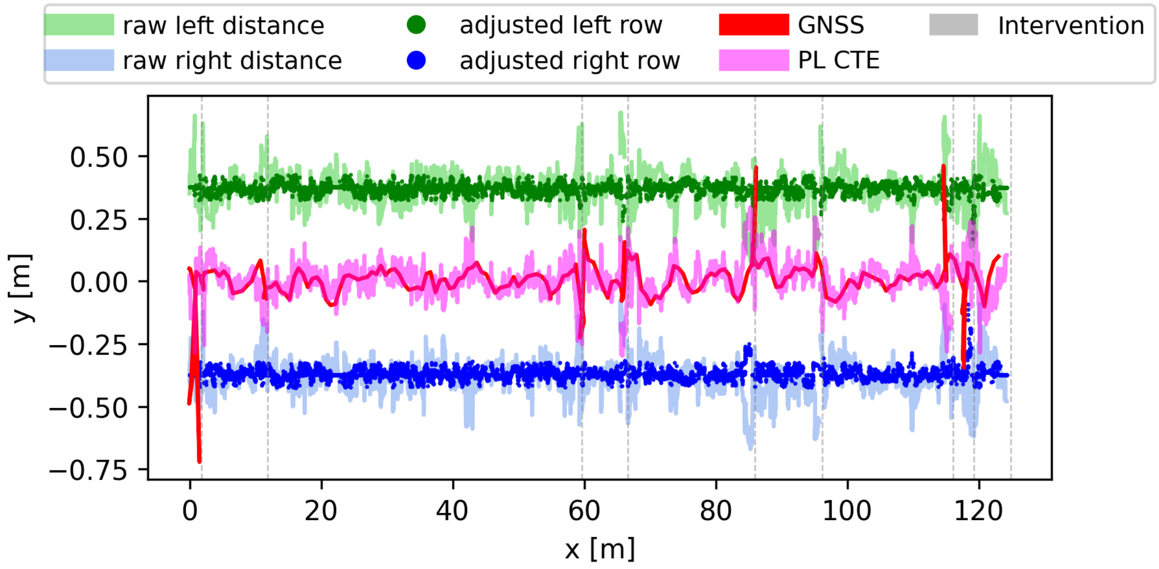

Source: author’s own elaboration using DASLab database.

in this controlled set, which can be broadly divided into two categories: without and with EKF usage. The first category, experiments without EKF usage, concentrates 82.353% (42) of the remaining 51 interventions. Subsequently, the second category (9) shows a significant decrease in collisions due to PL related issues (from 40 to 8). This section further explores particular cases that highlight the perception subsystem performance.

Table 14 – Number of interventions in a commercial corn crop.

	Run		
	1	2	3
PL+EKF	6	4	6
PL	23	13	20

Source: author’s own elaboration using DASLab database.

Figure 39 highlights the issue of having a single scanning plane: there is a horizontal leaf that blocks all readings on right side behind it. Moreover, it could be noted a converging pattern of the rows for $y \in (0, 0.5)$. Because our algorithm assumes that the angle of the best defined line is the heading error, when scan was rotated to make right row parallel to y-axis, left row became highly tilted to right. This prejudiced the point choosing step, which relies on a histogram applied to x-axis to find the 0.05 m bin with most readings. Since right row is already parallel to y-axis, most of its readings were counted in the same bin, but the same does not happen for a diagonal row such as the left whose readings were scattered on several bins. Subsequently, only the readings within the highest count bin and its neighbors are used. Therefore, the derived expression of left row contains only a small section of it.

Figure 39 – A front camera frame (a) and a LiDAR scan (b) in the commercial corn crop.

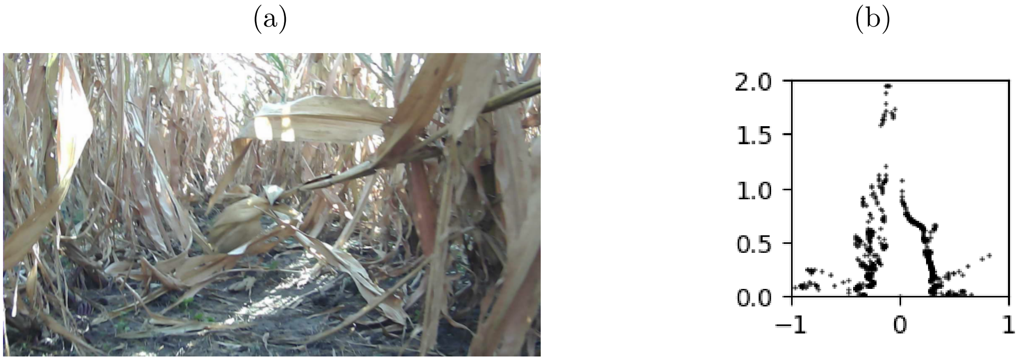

Source: author's own elaboration using DASLab database.

4.4.2 EarthSense Field Data #1

The EarthSense Field Data #1 field is composed of 125 to 150 m corn lanes divided into 5 m length plots separated by 0.5 m gaps using ***PL+EKF***. The field runs happened from August 10th, 2020 to September 21st, 2020. The reader may see a glimpse of field conditions in Fig. 40.

The complete set has 373 trials. The operator's goal was to collect visual data for the whole lane and that was achieved 356 times by combining autonomous and manual drive modes, which adds up to 50796.998 m (estimated with odometry EKF). From this total, 17795.052 m (35.032%) was performed in autonomous mode. For comparison, GNSS measurements (2.383 m average accuracy) indicate a total of 50093.227 m and 17235.844 m in autonomous mode. Figure 41a provides a visualization of the involved distances for each experiment. The gray dots reveal that majority of the experiments had a total length of either 125 or 150 m. While the green dots show the total distance, black dots refer to the largest segment within lane, both in autonomous mode. Finally, red circles highlight the 51 experiments that were analyzed. For convenience, the set was sorted in ascending way with respect to the total distance in autonomous mode.

Figure 40 – Figures (a-c) were taken on August 10th, Figs. (d-f) were taken on August 24th, Figs. (g-i) were taken on September 10th and Figs. (j-l) were taken on September 21th. Each line has an upward-pointing frontal, a lateral and an on top of robot fish-eye camera, respectively.

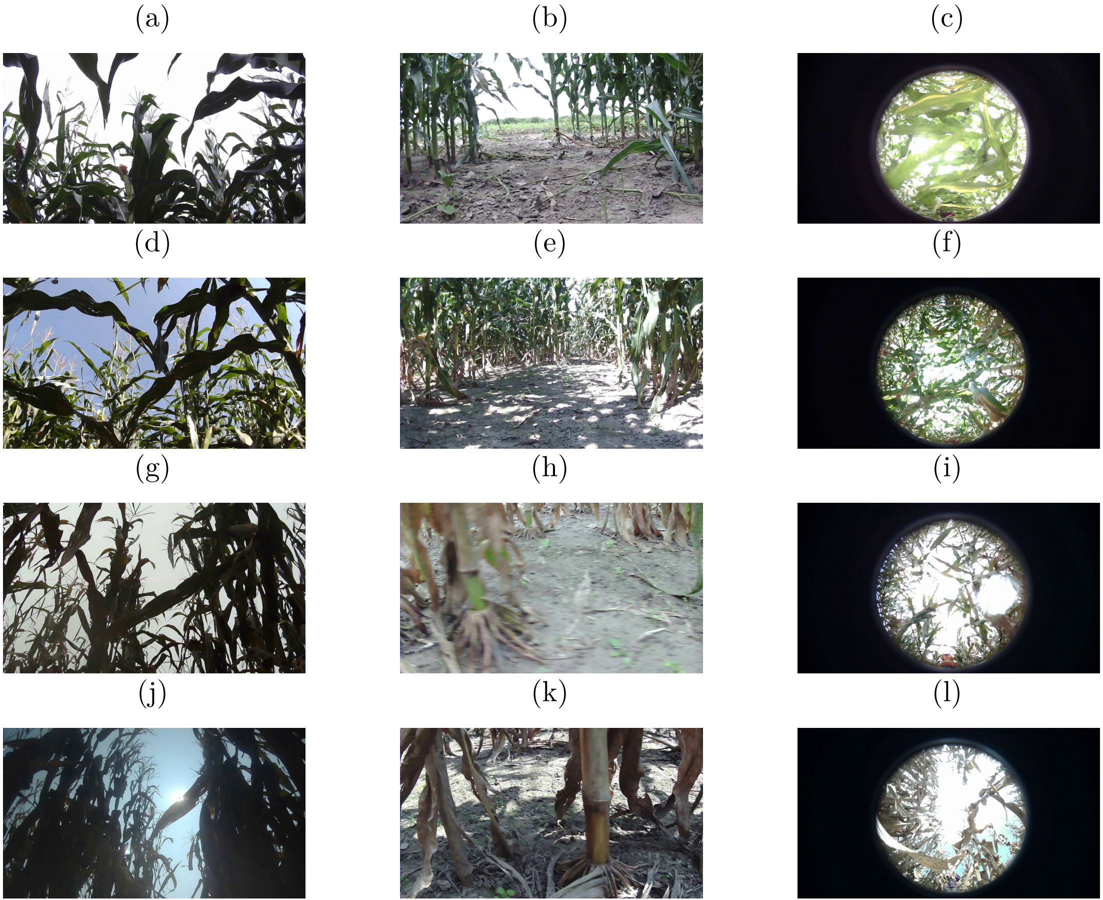

Source: EarthSense Database.

Figure 41b shows the number of occurrences, both interventions and specifically collisions due to relevant reasons. For convenience, the set was sorted in ascending way with respect to number of interventions. Again, the red crosses highlight the 51 experiments that were analyzed. The subset was chosen because the distance in autonomous mode represents more than 90% of experiments total travel and it is also greater than 100 m. Although ***PL+EKF*** still runs in manual mode, failures are not easily pinpointed as the act of stopping robot has a lot more reasons, e.g. specific plant inspection, note taking, operator rest period among others. As it can be seen in Figure 41b, experiments with higher number of interventions have not been neglected in the analysis.

There were 848 interventions, from which 202 were analyzed. They represent 23.821% of the total number and they were extracted from 51 experiments (13.673% of the runs with autonomous mode). Figure 41b also shows that number of collisions is usually lower than number of interventions. In fact, from the subset's 202 interventions, 81 will not be considered in this analysis because 7 (3.465%) are control related, 8 (3.960%) are hardware issues, 14 (6.931%) are operator manual stop, 10 (12.346%) are bad starts, and

Figure 41 – Summary of EarthSense Data #1 field experiments

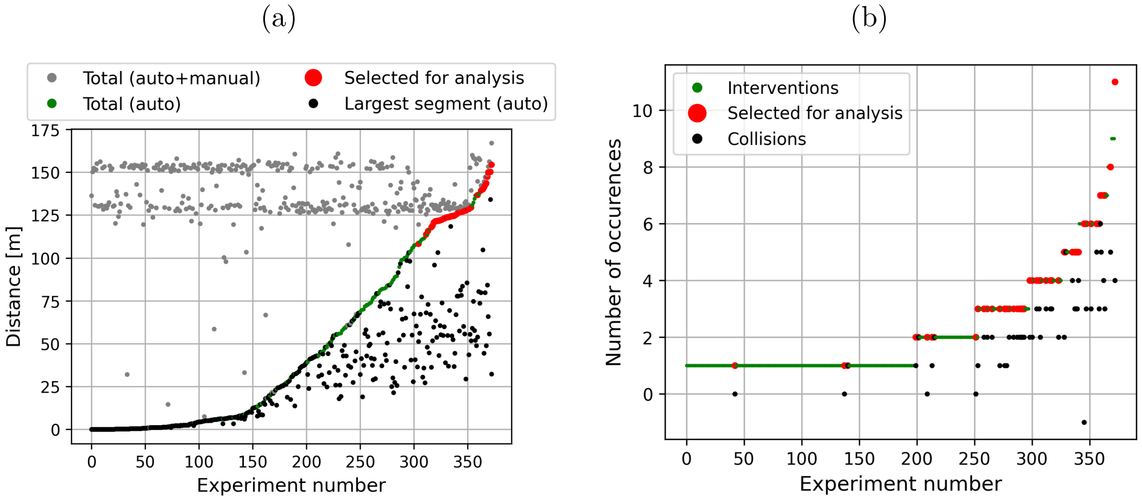

(a)

(b)

Source: author's own elaboration using EarthSense database.

42 (20.792%) are end of lanes. It follows that major cause of the remaining interventions is gap 93 (46.040% of 121) and others are:

- 9 (4.455%) estimation of heading diverges on occlusion;
- 7 (3.465%) challenging row identification;
- 4 (1.980%) convergence of rows;
- 3 (1.485%) wrong points were chosen to represent the row;
- 3 (1.485%) only one side was visible and it was not adequately tracked;
- 2 (0.990%) occlusion.

Figure 42 pictures the lane reconstruction of the longest autonomous run without collision. After around 128 m, the operator took control and drove it to another lane. Observe that standalone GNSS readings are hardly usable for navigation purpose and that gaps are not observable in the reconstruction. The latter happens because the method is always trying to fit a line for each side, even if it is ahead.

4.4.3 EarthSense Field Data #2

The second EarthSense set of ***PL+EKF*** experiments happened on a corn crop with row spacing of 0.8 m and divided into at least 75 plots of 4.8 m divided by 0.5 m gaps. The reader may see a glimpse of field conditions in Fig. 43. Each line provides picture two weeks apart (July 31st, 2020 to August 27th, 2020). The general trend that one can observe is that canopy becomes more open with both plants growing taller and also because of leaves falling off.

Figure 42 – Lane reconstruction of the longest autonomous run without collision.

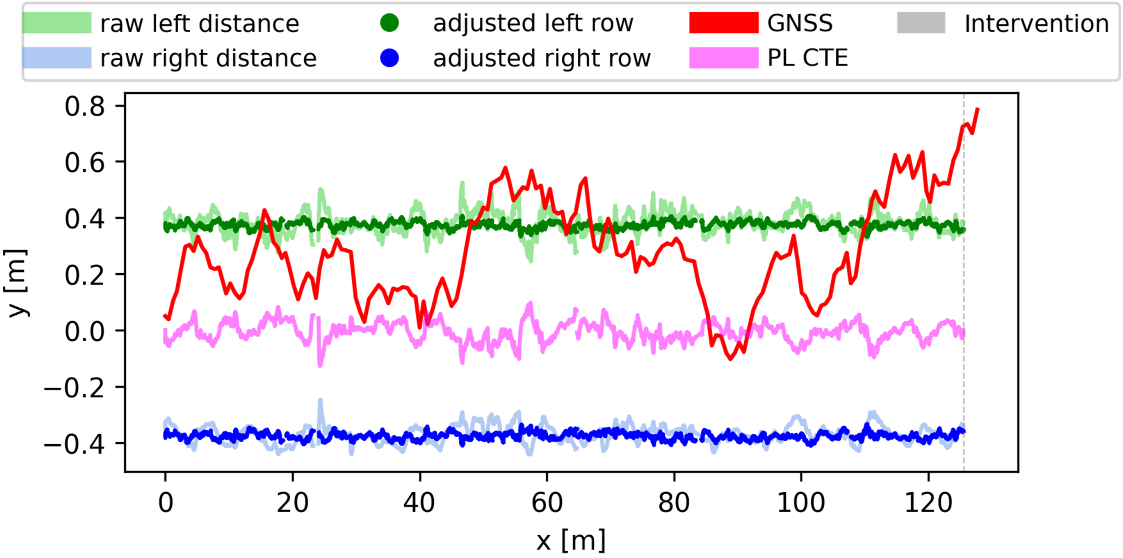

Source: author's own elaboration using EarthSense database.

Figure 43 – Figures (a-c) were taken on July 31st, Figs. (d-f) were taken on August 14th and Figs. (g-i) were taken on August 27th. Each line has an upward-pointing frontal, a lateral and an on top of robot fish-eye camera, respectively.

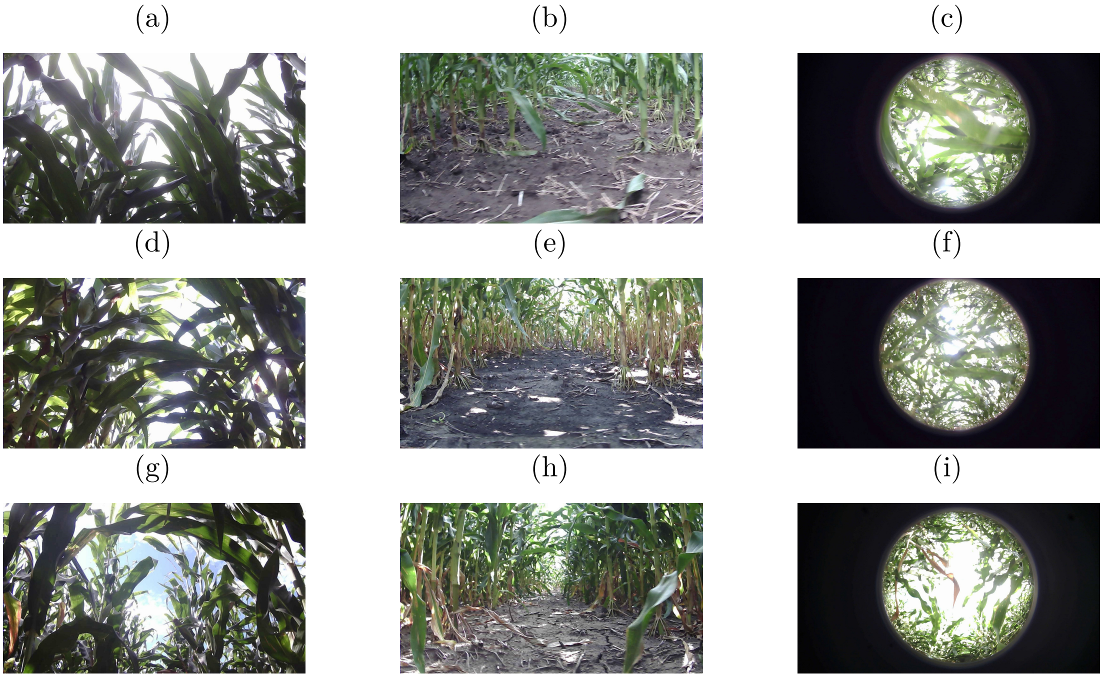

Source: EarthSense database.

The complete set has 159 runs. The operator's goal was to collect visual data for either the whole lane or specific plots, thus expected lane length varies. By summing distance traveled with both (autonomous and manual) modes, it adds up to 28992.617 m (estimated with odometry EKF). From this total, 28245.670 m (97.424%) was performed in autonomous mode. For comparison, GNSS measurements (12.385 m average accuracy) indicate a total of 22338.204 m and 20734.447 m in autonomous mode. Besides the accuracy, the large difference with respect to odometry EKF estimates (22.952%) also comes from the fact that GNSS was available for only 115 experiments. Similar to Fig. 41a, Fig. 44a shows the involved distances for each experiment. Only few (11/6.918%) required additional manual mode, which indicates that most of data collection could be achieved using autonomous mode.

Figure 44 – Performance summary for EarthSense Field Data #2 set.

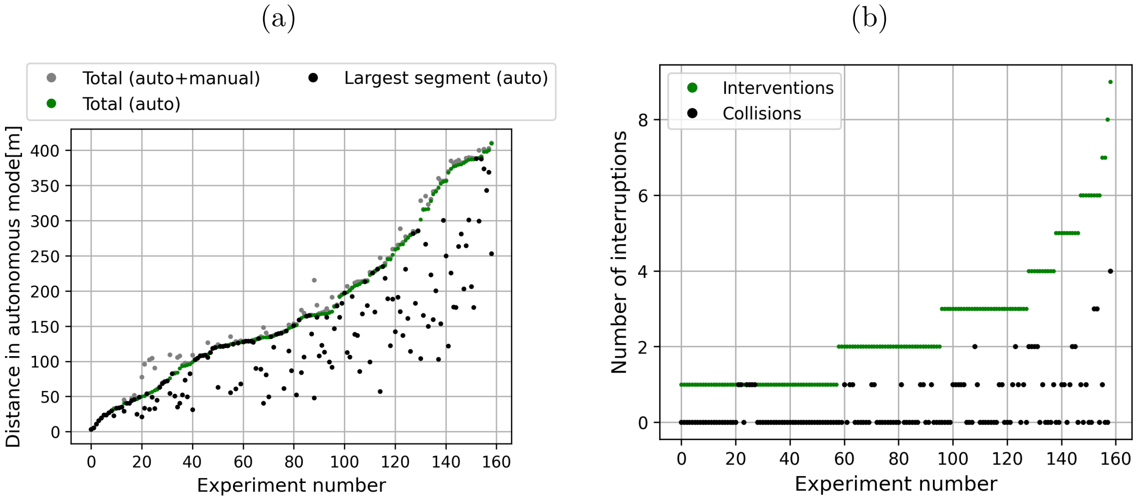

(a)

(b)

Source: author's own elaboration using EarthSense database.

There were 393 interventions. From this total, 333 were not analyzed because 13 (3.904%) are control related, 70 (21.021%) are hardware issues, 227 (68.168%) are operator manual stop, 10 (3.003%) are bad starts, and 13 (3.904%) are end of lanes. The remaining 60 resulted in collisions because of getting lost while traversing a gap (29/48.333%), ***PL+EKF*** errors (28/46.667%), and challenging row identification (3/5%). Within the 159 experiments and considering only the relevant reasons for intervention, 71.698% (114) had none, 21.384% (34) had one, 5.031% (8) had two, 1.258% (2) had three, and 0.629% (1) had four collisions. Indeed, Fig. 44b show that number of collision occurrences because of one of the relevant reasons is much lower than the actual number of interventions.

Figure 45 provides the lane reconstruction for the longest run in autonomous mode with a continuous 360 m segment without interventions. Two collisions happened (around 11 m and 371 m) when robot was trying to traverse a gap.

4.4.4 EarthSense Field Data #3

This section reports field tests with ***PL+EKF*** for a third set provided by EarthSense in a research corn farm whose nominal row spacing is 0.8 m and seeds were planted in blocks of around 7 m length with 0.5 m gap between consecutive blocks, which generates a total lane of 78 m. The field runs happened on July 20th, 2020. The reader may see a glimpse of field conditions in Fig. 46.

Figure 45 – Lane reconstruction of the longest autonomous run.

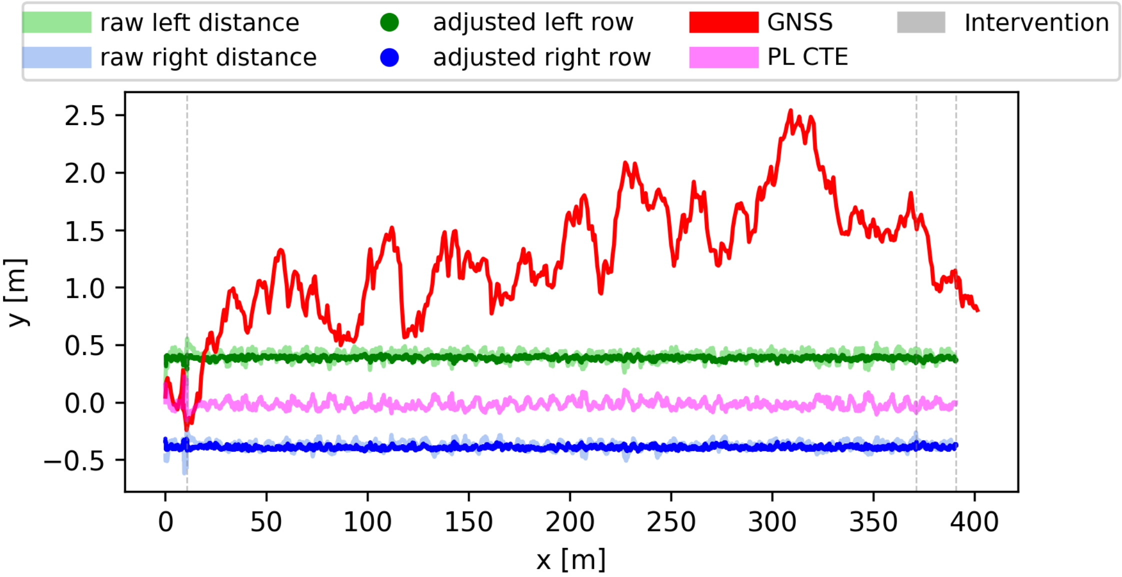

Source: author’s own elaboration using EarthSense database.

Figure 46 – Figures (a-c) were taken on July 20th. Each line has an upward-pointing frontal, a lateral and an on top of robot fish-eye camera, respectively.

(a) (b) (c)

Source: EarthSense database.

This set comprised 25 attempts to drive through a lane, i.e. from begin to end of the 78 m lanes. The operator’s goal was to collect visual data for the whole lane. The sum of distances traveled in both autonomous and manual drive modes reaches 1952.611 m (estimated with odometry EKF). From this total, 1284.824 m (65.800%) was performed in autonomous mode. For comparison, GNSS measurements (2.426 m average accuracy) indicate a total of 1881.030 m and 1230.092 m in autonomous mode.

Figure 47 pictures, for each attempt, the distance traveled in autonomous mode (green bars with gradient color to show subsequent use of autonomous mode after an intervention) and also in manual mode (salmon bars). The total distance has some variations with respect to nominal 78 m because some segments may have been skipped or repeated according to operator’s judgement. Additionally, the operator chose to manually drive the whole lane three times (#16 and #17), and decided to switch between autonomous and manual mode in another nine times. There was a failure motivation in only four of them (2 collisions after gap and 2 collisions within lane).

Figure 47 – Measured distance for each attempt to drive through a lane. The salmon bars indicate manually driven segments while different green colored bars show different usages of autonomous navigation within same lane attempt.

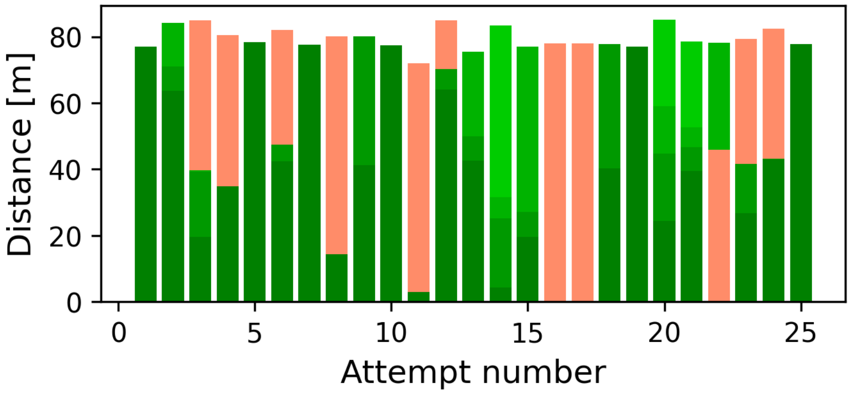

Source: author's own elaboration using EarthSense database.

Figure 48 – Lane reconstruction of a complete autonomous run (attempt #7)

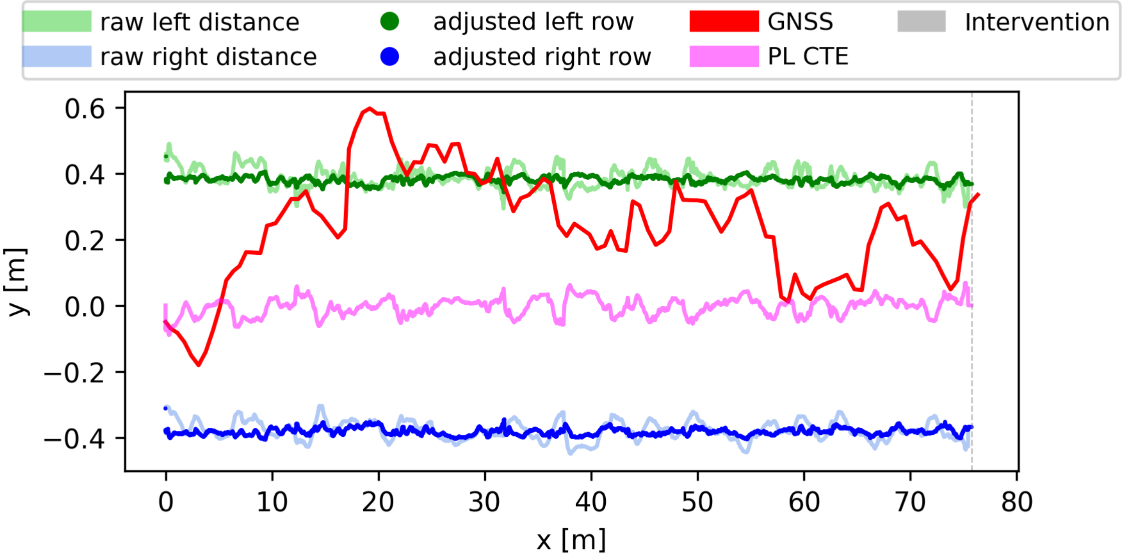

Source: author's own elaboration using EarthSense database.

The autonomous mode was used to cross 183 segments and from the subset's 49 interventions, 27 will not be considered in this analysis because 1 (3.704%) is hardware issue, 14 (51.852%) are operator manual stop, and 12 (44.444%) are end of lanes. From the remaining 22, it failed 18 times because of the gap and another four times because occlusion was mishandled by ***PL+EKF***.

Figure 48 shows the lane reconstruction of attempt #7, one that has the longest traveled distance in autonomous mode without intervention, except the final one of end of lane. Another four attempts present the same performance. Because the system does not have the ability to classify gaps, the rows are seen as continuous lines.

4.5 Full Path Navigation Field Experiments

There were 36 trials on the four paths described by Sec. 3.6.2. They are summarized in Table 15 and they were another 9.8 km of autonomous navigation. Although only few completed the whole path, the goal of this section is to analyze the segments where ***PL+EKF*** should have worked. From Table 15, very few interventions within lanes (8) happened due to perception failure. The fraction numbers in *Num segments* column not always indicate a failure, but also trials where autonomous navigation was started very close to end of lane or soon after it entered next lane because the goal was to assess the transition. The relative low number of segments compared to number of trials highlights the inability to complete whole path most of the times and the main reason was robot getting lost/ not being able to enter next lane. Besides huge gaps that required GNSS-based navigation, small sized ones (0.5 to 1 m) were not tested. The low number of considered interventions shows a similar performance as ***PL+EKF*** in the controlled set.

Table 15 – Summary of Full Path Navigation trials.

Path type	Day	Num trials	Num segments	N interventions within lane due PL
U-shaped	Aug 17th	2	2	0
	Aug 18th	4	6	0
	Aug 19th	1	1	0
8-shaped	Aug 20th	2	3.99	1
	Aug 26th	6	10.1	0
	Aug 28th	3	6	0
	Sept 11th	3	4	0
	Sept 14th	3	7	0
	Sept 21th	1	1	0
Serpentine	Sept 18th	2	3	5
	Sept 21th	1	2	0
Longest	Sept 25th	3	10.1	0
	Sept 29th	3	11.7	0
	Oct 12th	1	5.9	2

Source: author's own elaboration using DASLab database.

A successful example of each path tested in Autonomous Farm is provided by Fig. 49). The black dashed line shows the desired path. Both red and lime green dots are estimations of an EKF for localization. While red dots mark where GNSS-based navigation was used, the lime green ones reflect where ***PL+EKF*** was used. The blue numbers indicate the fraction of traveled distance, with start point being zero and one for final point. One of the challenges for current system is to recognize when it is inside/outside lanes because of the lack of contextual information from only the LiDAR data. For example, the green points close to 1 in Fig. 49a indicate that PL was used outside rows. In such case, the multiple row entrances form themselves a line that can be followed. Additionally, there are green dots soon after 0.4 in Fig. 49c. Here, the lane ended close to tall grass, and while making the U-turn, the tall grass was recognized as a row and robot started following it.

Figure 49 – Examples of successful trials on U-shaped, 8-shaped and longest paths.

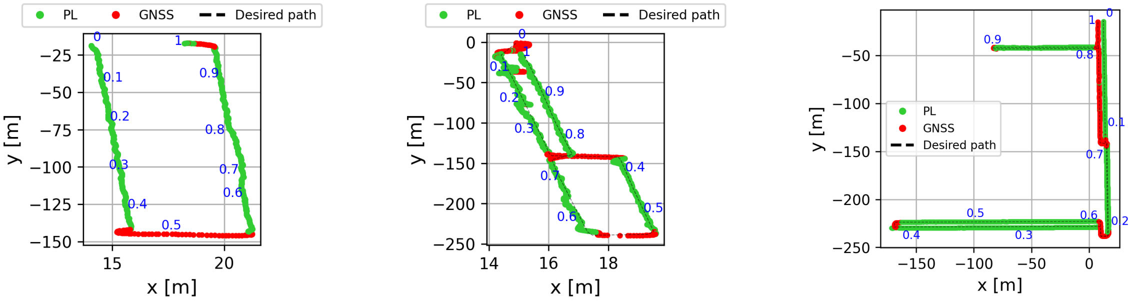
(a) (b) (c)

Source: author's own elaboration using DASLab database.

There were five interventions within lane. One happened after an occlusion of the only side (left) that was visible at time because right side had around 2 m of missing plants (Fig. 50a). This prevented ***PL+EKF*** to provide valid estimations and this led to navigation system change to GNSS-based mode (see curved red waypoints in Fig. 50b). Although ***PL+EKF*** recovered the lateral rows tracking (Fig. 50c), it was already too late for current control system to correct and robot hit the plant. A video[7] is provided as supplementary resource.

The second happened because TerraSentia spent too much time on right side without correcting the offset to lane center (Fig. 51a). Such situation increases the sensor occlusion because of leaves from the nearest row that results in overreliance on the available row. Note on Fig. 51b that estimated left row (black line) was influenced by some leaf clusters and it diverges from the actual row (blue dashed line). Therefore, instead of going towards left to at least correct the heading, robot went straight and hit the right row. A video[8] is provided as supplementary resource.

Third collision occurred after a complete occlusion because of a fallen plant in front of the robot (Fig. 52a). After the occlusion, the robot was too close to left row and although it could clearly see the right row, controller was not fast enough to correct robot towards lane center (Fig. 52b). A video[9] is provided as supplementary resource.

A ROS rviz recording[10] is provided for the longest path in Autonomous Farm. The desired path is shown by the thin light green lines. As the fixed reference frame is the

---

[7] <https://youtu.be/n_V4UGZwgSk>
[8] <https://youtu.be/Lv3Uo06p-Qs>
[9] <https://youtu.be/xXjbrWrhHk8>
[10] <https://youtu.be/gYk9hjxMSLQ>

Figure 50 – First collision. (a) Occlusion by leaf. (b) Wrong switch to GNSS-based navigation. (c) Lateral rows tracking is recovered but too late to avoid collision.

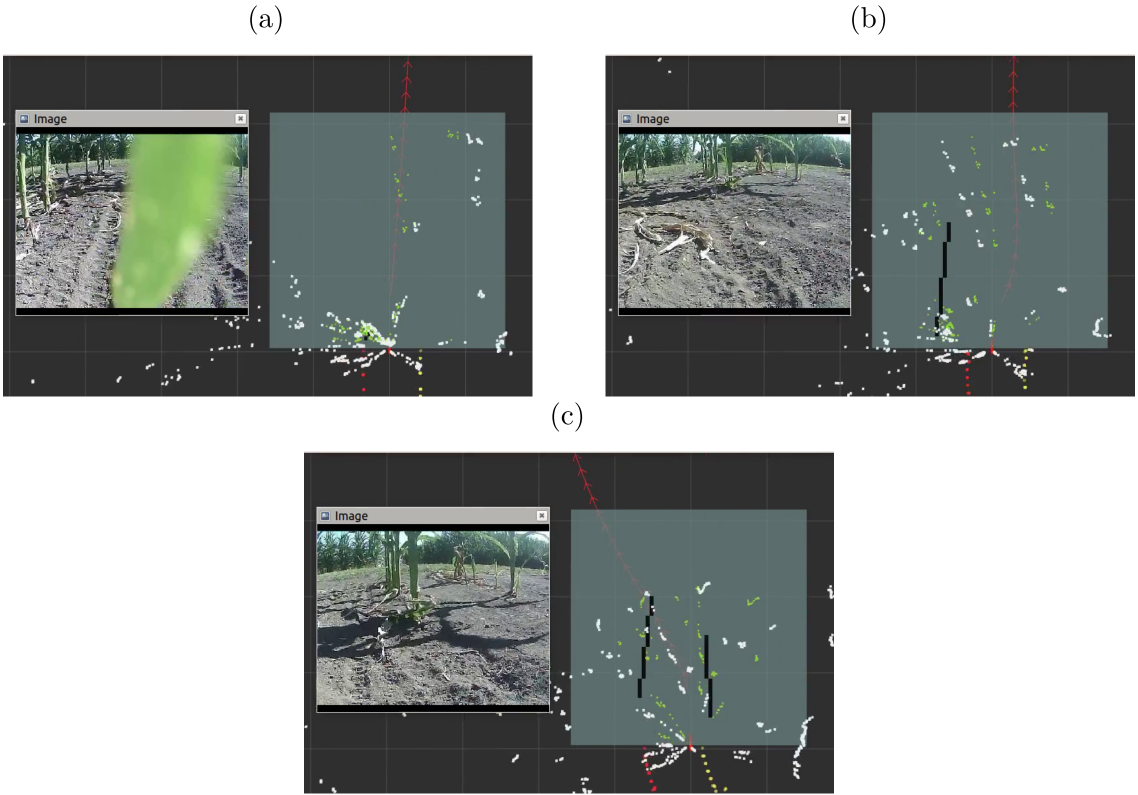

(a) (b) (c)

Source: DASLab database.

Figure 51 – Second collision. (a) TerraSentia being on right side for too long. (b) Note the leaf clusters close to left row. They resulted in a deviated left row estimate which caused robot to think it was closer to left side.

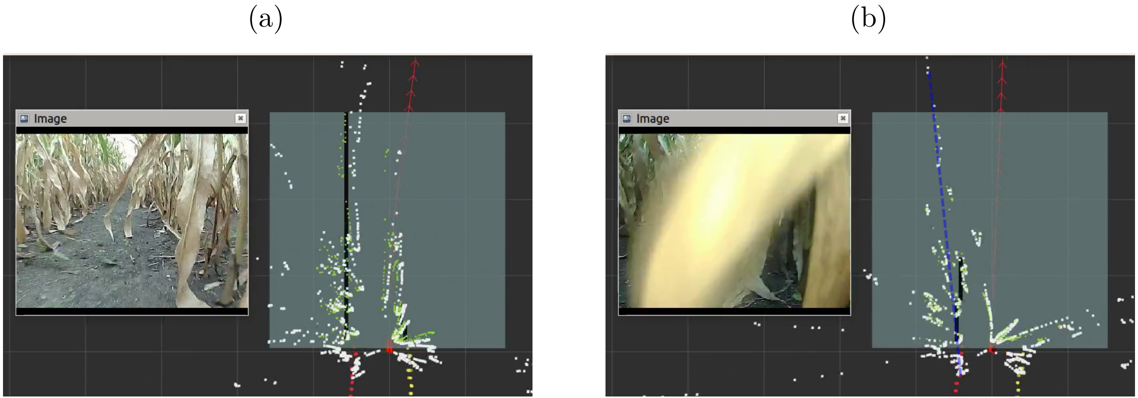

(a) (b)

Source: DASLab database.

robot's one, "the world moves around it". The white points show the raw LiDAR readings, the black lines show current fitted lines and red/yellow points show the last 200 lateral distance estimates for left and right sides, respectively. The thick light green line shows the part of the path that robot should be currently following. There are lane changes for 20s, 38s, 01min13s, 01min50s, 02min10s and 02min43s. All collisions happened in the transitions.

Figure 52 – Third collision. (a) Fallen plant in front of robot. (b)

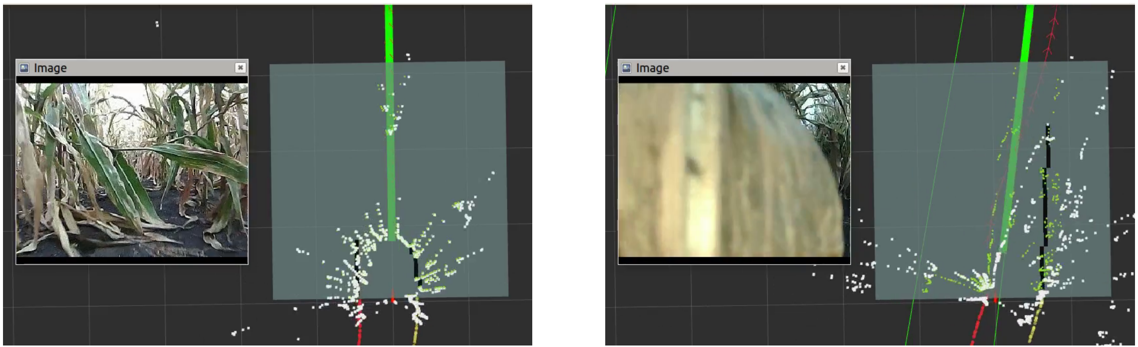
(a)

(b)

Source: DASLab database.

Two of the three trials of serpentine path are displayed by Fig. 53. Figure 53a shows what happens when GNSS measurements lose the RTK corrections: the EKF for localization, which uses the GNSS readings, diverges significantly from where it should be and although two collisions happened (around 0.4 and 0.8), the robot was always within a 0.8 m width lane. Besides these two collisions, the other three collisions also occurred in this type of path and they are depicted by the visible discontinuities on the lime green line (0.5/0.6/1 in Fig. 53b).

Figure 53 – Two of the serpentine path trials.

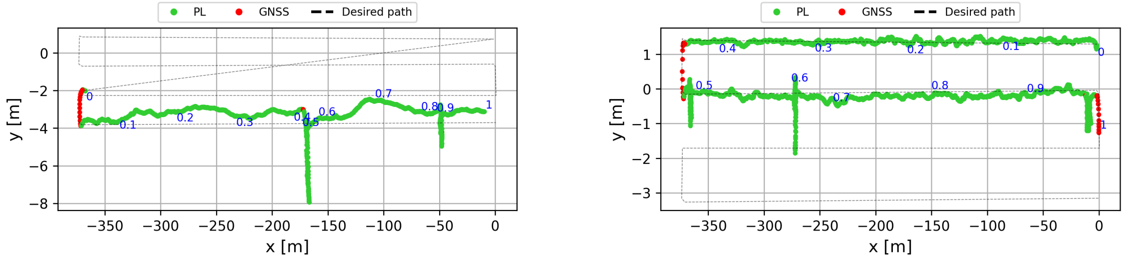
(a)

(b)

Source: DASLab database.

All five collisions in the serpentine path trials were caused by a complete occlusion either because of leaves in the middle of the lane and at LiDAR's reading plane (Figs. 54a, 54b, 54d and 54e) or a fallen plant (Fig. 54c). All of them leads to the heading estimation problem discussed on Sec. 4.4.1.2 and because of that, there was a not negligible time period between occlusion end and returning to track rows. For example, in Fig. 54c situation, this time was around one second and given the robot's speed of 0.7 m/s, it was already too late to avoid collision.

A ROS rviz recording[11] is provided for the longest experiment with serpentine path. Its general description follows the one provided for the longest path in Autonomous Farm. It completed three lanes without collisions while inside. It is sped up 10x due to original

---

[11] <https://youtu.be/ggrvRn7TSs0>

Figure 54 – Collisions in the serpentine path.

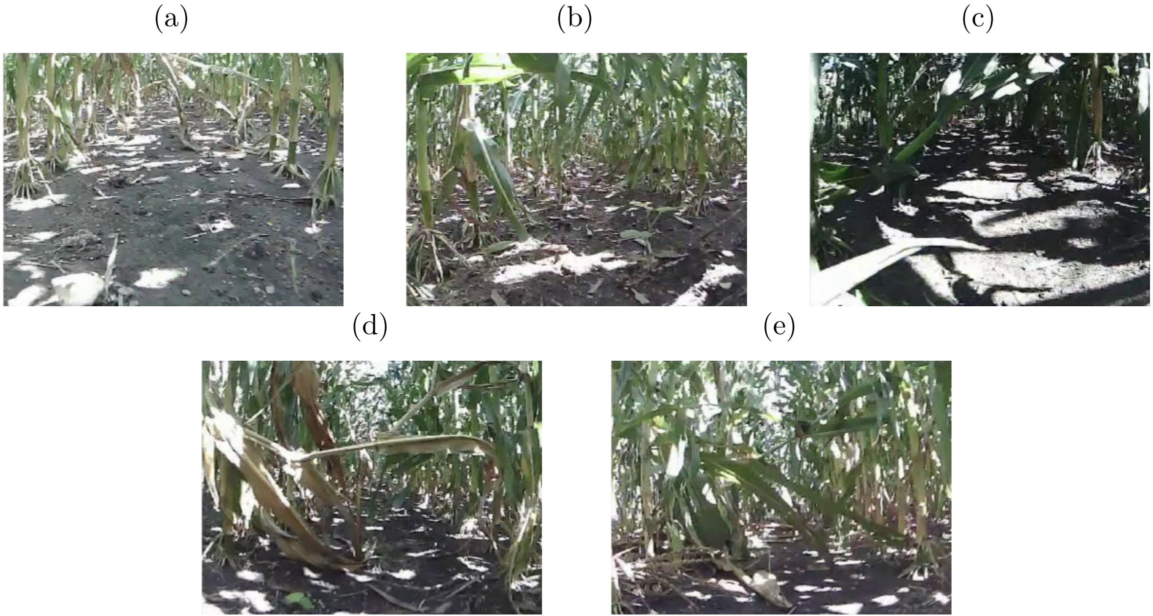

Source: DASLab database.

duration being over 30 minutes. There is a long section without right row around 50 s. Note that right side estimates still exists. The lane switching happens at 1min04s, 2min14s, Note that around 01min38s the global positioning estimates start to drift off due to GNSS bad measurements and the robot is far from the waypoints it should be following. Such drift seems to be corrected after robot changes lane but appears again around 2min48s. Because of this problem, the robot could not go correctly to last lane. Also note the tractor wheel tracks for first and third lanes. They made robot to be significantly tilted and bumping.

5 CONCLUSIONS AND FUTURE WORKS

This study has successfully developed a LiDAR-based Perception Subsystem to estimate lateral distance to rows within narrow lane crop fields such as corn and sorghum. Extensive field testing under multiple conditions and robots has shown around 90% success rate (within 6.6 km of autonomous tests - Sec. 4.2) to reach the end point of continuous corn and sorghum lanes. In total, it has reached 72 km of autonomous navigation using either ***PL*** or ***PL+EKF*** during the study's period.

The remaining field tests (Sec. 4.4) show that EKF improves the lateral estimations, smoothing it out and avoiding common discontinuities when occlusions occur. Nonetheless, occlusions remain a challenge especially in sparser/less well-cared crops and when parallelism between rows is not satisfied. Additionally, gaps of 0.5 m to 1 m are usual in research farms and they provide a challenging situation for the current ***PL+EKF*** due to effect of end of lane from previous segment and variety of entrance conditions on next segment. Indeed, gaps were the major failure reason in Sec. 4.4. Section 4.5 corroborate with ***PL+EKF*** performance as few collisions happened within crop rows.

An interesting future work is to take advantage of on-board camera to estimate field parameters as the row spacing, the stalk width (subsequently the required bin size) and ROI limits as such estimations do not require robot to be moving, therefore, in the beginning of the whole scouting process, they can take as long as needed to improve accuracy. With this and by using ***PL+EKF***, no user-defined parameter would be required anymore.

Reported works in the literature often require an offline pre-mapping stage due to computational power constraints. Such task, which may be manually done, also needs to be constantly updated since crops as corn and sorghum rapidly grow and do not possess a slow time-changing feature as trunks in orchards. Given the performance of the presented ***PL*** and ***PL+EKF***, there is no actual need to map inside rows in the first trip to field. However, a map may be useful when the robot leaves the lane. In this aspect, ***PL+EKF*** greatly reduces operators field work since they will need to manually drive the robot only for occasional situations within crop and for headlands. Section 4.5 showed some initial attempts to autonomously perform the out-crop activities using RTK-GNSS measurements.

The analysis of the field failures show that they mostly happen when a best line cannot be extracted from LiDAR data. This highlights that although significant research focus on improving line extraction with the cost of higher computational costs, the narrow lane crop case requires more investigation on classification. Indeed, an useful immediate step is a classification stage for the LiDAR scan, whether it is usable or not for ***PL***, and going even further, a classification of the points that pertain to the stalks, and not leaves or other clutter. This is supported by the experimental tests with MLSS, which provided cleaner inputs to ***PL*** and performed better under occlusion.

A suitable future work lies in the realm of learning techniques where robot should consciously identify that it ran into an intervention situation and by doing so, it should also learn how to get out of such situation and back to the scouting. This will greatly reduce the intervention rate, thus making the technology more appealing to general public.

In summary, this thesis contributes with a gap filling research on narrow lane crop fields. It also brings a set of user-defined, geometric and temporal constraints to make the solution feasible with low computational power. The later stages, when crops are higher and their height preclude the use of conventional tractors unless harvest is the goal, have remained uncharted for long and interaction with small robots was unknown. Therefore, the field tests highlighted the challenges ahead, i.e. occlusion, lane entrance and gaps, with contextual information of the behavior from a small robot in such situations.

As discussed for mapping, ***PL*** or ***PL+EKF*** are likely to be lower level blocks in more complex autonomous systems yet to be developed to solve the complete autonomy challenge in agricultural fields. A true autonomous robot in agriculture removes the human component, which enables new ways of doing agriculture, such as the concept of swarm, and meet the 2050 agricultural demands with sustainability.

BIBLIOGRAPHY

ABDU, M. A.; BATISTA, I. S.; CARRASCO, A. J.; BRUM, C. G. South Atlantic magnetic anomaly ionization: A review and a new focus on electrodynamic effects in the equatorial ionosphere. **Journal of Atmospheric and Solar-Terrestrial Physics**, v. 67, n. 17-18 SPEC. ISS., p. 1643–1657, 2005. ISSN 13646826.

ABIDINE, A. Z.; HEIDMAN, B. C.; UPADHYAYA, S. K.; HILLS, D. J. Autoguidance system operated at high speed causes almost no tomato damage. **California Agriculture**, v. 58, n. 1, p. 44–47, 2004. ISSN 0008-0845.

AGUIAR, A. S.; SANTOS, F. N. D.; CUNHA, J. B.; SOBREIRA, H.; SOUSA, A. J. Localization and mapping for robots in agriculture and forestry: A survey. **Robotics**, v. 9, n. 4, p. 1–23, 2020. ISSN 22186581.

AMANN, M.-C.; BOSCH, T.; MYLLYLA, R.; RIOUX, M. Laser ranging: a critical review of usual techniques for distance measurement. **Optical Engineering**, [S.I], v. 40, n. 1, p. 10, 2001. ISSN 0091-3286. Disponível em: <http://opticalengineering.spiedigitallibrary.org/article.aspx?doi=10.1117/1.1330700>.

ANDREW, F. W. **Automatic Tractor Control**. US Patent and Trademark Office, 1941. 3 p. Disponível em: <https://patentimages.storage.googleapis.com/a5/3f/ad/dd59d989619911/US2259193.pdf>.

ASTOLFI, P.; GABRIELLI, A.; BASCETTA, L.; MATTEUCCI, M. Vineyard Autonomous Navigation in the Echord++ GRAPE Experiment. **IFAC-PapersOnLine**, Elsevier B.V., v. 51, n. 11, p. 704–709, 2018. ISSN 24058963. Disponível em: <https://doi.org/10.1016/j.ifacol.2018.08.401>.

ÅSTRAND, B.; BAERVELDT, A. J. A vision based row-following system for agricultural field machinery. **Mechatronics**, v. 15, n. 2, p. 251–269, 2005. ISSN 09574158.

BAK, T.; JAKOBSEN, H. Agricultural Robotic Platform with Four Wheel Steering for Weed Detection. **Biosystems Engineering**, [S.I], v. 87, n. 2, p. 125–136, 2004.

BAKKER, T.; ASSELT, K. van; BONTSEMA, J.; MÜLLER, J.; STRATEN, G. van. Autonomous navigation using a robot platform in a sugar beet field. **Biosystems Engineering**, v. 109, n. 4, p. 357–368, 2011. ISSN 15375110.

BAKKER, T.; WOUTERS, H.; ASSELT, K. van; BONTSEMA, J.; TANG, L.; MÜLLER, J.; STRATEN, G. van. A vision based row detection system for sugar beet. **Computers and Electronics in Agriculture**, v. 60, n. 1, p. 87–95, 2008. ISSN 01681699.

BALDWIN, I.; NEWMAN, P. Road vehicle localization with 2D push-broom LIDAR and 3D priors. In: **2012 IEEE International Conference on Robotics and Automation**. IEEE, 2012. p. 2611–2617. ISBN 978-1-4673-1405-3. Disponível em: <http://ieeexplore.ieee.org/document/6224996/>.

BARAWID, O. C.; MIZUSHIMA, A.; ISHII, K.; NOGUCHI, N. Development of an Autonomous Navigation System using a Two-dimensional Laser Scanner in an Orchard Application. **Biosystems Engineering**, v. 96, n. 2, p. 139–149, 2007. ISSN 15375110.

BECHAR, A. Robotics in horticultural field production. **Stewart Postharvest Review**, v. 6, n. 3, p. 1–11, 2010. ISSN 17459656.

BECHAR, A.; VIGNEAULT, C. Agricultural robots for field operations: Concepts and components. **Biosystems Engineering**, [S.I], v. 149, p. 94–111, 2016. ISSN 15375110.

BELL, J.; MACDONALD, B. A.; AHN, H. S. Row following in pergola structured orchards. In: **2016 IEEE/RSJ International Conference on Intelligent Robots and Systems (IROS)**. Daejeon, South Korea: IEEE, 2016. p. 640–645. ISBN 978-1-5090-3762-9. Disponível em: <http://ieeexplore.ieee.org/document/7759120/>.

BELL, T. Automatic tractor guidance using carrier-phase differential GPS. **Computers and Electronics in Agriculture**, v. 25, n. 1-2, p. 53–66, 2000. ISSN 01681699.

BERGERMAN, M.; MAETA, S. M.; ZHANG, J.; FREITAS, G. M.; HAMNER, B.; SINGH, S.; KANTOR, G. Robot Farmers: Autonomous Orchard Vehicles Help Tree Fruit Production. **Robotics & Automation Magazine**, v. 22, n. march, p. 54–63, 2015.

BLACKMORE, S. Towards robotic agriculture. **Autonomous Air and Ground Sensing Systems for Agricultural Optimization and Phenotyping**, v. 9866, n. June 2016, p. 986603, 2016. ISSN 1996756X.

BLACKMORE, S.; GRIEPENTROG, H. W.; NIELSEN, H.; NORREMARK, M.; RESTING-JEPPESEN, J. Development of a deterministic autonomous tractor. **CIGR International conference**, n. May 2014, p. 6, 2004.

BONGIOVANNI, R.; LOWENBERG-DEBOER, J. Precision agriculture and sustainability. **Precision Agriculture**, v. 5, n. 4, p. 359–387, 2004. ISSN 13852256.

CHAWADE, A.; HAM, J. V.; BLOMQUIST, H.; BAGGE, O.; ALEXANDERSSON, E.; ORTIZ, R. High-throughput field-phenotyping tools for plant breeding and precision agriculture. **Agronomy**, v. 9, n. 5, p. 1–18, 2019. ISSN 20734395.

CHEEIN, F. A.; STEINER, G.; PAINA, G. P.; CARELLI, R. Optimized EIF-SLAM algorithm for precision agriculture mapping based on stems detection. **Computers and Electronics in Agriculture**, Elsevier B.V., v. 78, n. 2, p. 195–207, 2011. ISSN 0168-1699. Disponível em: <http://dx.doi.org/10.1016/j.compag.2011.07.007>.

CHOUDHURI, A.; CHOWDHARY, G. Crop stem width estimation in highly cluttered field environment. **Proceedings of the Computer Vision Problems in Plant Phenotyping (CVPPP 2018), Newcastle, UK**, p. 6–13, 2018.

CHRISTIANSEN, M. P. **Localization in orchards: Using Extended Kalman Filter for sensor-fusion**. 2011. 94 p. Tese (Doutorado) — University of Southern Denmark (SDU), 2011.

Department of Economic and Social Affairs of the United Nations. **World population prospects: The 2015 Revision, Key Findings and Advance Tables**. Cambridge University Press, 2015. 66 p. ISSN 1098-6596. ISBN 9788578110796. Disponível em: <http://www.ncbi.nlm.nih.gov/pubmed/21798940>.

DØRUM, J. **Autonomous Navigation And Row Detection in Crop Fields Using Computer Vision**. 2015. Tese (Doutorado) — Norwegian University of Science and Technology, 2015.

DURRANT-WHYTE, H.; BAILEY, T. Simultaneous localization and mapping: part I. **IEEE Robotics & Automation Magazine**, v. 13, n. 2, p. 99–110, 6 2006. ISSN 1070-9932. Disponível em: <http://ieeexplore.ieee.org/document/1638022/>.

ENGLISH, A.; ROSS, P.; BALL, D.; CORKE, P. Vision based guidance for robot navigation in agriculture. In: **2014 IEEE International Conference on Robotics and Automation (ICRA)**. Hong Kong: IEEE, 2014. p. 1693–1698. ISBN 978-1-4799-3685-4. ISSN 10504729. Disponível em: <http://ieeexplore.ieee.org/document/6907079/>.

FAHLGREN, N.; GEHAN, M. A.; BAXTER, I. Lights, camera, action: high-throughput plant phenotyping is ready for a close-up. **Current Opinion in Plant Biology**, Elsevier Ltd, v. 24, p. 93–99, 4 2015. ISSN 13695266. Disponível em: <http://dx.doi.org/10.1016/j.pbi.2015.02.006http://linkinghub.elsevier.com/retrieve/pii/S1369526615000266>.

FAO. **The state of food and agriculture, 1974.** London: Earthscan, 1975. v. 2. 313–4 p. ISSN 0140-6736. ISBN 9781849713269. Disponível em: <http://www.ncbi.nlm.nih.gov/pubmed/50516>.

FAO; IFAD; WFP. **The State of Food Insecurity in the orld: Meeting the 2015 international hunger targets: taking stock of uneven progress**. [S.l.], 2015. 1–54 p. Disponível em: <http://www.fao.org/3/a4ef2d16-70a7-460a-a9ac-2a65a533269a/i4646e.pdf>.

FARRELL, J. A. **Aided Navigation - GPS with High Rate Sensors**. [S.l.]: McGraw-Hill, 2008. 553 p.

FINGER, R.; SWINTON, S. M.; BENNI, N. E.; WALTER, A. Precision Farming at the Nexus of Agricultural Production and the Environment. **Annual Review of Resource Economics**, v. 11, p. 313–335, 2019. ISSN 19411359.

FOUNTAS, S.; MYLONAS, N.; MALOUNAS, I.; RODIAS, E.; SANTOS, C. H.; PEKKERIET, E. Agricultural Robotics for Field Operations. **Sensors**, Elsevier, v. 20, n. 9, p. 2672, 5 2020. ISSN 1424-8220. Disponível em: <https://www.mdpi.com/1424-8220/20/9/2672>.

FURBANK, R. T.; TESTER, M. Phenomics - technologies to relieve the phenotyping bottleneck. **Trends in Plant Science**, Elsevier Ltd, v. 16, n. 12, p. 635–644, 2011. ISSN 13601385. Disponível em: <http://dx.doi.org/10.1016/j.tplants.2011.09.005>.

GARCÍA-SANTILLÁN, I. D.; MONTALVO, M.; GUERRERO, J. M.; PAJARES, G. Automatic detection of curved and straight crop rows from images in maize fields. **Biosystems Engineering**, v. 156, p. 61–79, 4 2017. ISSN 15375110. Disponível em: <https://linkinghub.elsevier.com/retrieve/pii/S1537511016301106>.

GASPARINO, M. V.; HIGUTI, V. A.; VELASQUEZ, A. E.; BECKER, M. Improved localization in a corn crop row using a rotated laser rangefinder for three-dimensional data acquisition. **Journal of the Brazilian Society of Mechanical Sciences and Engineering**, Springer Berlin Heidelberg, v. 42, n. 11, p. 1–10, 2020. ISSN 18063691. Disponível em: <https://doi.org/10.1007/s40430-020-02673-z>.

GILBERT, N. Case studies: A hard look at GM crops. **Nature**, v. 497, n. 7447, p. 24–26, 2013. ISSN 00280836.

GRIFT, T.; ZHANG, Q.; KONDO, N.; TING, K. A review of automation and robotics for the bio-industry. **Journal of Biomechatronics Engineering**, v. 1, n. 1, p. 37–54, 2008.

GUERRERO, H. B. **Desenvolvimento de um sistema de controle em um robô móvel agrícola em escala reduzida para deslocamento entre fileiras de plantio**. 6 2016. 195 p. Tese (Doutorado) — Universidade de São Paulo, São Carlos, 6 2016. Disponível em: <http://www.teses.usp.br/teses/disponiveis/18/18149/tde-24122016-154205/>.

GUERRERO, J. M.; GUIJARRO, M.; MONTALVO, M.; ROMEO, J.; EMMI, L.; RIBEIRO, A.; PAJARES, G. Automatic expert system based on images for accuracy crop row detection in maize fields. **Expert Systems with Applications**, Elsevier Ltd, v. 40, n. 2, p. 656–664, 2013. ISSN 09574174. Disponível em: <http://dx.doi.org/10.1016/j.eswa.2012.07.073>.

GUERRERO, J. M.; RUZ, J. J.; PAJARES, G. Crop rows and weeds detection in maize fields applying a computer vision system based on geometry. **Computers and Electronics in Agriculture**, Elsevier, v. 142, n. March, p. 461–472, 11 2017. ISSN 01681699. Disponível em: <http://dx.doi.org/10.1016/j.compag.2017.09.028https://linkinghub.elsevier.com/retrieve/pii/S0168169917303940>.

HAGUE, T.; MARCHANT, J. A.; TILLETT, N. D. Ground based sensing systems for autonomous agricultural vehicles. **Computers and Electronics in Agriculture**, v. 25, n. 1-2, p. 11–28, 2000. ISSN 01681699.

HIGUTI, V. A. H.; VELASQUEZ, A. E. B.; MAGALHAES, D. V.; BECKER, M.; CHOWDHARY, G. Under canopy light detection and ranging-based autonomous navigation. **Journal of Field Robotics**, v. 36, n. 3, p. 547–567, 5 2018. ISSN 1556-4959. Disponível em: <https://onlinelibrary.wiley.com/doi/abs/10.1002/rob.21852>.

HIREMATH, S.; EVERT, F. K. van; BRAAK, C. t.; STEIN, A.; HEIJDEN, G. van der. Image-based particle filtering for navigation in a semi-structured agricultural environment. **Biosystems Engineering**, Elsevier Ltd, v. 121, p. 85–95, 5 2014. ISSN 15375110. Disponível em: <http://dx.doi.org/10.1016/j.biosystemseng.2014.02.010http://linkinghub.elsevier.com/retrieve/pii/S1537511014000312>.

HIREMATH, S. A.; HEIJDEN, G. W. A. M. van der; EVERT, F. K. van; STEIN, A.; BRAAK, C. J. F. T. Laser range finder model for autonomous navigation of a robot in a maize field using a particle filter. **Computers and Electronics in Agriculture**, Elsevier B.V., v. 100, p. 41–50, 2014. ISSN 01681699. Disponível em: <http://dx.doi.org/10.1016/j.compag.2013.10.005>.

HUNTER, M. C.; SMITH, R. G.; SCHIPANSKI, M. E.; ATWOOD, L. W.; MORTENSEN, D. A. Agriculture in 2050: Recalibrating targets for sustainable intensification. **BioScience**, v. 67, n. 4, p. 386–391, 2017. ISSN 15253244.

Ji Zhang; CHAMBERS, A.; MAETA, S.; BERGERMAN, M.; SINGH, S. 3D perception for accurate row following: Methodology and results. In: **2013 IEEE/RSJ International Conference on Intelligent Robots and Systems**. Tokyo: IEEE, 2013. p. 5306–5313. ISBN 978-1-4673-6358-7. ISSN 21530858. Disponível em: <http://ieeexplore.ieee.org/document/6697124/>.

JIANG, G.; WANG, Z.; LIU, H. Automatic detection of crop rows based on multi-ROIs. **Expert Systems with Applications**, Elsevier Ltd, v. 42, n. 5, p. 2429–2441, 4 2015. ISSN 09574174. Disponível em: <http://dx.doi.org/10.1016/j.eswa.2014.10.033http://linkinghub.elsevier.com/retrieve/pii/S0957417414006575>.

KALMAN, R. E. A New Approach to Linear Filtering and Prediction Problems. **Journal of Basic Engineering**, v. 82, n. 1, p. 35, 1960. ISSN 00219223. Disponível em: <http://scholar.google.com/scholar?hl=en&btnG=Search&q=intitle:A+New+Approach+to+Linear+Filtering+and+Prediction+Problems#0%5Cnhttp://fluidsengineering.asmedigitalcollection.asme.org/article.aspx?articleid=1430402>.

KAPLAN, E. D.; HEGARTY, C. J. **Understanding GPS. Principles and applications**. 2nd. ed. Norwood: Artech House, 2006. 723 p. ISSN 13646826. ISBN 1580538940.

KIENZLE, J.; ASHBURNER, J. E.; SIMS, B. G. et al. Mechanization for rural development: a review of patterns and progress from around the world. **Integrated Crop Management**, Food and Agriculture Organization of the United Nations (FAO), v. 20, 2013.

KING, A. Technology: The Future of Agriculture. **Nature**, v. 544, n. 7651, p. S21–S23, 4 2017. ISSN 0028-0836. Disponível em: <http://www.nature.com/articles/544S21a>.

KNEIP, L.; TACHE, F.; CAPRARI, G.; SIEGWART, R. Characterization of the compact Hokuyo URG-04LX 2D laser range scanner. In: **2009 IEEE International Conference on Robotics and Automation**. IEEE, 2009. p. 1447–1454. ISBN 978-1-4244-2788-8. ISSN 10504729. Disponível em: <http://ieeexplore.ieee.org/document/5152579/>.

Labecki. Characterization of a Compact Laser Scanner As a Sensor for Legged Mobile Robots. v. 3, n. 3, p. 45–52, 2012.

LEMOS, R. A. d.; NOGUEIRA, L. A. C. d. O.; RIBEIRO, A. M.; MIRISOLA, L. G. B.; Mauro F. Koyama; PAIVA, E. C. d.; BUENO, S. S. UNISENSORY INTRA-ROW NAVIGATION STRATEGY FOR ORCHARDS ENVIRONMENTS BASED ON SENSOR LASER. In: **Congresso Brasileiro de Automática**. [s.n.], 2018. v. 1, n. 1. Disponível em: <http://www.swge.inf.br/proceedings/paper/?P=CBA2018-0400>.

LENAIN, R.; THUILOT, B.; CARIOU, C.; MARTINET, P. Rejection of sliding effects in car like robot control: application to farm vehicle guidance using a single RTK GPS sensor. In: **Proceedings 2003 IEEE/RSJ International Conference on Intelligent Robots and Systems (IROS 2003) (Cat. No.03CH37453)**. IEEE, 2003. v. 3, n. October, p. 3811–3816. ISBN 0-7803-7860-1. Disponível em: <http://ieeexplore.ieee.org/document/1249748/>.

LEPEJ, P.; RAKUN, J. Simultaneous localisation and mapping in a complex field environment. **Biosystems Engineering**, v. 150, p. 160–169, 10 2016. ISSN 15375110. Disponível em: <https://linkinghub.elsevier.com/retrieve/pii/S1537511015302841>.

LEWIS, R.; JOHNSTON, A. A Scanning Laser Rangefinder for a Robotic Vehicle. In: **Proceedings of the Fifth International Joint Conference on Artificial Intelligence (II)**. Cambridge: [s.n.], 1977. p. 762–768.

MALAVAZI, F. B. P.; GUYONNEAU, R.; FASQUEL, J.-b.; LAGRANGE, S. LiDAR-only based navigation algorithm for an autonomous agricultural robot. **Computers and Electronics in Agriculture**, Elsevier, v. 154, n. September, p. 71–79, 2018. ISSN 0168-1699. Disponível em: <https://doi.org/10.1016/j.compag.2018.08.034>.

MARINOUDI, V.; SØRENSEN, C. G.; PEARSON, S.; BOCHTIS, D. Robotics and labour in agriculture. A context consideration. **Biosystems Engineering**, Elsevier Ltd, v. 184, p. 111–121, 2019. ISSN 15375110. Disponível em: <https://doi.org/10.1016/j.biosystemseng.2019.06.013>.

MCCONNELL, M.; LIEFERT, O.; OLSON, D.; CAPEHART, T. **Feed Outlook Strong Global Prices and Foreign Demand Raise Projected Corn Exports**. [S.l.], 2021. 14 p. Disponível em: <https://downloads.usda.library.cornell.edu/usda-esmis/files/44558d29f/6395x159k/2801q936m/FDS-21b.pdf>.

MONTALVO, M.; PAJARES, G.; GUERRERO, J.; ROMEO, J.; GUIJARRO, M.; RIBEIRO, A.; RUZ, J.; CRUZ, J. Automatic detection of crop rows in maize fields with high weeds pressure. **Expert Systems with Applications**, Elsevier Ltd, v. 39, n. 15, p. 11889–11897, 11 2012. ISSN 09574174. Disponível em: <http://dx.doi.org/10.1016/j.eswa.2012.02.117http://linkinghub.elsevier.com/retrieve/pii/S0957417412003806>.

MORIMOTO, E.; SUGURI, M.; UMEDA, M. Vision-based navigation system for autonomous transportation vehicle. **Precision Agriculture**, v. 6, n. 3, p. 239–254, 2005. ISSN 13852256.

MOUSAZADEH, H. A technical review on navigation systems of agricultural autonomous off-road vehicles. **Journal of Terramechanics**, ISTVS, v. 50, n. 3, p. 211–232, 2013. ISSN 00224898. Disponível em: <http://dx.doi.org/10.1016/j.jterra.2013.03.004>.

MUELLER-SIM, T.; JENKINS, M.; ABEL, J.; KANTOR, G. The Robotanist: A ground-based agricultural robot for high-throughput crop phenotyping. In: **2017 IEEE International Conference on Robotics and Automation (ICRA)**. IEEE, 2017. p. 3634–3639. ISBN 978-1-5090-4633-1. ISSN 10504729. Disponível em: <http://ieeexplore.ieee.org/document/7989418/>.

NØRREMARK, M.; GRIEPENTROG, H. W.; NIELSEN, J.; SØGAARD, H. T. The development and assessment of the accuracy of an autonomous GPS-based system for intra-row mechanical weed control in row crops. **Biosystems Engineering**, IAgrE, v. 101, n. 4, p. 396–410, dez. 2008. Disponível em: <https://doi.org/10.1016/j.biosystemseng.2008.09.007>.

OKUBO, Y.; YE, C.; BORENSTEIN, J. Characterization of the Hokuyo URG-04LX laser rangefinder for mobile robot obstacle negotiation. **Proceedings of SPIE**, v. 7332, p. 1–733212, 2009. ISSN 0277786X.

ORTIZ, J. M.; OLIVARES, M. A Vision Based Navigation System for an Agricultural Field Robot. In: **2006 IEEE 3rd Latin American Robotics Symposium**. IEEE, 2006. p. 106–114. ISBN 1-4244-0536-X. Disponível em: <http://ieeexplore.ieee.org/document/4133840/>.

PILARSKI, T.; HAPPOLD, M.; PANGELS, H.; OLLIS, M.; FITZPATRICK, K.; STENTZ, A. The Demeter System for Automated Harvesting. **Autonomous Robots**, v. 13, n. 1,

p. 9–20, 2002. ISSN 09295593. Disponível em: <http://link.springer.com/10.1023/A:1015622020131>.

POULIOT, N.; RICHARD, P.-L.; MONTAMBAULT, S. LineScout power line robot: Characterization of a UTM-30LX LIDAR system for obstacle detection. In: **2012 IEEE/RSJ International Conference on Intelligent Robots and Systems**. IEEE, 2012. p. 4327–4334. ISBN 978-1-4673-1736-8. ISSN 21530858. Disponível em: <http://ieeexplore.ieee.org/document/6385476/>.

RADCLIFFE, J.; COX, J.; BULANON, D. M. Machine vision for orchard navigation. **Computers in Industry**, Elsevier B.V., v. 98, p. 165–171, 6 2018. ISSN 01663615. Disponível em: <https://doi.org/10.1016/j.compind.2018.03.008https://linkinghub.elsevier.com/retrieve/pii/S0166361517305389>.

RAHAMAN, M. M.; CHEN, D.; GILLANI, Z.; KLUKAS, C.; CHEN, M. Advanced phenotyping and phenotype data analysis for the study of plant growth and development. **Frontiers in Plant Science**, v. 6, n. August, p. 1–15, 8 2015. ISSN 1664-462X. Disponível em: <http://journal.frontiersin.org/Article/10.3389/fpls.2015.00619/abstract>.

RAI, M. State of indian agriculture. National Academy of Agricultural Sciences, 2009.

REINA, G.; MILELLA, A.; ROUVEURE, R.; NIELSEN, M.; WORST, R.; BLAS, M. R. Ambient awareness for agricultural robotic vehicles. **Biosystems Engineering**, v. 146, p. 114–132, 6 2016. ISSN 15375110. Disponível em: <http://linkinghub.elsevier.com/retrieve/pii/S1537511015001889https://linkinghub.elsevier.com/retrieve/pii/S1537511015001889>.

RIGGIO, G.; FANTUZZI, C.; SECCHI, C. A Low-Cost Navigation Strategy for Yield Estimation in Vineyards. **Proceedings - IEEE International Conference on Robotics and Automation**, IEEE, p. 2200–2205, 2018. ISSN 10504729.

ROMEO, J.; PAJARES, G.; MONTALVO, M.; GUERRERO, J. M.; GUIJARRO, M.; RIBEIRO, A. Crop row detection in maize fields inspired on the human visual perception. **The Scientific World Journal**, v. 2012, 2012. ISSN 1537744X.

ROVIRA-MÁS, F.; CHATTERJEE, I.; SÁIZ-RUBIO, V. The role of GNSS in the navigation strategies of cost-effective agricultural robots. **Computers and Electronics in Agriculture**, Elsevier B.V., v. 112, p. 172–183, 3 2015. ISSN 01681699. Disponível em: <http://dx.doi.org/10.1016/j.compag.2014.12.017http://linkinghub.elsevier.com/retrieve/pii/S0168169914003275>.

SANTOS, F. B. N. d.; SOBREIRA, H. M. P.; CAMPOS, D. F. B.; SANTOS, R. M. P. M. d.; MOREIRA, A. P. G. M.; CONTENTE, O. M. S. Towards a Reliable Monitoring Robot for Mountain Vineyards. In: **2015 IEEE International Conference on Autonomous Robot Systems and Competitions**. Vila Real: IEEE, 2015. p. 37–43. ISBN 978-1-4673-6991-6. ISSN 15730409. Disponível em: <http://ieeexplore.ieee.org/lpdocs/epic03/wrapper.htm?arnumber=7101608http://ieeexplore.ieee.org/document/7101608/>.

SHALAL, N.; LOW, T.; MCCARTHY, C.; HANCOCK, N. Orchard mapping and mobile robot localisation using on-board camera and laser scanner data fusion - Part B: Mapping and localisation. **Computers and Electronics in Agriculture**, Elsevier B.V., v. 119, p. 267–278, 2015. ISSN 01681699.

SHAMSHIRI, R. R.; WELTZIEN, C.; HAMEED, I. A.; YULE, I. J.; GRIFT, T. E.; BALASUNDRAM, S. K.; PITONAKOVA, L.; AHMAD, D.; CHOWDHARY, G. Research and development in agricultural robotics: A perspective of digital farming. **International Journal of Agricultural and Biological Engineering**, v. 11, n. 4, p. 1–11, 2018. ISSN 1934-6344.

SIEGWART, R.; NOURBAKHSH, I. R.; SCARAMUZZA, D. **Introduction to autonomous mobile robots**. [S.l.]: MIT press, 2011.

SPOGLI, L.; ALFONSI, L.; ROMANO, V.; FRANCESCHI, G. D.; FRANCISCO, G. M. J.; SHIMABUKURO, M. H.; BOUGARD, B.; AQUINO, M. Assessing the GNSS scintillation climate over Brazil under increasing solar activity. **Journal of Atmospheric and Solar-Terrestrial Physics**, v. 105-106, p. 199–206, 2013. ISSN 13646826.

STOLL, A.; KUTZBACH, H. D. Guidance of a forage harvester with GPS. **Precision Agriculture**, v. 2, n. 3, p. 281–291, 2001. ISSN 13852256.

SUBRAMANIAN, V.; BURKS, T. F.; ARROYO, A. A. Development of machine vision and laser radar based autonomous vehicle guidance systems for citrus grove navigation. **Computers and Electronics in Agriculture**, v. 53, n. 2, p. 130–143, 2006. ISSN 01681699.

SUPREM, A.; MAHALIK, N.; KIM, K. A review on application of technology systems, standards and interfaces for agriculture and food sector. **Computer Standards & Interfaces**, Elsevier B.V., v. 35, n. 4, p. 355–364, 2013. ISSN 09205489. Disponível em: <http://dx.doi.org/10.1016/j.csi.2012.09.002>.

TAROKH, M.; HO, H. D.; BOULOUBASIS, A. Systematic kinematics analysis and balance control of high mobility rovers over rough terrain. **Robotics and Autonomous Systems**, North-Holland, v. 61, n. 1, p. 13–24, 1 2013. ISSN 0921-8890. Disponível em: <https://www.sciencedirect.com/science/article/pii/S0921889012001649>.

THUILOT, B.; CARIOU, C.; MARTINET, P.; BERDUCAT, M. Automatic guidance of a farm tractor relying on a single CP-DGPS. **Autonomous Robots**, v. 13, n. 1, p. 53–71, 2002. ISSN 09295593.

TILLETT, N. D.; HAGUE, T.; MARCHANT, J. A. A robotic system for plant-scale husbandry. **Journal of Agricultural and Engineering Research**, v. 69, n. 2, p. 169–178, 1998. ISSN 00218634.

TORGERSEN, J. **Mobile Agricultural Robot Independent Four Wheel Ackerman Steering**. 2014. Tese (Doutorado) — Norwegian University of Life Sciences, 2014.

TROYER, T. A.; PITLA, S.; NUTTER, E. Inter-row Robot Navigation using 1D Ranging Sensors. **IFAC-PapersOnLine**, Elsevier B.V., v. 49, n. 16, p. 463–468, 2016. ISSN 24058963. Disponível em: <http://dx.doi.org/10.1016/j.ifacol.2016.10.084https://linkinghub.elsevier.com/retrieve/pii/S2405896316316470>.

United Nations DESA. **World Population Prospects 2019**. [S.l.], 2019. 49–78 p. Disponível em: <http://www.ncbi.nlm.nih.gov/pubmed/12283219>.

U.S. Department of Agriculture. **2020 International Long-Term Projections to 2029**. [S.l.], 2020. Disponível em: <https://www.ers.usda.gov/webdocs/DataFiles/51280/2020InternationalLong-TermProjectionsto2029.xlsx?v=8049>.

USA Department Of Defense. **Global Positioning System Standard Positioning Service**. 2008. 1 - 160 p. Disponível em: <http://www.gps.gov/technical/ps/2008-SPS-performance-standard.pdf>.

VELASQUEZ, A. E.; HIGUTI, V. A.; GUERRERO, H. B.; GASPARINO, M. V.; MAGALHÃES, D. V.; AROCA, R. V.; BECKER, M. Reactive navigation system based on H∞ control system and LiDAR readings on corn crops. **Precision Agriculture**, Springer US, n. 0123456789, 2019. ISSN 15731618. Disponível em: <https://doi.org/10.1007/s11119-019-09672-8>.

VELASQUEZ, A. E. B. **helvis III – Desenvolvimento e Caracterização da Plataforma Robótica**. 2015. 162 p. Tese (Doutorado) — University of São Paulo, 2015.

VELASQUEZ, A. E. B.; HIGUTI, V. A. H.; GUERRERO, H. B.; MILORI, D. M. B. P.; MAGALHAES, D. V.; BECKER, M. Helvis - a Small-Scale Agricultural Mobile Robot Prototype for Precision Agriculture. In: **13th International Conference of Precision Agriculture**. St. Louis: International Society of Precision Agriculture, 2016. p. 17.

VIDONI, R.; BIETRESATO, M.; GASPARETTO, A.; MAZZETTO, F. Evaluation and stability comparison of different vehicle configurations for robotic agricultural operations on side-slopes. **Biosystems Engineering**, Elsevier Ltd, v. 129, p. 197–211, 2015. ISSN 15375110. Disponível em: <http://dx.doi.org/10.1016/j.biosystemseng.2014.10.003>.

VIDOVIC, I.; CUPEC, R.; HOCENSKI, Z. Crop row detection by global energy minimization. **Pattern Recognition**, v. 55, p. 68–86, 2016. ISSN 00313203.

WANG, H.; NOGUCHI, N. Autonomous maneuvers of a robotic tractor for farming. In: **2016 IEEE/SICE International Symposium on System Integration (SII)**. Sapporo: IEEE, 2016. p. 592–597. ISBN 978-1-5090-3329-4. Disponível em: <http://ieeexplore.ieee.org/document/7844063/>.

WILLRODT, F. L. **Steering Attachment for Tractors**. 1924. 6 p.

XAUD, M. F.; LEITE, A. C.; FROM, P. J. Thermal image based navigation system for skid-steering mobile robots in sugarcane crops. **Proceedings - IEEE International Conference on Robotics and Automation**, v. 2019-May, p. 1808–1814, 2019. ISSN 10504729.

XUE, J.; ZHANG, L.; GRIFT, T. E. Variable field-of-view machine vision based row guidance of an agricultural robot. **Computers and Electronics in Agriculture**, Elsevier B.V., v. 84, p. 85–91, 2012. ISSN 01681699. Disponível em: <http://dx.doi.org/10.1016/j.compag.2012.02.009>.

YAN, W.; WANG, L.; JIN, Y.; SHI, G. High accuracy Navigation System using GPS and INS system integration strategy. In: **2016 IEEE International Conference on Cyber Technology in Automation, Control, and Intelligent Systems (CYBER)**. IEEE, 2016. p. 365–369. ISBN 978-1-5090-2733-0. Disponível em: <http://ieeexplore.ieee.org/document/7574851/>.

YOUNG, S. N.; KAYACAN, E.; PESCHEL, J. M. Design and field evaluation of a ground robot for high-throughput phenotyping of energy sorghum. **Precision Agriculture**, Springer US, v. 20, n. 4, p. 697–722, 2019. ISSN 15731618. Disponível em: <https://doi.org/10.1007/s11119-018-9601-6>.

ZHAI, Z.; ZHU, Z.; DU, Y.; SONG, Z.; MAO, E. Multi-crop-row detection algorithm based on binocular vision. **Biosystems Engineering**, Elsevier Ltd, v. 150, p. 89–103, 2016. ISSN 15375110. Disponível em: <http://dx.doi.org/10.1016/j.biosystemseng.2016.07.009>.

ZHANG, C.; NOGUCHI, N.; YANG, L. Leader–follower system using two robot tractors to improve work efficiency. **Computers and Electronics in Agriculture**, Elsevier B.V., v. 121, p. 269–281, 2 2016. ISSN 01681699. Disponível em: <http://dx.doi.org/10.1016/j.compag.2015.12.015https://linkinghub.elsevier.com/retrieve/pii/S016816991500397X>.

ZHANG, S.; WANG, Y.; ZHU, Z.; LI, Z.; DU, Y.; MAO, E. Tractor path tracking control based on binocular vision. **Information Processing in Agriculture**, China Agricultural University, v. 5, n. 4, p. 422–432, 12 2018. ISSN 22143173. Disponível em: <https://doi.org/10.1016/j.inpa.2018.07.003https://linkinghub.elsevier.com/retrieve/pii/S2214317318300787>.

ZHAO, S.; ZHANG, Z. A new recognition of crop row based on its structural parameter model. **IFAC-PapersOnLine**, Elsevier B.V., v. 49, n. 16, p. 431–438, 2016. ISSN 24058963. Disponível em: <http://dx.doi.org/10.1016/j.ifacol.2016.10.079https://linkinghub.elsevier.com/retrieve/pii/S2405896316316421>.

Appendix

APPENDIX A – 2D LIDAR

A.1 Basic Principle

The basic principle of a laser rangefinder device is the projection of a light wave onto an object and subsequent processing of reflected or scattered wave to determine distance. They are often referred to as optical radar or LiDAR.

Several principles are used in such devices. A very common one is time-of-flight (TOF), which is explained as it is used in the distance sensor SICK LMS 200, considered de-facto standard in robotics community until mid-2000s (OKUBO, 2009). In addition, Amplitude Modulated Continuous Wave (AMCW) is explained as it is the working principle for Hokuyo sensors, subjects of characterization in this work.

A.1.1 Time-of-Flight (TOF)

Time-of-flight distance measuring technique refers to the transmission of a pulse of energy which will be reflected when it encounters an object and a time t_d, which is the time needed for the signal to be transmitted and to return to the receiver, can be measured. Thus, distance d to the observed object can be calculated based on the propagation speed of light ($c = 3 \cdot 10^8 \mathrm{m/s}$) using Eq. A.1

$$d = c \cdot t_d/2 \tag{A.1}$$

It is important to notice that the measured time t_d corresponds to traveling the distance twice, hence only half of t_d should be used to obtain distance to target. In order to obtain 1mm accuracy, time interval measurement requires electronics capable of 6.7ps accuracy (AMANN, 2001).

Also according to Amann, Bosch, Myllyla and Rioux (2001), final precision of distance measurement can be greatly improved by averaging. This improvement is proportional to the square root of the number of results averaged.

A.1.2 Amplitude Modulated Continuous Wave (AMCW)

AMCW ranging technique obtains distance measurements to a target by measuring phase-shifts. As it can be seen in Fig. 55, the laser block emits a beam and its direction is changed by a rotating mirror. After hitting the surface of the object, the laser is reflected and returns to sensor. Then its direction is again changed by a rotating mirror, and captured by an Avalanche Photodiode (APD). Finally, on board electronics is responsible to measure the phase difference ϕ_d between the emitted wave of laser light and a fraction of this wave reflected by target surface back to the sensor. Then, distance traveled d_{PS} when the modulated frequency of emitted signal is ω_{sig} is given by

$$d_{PS} = \frac{c \cdot \phi_d}{2\omega_{sig}} \tag{A.2}$$

Figure 55 – Working principle of Hokuyo laser rangefinder.

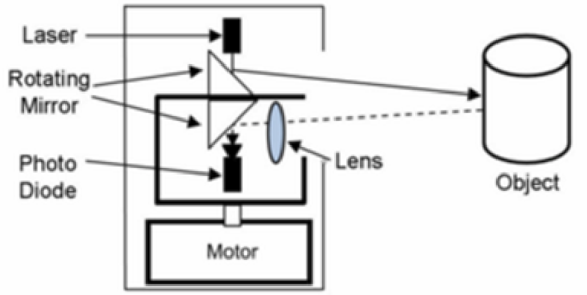

Source: Okubo, Ye and Borenstein (2009)

A.2 LiDAR Assessment

A.2.1 Common Analyzed Effects

Okubo, Ye and Borenstein (2009) addressed possible effects on sensor performance such as drift and surface properties. In addition, sensor spatial orientation is also tested by Pouliot, Richard and Montambault (2012), Kneip, Tache, Caprari and Siegwart (2009). Due to heat dissipation of the spindle motor, from completely turned off condition until temperature equilibrium, there is a continuous increase in sensor's operating temperature. This may lead to drift effects while the sensor is not completely "warmed-up". In summary, Okubo, Ye and Borenstein (2009) found out that target surface reflectivity significantly influences both mean value and the distribution of the measured distances, while surface color and gray levels do not significantly influence those quantities. Sensor spatial orientation analysis was crucial to Pouliot, Richard and Montambault (2012) as the mobile robot which carries the sensor is subject to lateral winds and other tridimensional maneuvers to overcome obstacles, thus sensor would be out of standard standing position. While the orientation did not present significant effect on UTM-30LX (POULIOT, 2012), it certainly affected URG-04LX (KNEIP, 2009).

A.2.2 Experimental setup

The device URG-04LX NO: H1207998C has a scan rate of around 10Hz. Moreover, a range of 240 is covered by the rotating mirror with an angular resolution of 0.352°, resulting in 683 distance readings. The size of the sensor is 50x50x70 mm and it weighs only 160g. The beam source is a near-infrared (785nm) laser diode and according to Kneip, Tache, Caprari and Siegwart (2009), two modulation frequencies allow measurements between 0.02m and 5.6m. However, actual maximum range is up to 4m for most of surface types (Labecki, 2012).

The second one is UTM-30LX NO: H1210401B with a 40 Hz scan rate. A wider range of 270°is covered with an angular resolution of 0.25°, resulting in 1080 distance readings. Sensor's envelope is 60x60x87mm and it weighs 210g. The beam source is a 905nm laser diode and as principle is similar to URG-04LX, two modulation frequencies may also be used, allowing measurements between 0.1m and 30m. However, in outdoor conditions, actual maximum range is around 20m in a bright day (VELASQUEZ, 2015).

A null reference cannot be obtained from physical marks on sensors nor from specification sheet. As Kneip, Tache, Caprari and Siegwart (2009) states, this missing knowledge hinders determination of nominal distance. For this work, null reference is considered to be at the geometrical center of each sensor.

Setup consists of both Hokuyo sensors positioned on a wood table and white paper sheet as target. Using a Starrett TS34-5M measuring tape, the front plane of both sensors are positioned 1.000±0.001 m from target. As previously stated, sensor's geometrical center is considered null reference, therefore it is expected that measured distances are about 1.025m for URG-04LX and 1.030m for UTM-30LX.

As warm-up time may not be often possible for mobile robotics applications, all measurements started right after devices were powered up and continued for a standard time of 6000 seconds. Therefore, each measurement acquisition happened at least after a couple of hours with the system completely turned off.

First, distance measurements were taken with sensors positioned in conventional orientation as it can be seen in Fig. 56a. It can be noted that UTM-30LX is tested without an aluminium plate of 0.2x0.2x0.002m as heatsink, which is advised by manufacturer. This way, the sensor performance can be assessed as it has been used (embedded in the robot without any heatsink).

A second set is obtained with an aluminium plate under UTM-30LX, thus acting as heatsink. Finally, the acquisition is repeated but with both sensors in upside-down orientation, as it can be seen in Fig. 56b. It is important to state that UTM-30LX was tested with heatsink.

Both sensors are connected to a laptop running Ubuntu 14.04.3 LTS through full-speed USB 2.0. Using URG Network Library , a C++ routine is responsible for establishing communication with devices, retrieving two vectors: one with measured distances and another with intensities, and saving it to a text file.

Generated text files are then imported to Matlab environment, and time-series, histograms and boxplots are plotted for analysis purpose. For this characterization, only

Figure 56 – Experiment setup arranged to acquire fixed distance measurements for 6000 seconds. (a) Sensors are positioned in conventional orientation. (b) Sensors are positioned in upside-down orientation.

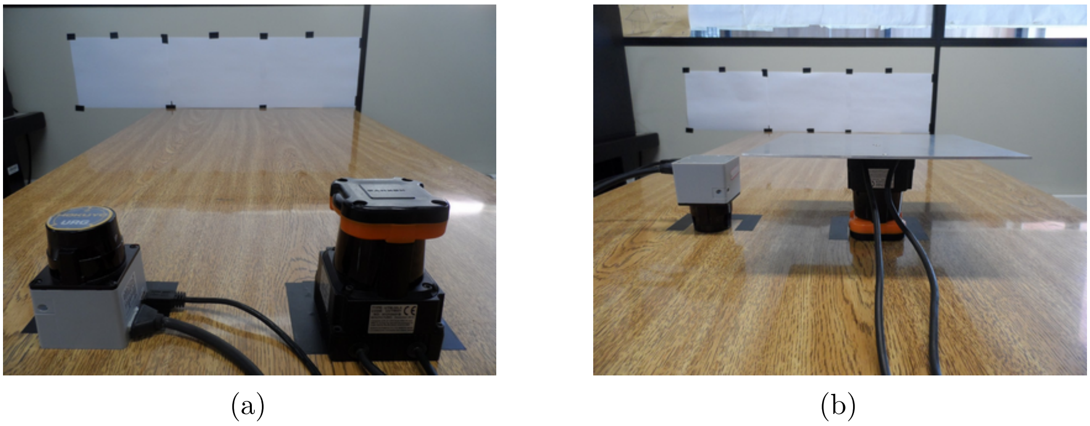
(a) (b)

Source: author.

steps 342 and 541 from URG-04LX and UTM-30LX respective vectors are used. Such steps were chosen as they are likely to contain each sensor's central beam measurement.

A.3 2D LiDAR characterization

Figure 57a and Fig. 57b are relative to first experimental setup, thus both sensors were positioned in conventional orientation. As similar figures would not provide additional information for second experimental setup, they are not displayed. Subsequently, the third experimental setup, the one in which sensors are flipped upside-down, can be described by Fig. 58a and Fig. 58b. Finally, Fig. 59a and Fig. 59b summarize the experiments in the form of boxplots.

As it can be seen in Fig. 57a(i) and Fig. 58a(ii), there is a continuous drop of measured distance over the first 30 minutes (1800 seconds) of operation, as exposed by Okubo, Ye and Borenstein (2009). In addition, although not as prominent as in URG-04LX, sensor UTM-30LX also requires some time to reach steady state, which can be seen by the difference between overall shape before and after the black vertical line in Fig. 57a(ii) and Fig. 58a(ii). This black line marks one hour of operation. Additionally, Fig. 57b and Fig. 58b show histograms of the retrieved data. For any of the studied cases, UTM-30LX presented a normal distribution (subplots (iii) and (iv)). Thus, this hypothesis can be securely used in further perception systems with UTM-30LX. The same cannot be said for URG-04LX, which does not present a coherent data distribution, as it did not assume a common shape when considering warm-up time or orientation. Therefore, a hypothesis of normal distribution for URG-04LX may be used with caution.

The boxplots pictured in Fig. 59a and Fig. 59b summarize key characteristics of the sensors. They were plotted from data ignoring the first sixty minutes, hence warm-up

Figure 57 – (a) Measured distance plots for sensors from start-up time until total time of 6000s. The black vertical line marks one hour of operation. (i) URG-04LX (ii) UTM-30LX; (b) Histograms of measured distances (i) URG-04LX for the first 30 minutes (ii) URG-04LX after warmed up (iii) UTM-30LX for the first 30 minutes (iv) UTM-30LX after warmed up.

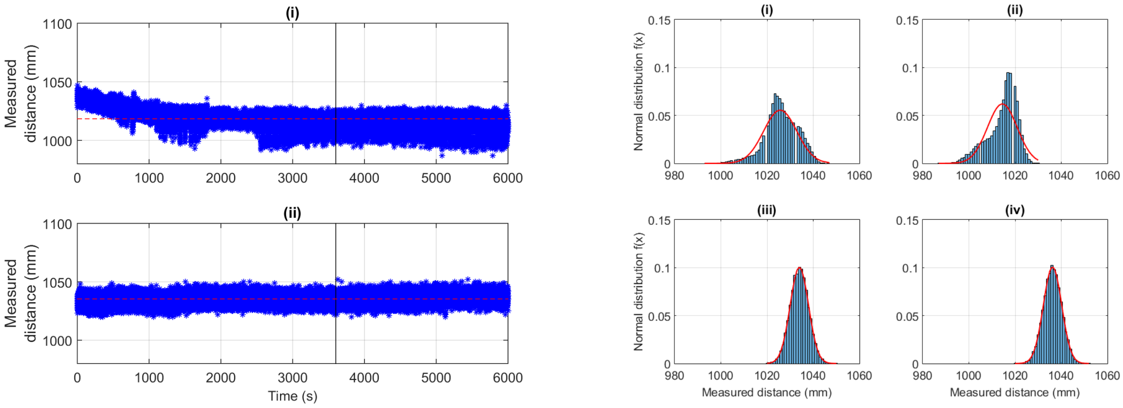

(a) (b)

Source: author.

effect is not present.

First, mean value is lower than expected, hence the null reference is probably few millimeters to the front of geometrical center. It also can be seen the presence of a considerable number of outliers, thus single distance measurement may not be completely reliable. Nevertheless, most of data remains inside a box of 10mm.

Finally, at least with regards to heatsink usage and orientation, robustness of UTM-30LX can be observed as data distribution is basically the same in all cases, as it can be seen in Fig. 59b. The same cannot be stated for URG-04LX, which showed visible changes only considering orientation (Fig. 59a).

A.3.1 Final remarks

LiDAR has been used to capture a horizontal scan of the surroundings. Angled LiDAR scans can be suitably treated to form a 3-D point cloud with similar procedures as MLSS (GASPARINO, 2020). Therefore, to understand the performance changes that will happen due to the change of LiDAR's orientation, the device was characterized in the standard orientation and an extreme case where the sensor was placed upside-down. Moreover, the influence of a heatsink suggested by manufacturer was also evaluated.

The characterization provided a good impression on the measured distance statistical distribution, supporting the usual hypothesis of normal distribution in perception systems based on LiDAR sensors. Moreover, manufacturer's suggestion of an aluminum plate as heatsink for UTM-30LX is probably related to extending its life-span as it does

Figure 58 – (a) Measured distance plots for upside-down sensors from start-up time until total time of 6000s. The black vertical line marks one hour of operation. (i) URG-04LX (ii) UTM-30LX; (b) Histograms of measured distances for upside-down sensors (i) URG-04LX for the first 30 minutes (ii) URG-04LX after warmed up (iii) UTM-30LX for the first 30 minutes (iv) UTM-30LX after warmed up.

(a) (b)

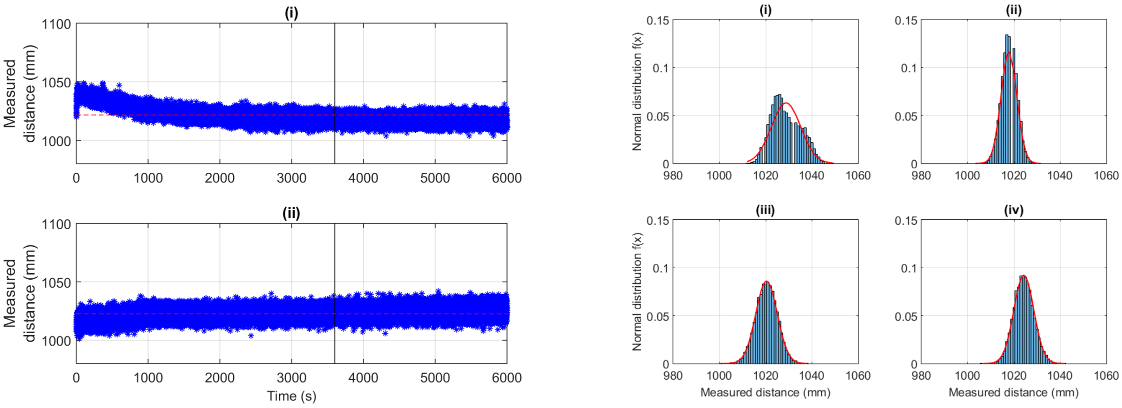

Source: author.

not cause significant influence on sensor's performance. Finally, warm-up time can be considered an issue for mobile robots using URG-04LX. Thus, for steady state performance, it is recommended at least thirty minutes of warm-up.

Figure 59 – Boxplot (a) URG-04LX (b) UTM-30LX. HS indicates heatsink.

(a) (b)

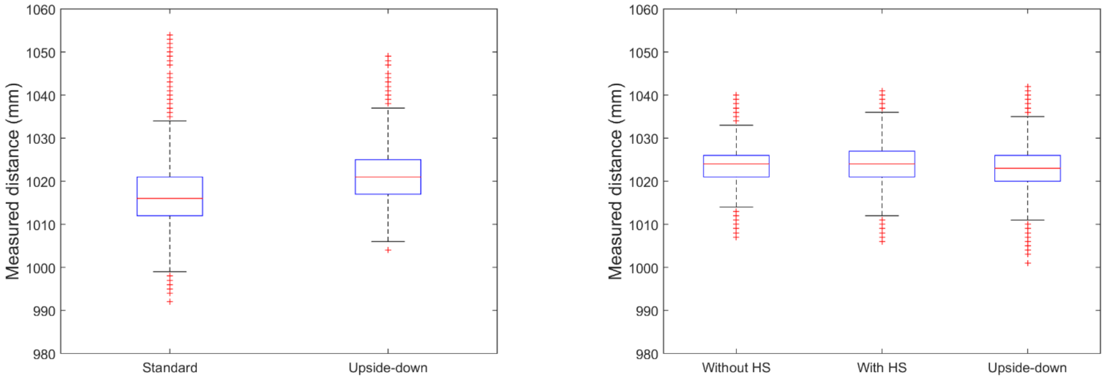

Source: author.